EFFECT OF HARMONIC FORCING ON TURBULENT FLAME PROPERTIES

A Dissertation
Presented to
The Academic Faculty

by

Sai Kumar Thumuluru

In Partial Fulfillment
of the Requirements for the Degree
Doctor of Philosophy in the
School of Aerospace Engineering

Georgia Institute of Technology

December 2010

EFFECT OF HARMONIC FORCING ON TURBULENT FLAME PROPERTIES

Approved by:

Dr. Tim Lieuwen, Advisor
School of Aerospace Engineering
Georgia Institute of Technology

Dr. Lakshmi Sankar
School of Aerospace Engineering
Georgia Institute of Technology

Dr. Jerry Seitzman
School of Aerospace Engineering
Georgia Institute of Technology

Dr. Shiva Srinivasan
Gas Turbine Technology Laboratory
GE Energy, Greenville

Dr. Suresh Menon
School of Aerospace Engineering
Georgia Institute of Technology

Date Approved: 5th November 2010

To my parents:
Lakshmi Thumuluru
and Ramachandraiah Thumuluru (Late)

ACKNOWLEDGEMENTS

It's been a long five years since I came to Georgia Tech and this dissertation would not be complete without the support of many people.

First and foremost, I would like to express my deepest gratitude to my advisor Dr. Tim Lieuwen for mentoring and supporting me throughout all these years. The multitude of meetings, discussions, career advice and long runs will always be remembered with very fond memories throughout my life. I would also like to thank Prof. Jerry Seitzman, Prof. Suresh Menon, Prof. Lakshmi Sankar and Dr. Shiva Srinivasan for serving on my committee.

For making life exciting, challenging and fun at the Combustion Lab., I would like to thank Rara, Murgi, Surki, Preetham, Santosh, Shadie, JP, Nelson, Nori, Qingguo, Priya, Bobby, Karthik, Yash, David, Jackie, Aditya, John Cutright, Brad, Vishal, SK, Tom, Claire, Jack, Chris, Andrew, Jim, Adam and all the other staff and students who are too numerous to mention here. Special thanks to Himani, Yogish, Kiruthika, Arun and Prabhakar for making life sweeter and fun outside work.

Finally, I would like to thank my parents and sister for their endless support, love and encouragement through every stage of my life. To save a few pennies for her children, my mother would refuse to use the public transportation and would instead walk to work. Such efforts and my father's ideology of "thinking big" will always be a constant source of inspiration throughout my life. Everything I am today is due to the endless sacrifices made by them.

TABLE OF CONTENTS

LIST OF FIGURES

LIST OF SYMBOLS

$S_{T,GC}$: Global consumption speed

$S_{T,LC}$: Local consumption speed

$S_{T,GD}$: Global displacement speed

$S_{T,LD}$: Local displacement speed

D : Fractal Dimension

σ : Standard deviation of phase jitter

τ : Integral time scale

L : Integral length scale

Φ : Phase jitter

<L> : Ensemble averaged flame location

Re : Reynolds number

D_t : Diffusivity coefficient

u'_t : Turbulence intensity

u'_a : Amplitude of acoustic velocity

f_{drive} : Drving frequency

δ_t : Flame brush thickness

t' : Flame development time

SUMMARY

Lean premixed combustors are highly susceptible to combustion instabilities, caused by the coupling between heat release fluctuations and combustor acoustics. In order to predict the conditions under which these instabilities occur and their limit cycle amplitudes, understanding of the amplitude dependent response of the flame to acoustic excitation is required. Heat release measurements using chemiluminescence techniques were conducted on an acoustically forced swirl combustor. Extensive maps of the flame response were obtained as a function of perturbation amplitude, frequency, and flow velocity. These maps illustrated substantial nonlinearity in the perturbation velocity – heat release relationship, with complex topological dependencies that illustrate folds and kinks when plotted in frequency-amplitude-heat release space. A detailed analysis of phase locked OH PLIF images of acoustically excited swirl flames was used to identify the key controlling physical processes and qualitatively discuss their characteristics. The analysis suggests that the flame dynamics are controlled by a superposition of the following processes – (1) annular jet fluctuations, (2) fluid mechanical instabilities of the backward facing step, jet column, swirl, and shear layer and (3) oscillatory flame speed and brush development. These results illustrate that the flame response is not controlled by any single physical process but rather by several simultaneously occurring processes which are potentially competing, and whose relative significance depends upon forcing frequency, amplitude of excitation, and flame stabilization dynamics. An in-depth study on the effect of acoustic forcing on the turbulent flame properties was conducted in a turbulent Bunsen flame. The results showed that the flame brush thickness and the local consumption speed grew in a step like manner. On examining the velocity field it was

seen that the turbulent intensity was also modulated in the presence of acoustic forcing. These results will not only be a useful input to help improve combustion dynamics predictions but will also help serve as validation data for models.

CHAPTER 1

INTRODUCTION

A large number of combustion systems have moved from operating in a non-premixed mode to a premixed mode, where the fuel and air are fully or partially premixed before entering the combustion zone. This is done to lower the flame temperature and hence decrease emissions from the nitric oxides (NOx). However, this operation under lean premixed modes can lead to issues which can be categorized into the following four main categories: (1) NOx, (2) CO, (3) turndown and (4) combustion dynamics. While emissions of combustion systems can be lowered by moving to a premixed system, a major drawback of lean premixed operation is the pronounced susceptibility to combustion instabilities.

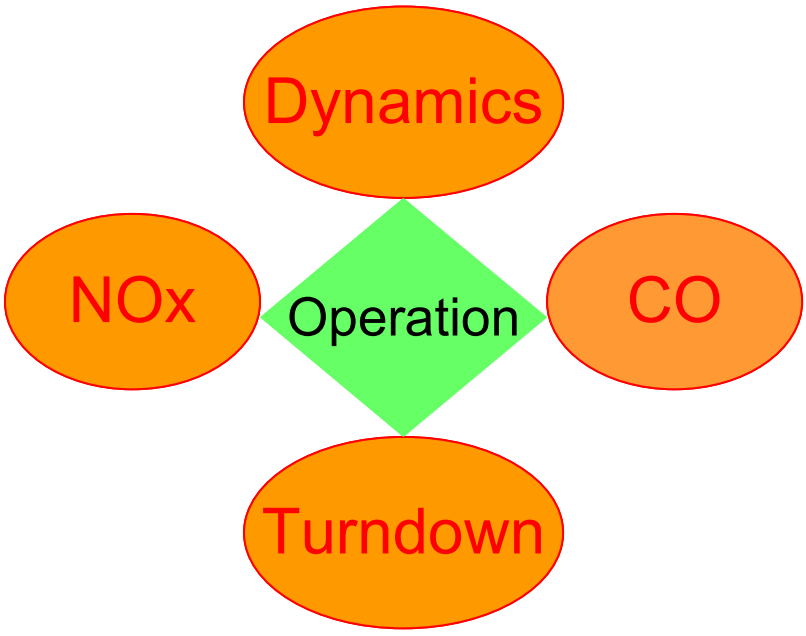

Figure 1: Operability regimes for typical lean premixed combustors operating on hydrocarbon fuels.

This research study focuses on combustion instabilities and in particular understanding

the physics that could lead to improved predictive models and hence reduced instability

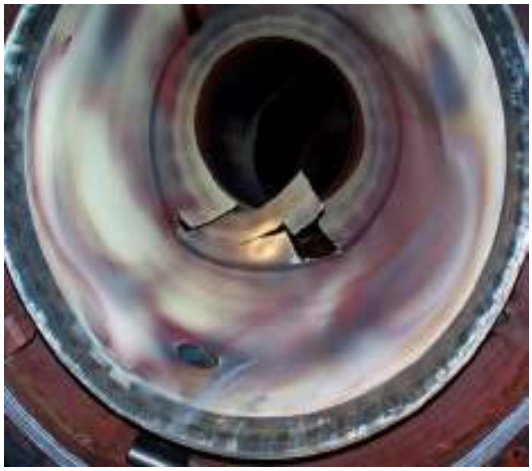

(a)

(b)

(c)

Figure 2 : Damaged (a) combustion liner, (b) transition piece and (c) turbine blades.

amplitudes.

The current work is motivated by the propensity of lean, premixed combustors to instabilities [1,2] which arises as a direct consequence of the coupling between the

combustion process and the acoustic modes of the chambers. Combustion instabilities are detrimental to hot section part life, as the instabilities cause severe damage to the section components. For example, shown in Figure 2 are the damaged combustion liner, a transition piece and finally the turbine blades. These damages require bringing the engine to a stop and replacing/repairing these damaged parts. In this competitive energy environment, this can represent large financial losses to power plants. The other effects of combustion instabilities include blowout or flashback if the instabilities are large enough.

The two most important parameters that characterize combustion instabilities are its amplitude and frequency. Predicting these parameters is crucial to combustor design and development. Models employing linear acoustics can be used to determine the frequency and the growth rates of these instabilities. However, predicting the amplitudes of these instabilities remains the biggest challenge as it requires nonlinear models. The main challenge lies in the determination of a key unknown relationship - between the pressure fluctuations and the heat release fluctuations. This relationship (typically nonlinear in nature) is an important input to models in order to predict the instability amplitude and is extremely difficult to determine, especially in self-excited combustion systems and at high pressures. This lack of information in the prediction of limit cycle amplitudes proves to be a key challenge to the gas turbine industry and is the primary motivation of this study.

The flame response to flow perturbations is much more complex than just a simple linear increase followed by saturation as assumed in several prior studies [3]. As will be shown in this research work, The flame response is not controlled by any single key

physical process, but rather several processes occurring simultaneously which are potentially competing, and whose relative significance depends upon forcing frequency, amplitude of excitation, and flame stabilization dynamics. This latter point is the key motivator for the present work – identifying and cataloguing the key physical processes is required before rational sense can be made of these results. Only with this understanding can the more global problem of the response of a turbulent flame to acoustic excitation be understood. Once the physical processes have been identified, the next step would be to examine each of the mechanisms in detail. In addition, most studies have dealt with the more global problem of flame response to acoustic modulations. However, very little research has been done to actually understand the underlying physics behind the flame response. This research work attempts to elucidate the physical processes that control the dynamics of acoustically excited turbulent flames. These include fluid mechanic instabilities, flame stabilization dynamics, and turbulent flame speed and brush development.

The above motivation leads us to the objectives of the current study which include: (1) Determining the flame response at various conditions of flow velocities, excitation frequencies and amplitudes, (2) Identifying the key physical processes, qualitatively examining their characteristics and illustrating the role they play in controlling the flame's amplitude dependent response characteristics and (3) conducting an in-depth analysis of one such mechanism *viz.* the effect of acoustic forcing on turbulent flame properties.

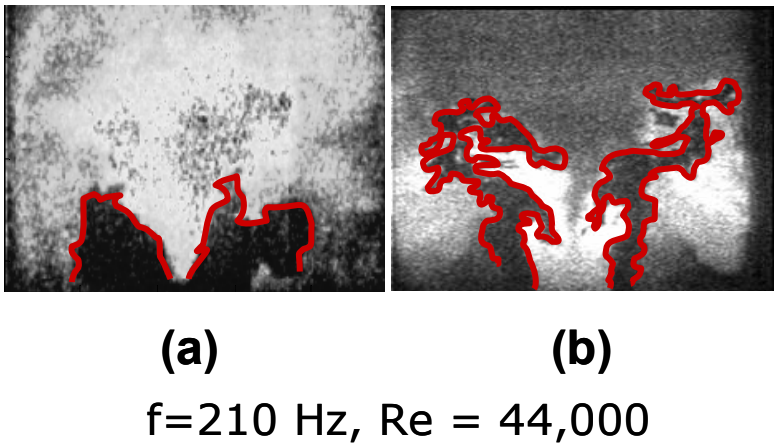

Figure 3: Sample pictures showing flame wrinkling at (a) u'/u_o =0.17 and (b) u'/u_o = 0.6 (Bellows *et al.* [12]).

The primary motivation for the latter objective is that, while numerous mechanisms have been proposed for the nonlinear response of turbulent flames to perturbations, there has been little emphasis on the effect of acoustic forcing on the turbulent flame properties. For example, Bellows *et al.* [12] observed that the degree of wrinkling increased at high amplitudes as compared to low amplitudes of excitation (see Figure 3) – this could indicate that the turbulent flame speed maybe modulated through the acoustic cycle.

Thesis Outline

The remainder of this dissertation is divided as follows. Chapter 2 presents a brief background on the significance of turbulent flame properties and its importance in combustion dynamics modeling. Chapter 3 describes the various experimental facilities used to conduct the experiments, the analysis methodology and the measurement uncertainties. This is central to all the analysis and results presented in Chapters 4-6. Chapter 4 discusses the results obtained from the chemiluminescence measurements performed on an acoustically forced swirl combustor. Here the transfer functions of the

flame response to acoustic forcing are presented at various conditions, including flow velocities, excitation frequencies and amplitudes. Chapter 4 also presents results from OH PLIF experiments that were conducted at select conditions based on the chemiluminescence measurements of the swirl combustor and characterizes the various flame shapes and the fluid mechanics that influence the flame response to harmonic forcing. Chapter 5 presents results on the turbulent flame properties of harmonically excited turbulent flames. Here, results for the flame brush development and flame speed variations are presented, first for the atmospheric swirl combustor and then for an acoustically excited Bunsen flame. A simplified model is developed and described to explain the flame brush development for the Bunsen flame. Finally, Chapter 6 summarizes the contributions from this thesis and provides recommendations for future work.

CHAPTER 2

BACKGROUND AND LITERATURE REVIEW

This chapter provides a brief background on the predictions of combustion instabilities. The first few sections provide an overview of the past literature on the proposed mechanisms of combustion systems in reaching limit cycle amplitudes. The importance of turbulence flame speed modulations in combustion amplitude predictions is then provided as well as relevant computational models used in the past to study the effect of turbulence flame properties on the instability amplitudes.

Combustion Instabilities

Combustion instabilities are excited by a feedback between the combustion processes and in general one of the acoustic modes of the combustor. A summary of the conditions under which combustion instabilities occurs is provided by Lieuwen and Yang [4] and is reproduced here in Figure 4. This figure illustrates a number of features, starting from the fact that combustion instabilities occur as a result of a feedback between the combustion process (flame) and the acoustics of the combustor. In addition, Rayleigh's criterion [5] states that combustion processes adds (removes) energy from the acoustics if Rayleigh's integral (Figure 4) is positive (negative). The sign of this integral depends on the phase difference between the heat release and pressure oscillations. If this phase difference is smaller (larger) than 90^o, Rayleigh's integral is positive (negative). Also, the energy losses (damping) present in a system is controlled by viscosity, heat transfer, radiation etc. Only if the driving exceeds the damping will the instabilities grow. Most commonly, combustion instabilities occur at frequencies associated with the natural modes of the combustor. These modes can be longitudinal (axial), radial or transverse. The focus of

this dissertation will be on understanding the physics of longitudinal instabilities which typically range in a few hundred Hertz.

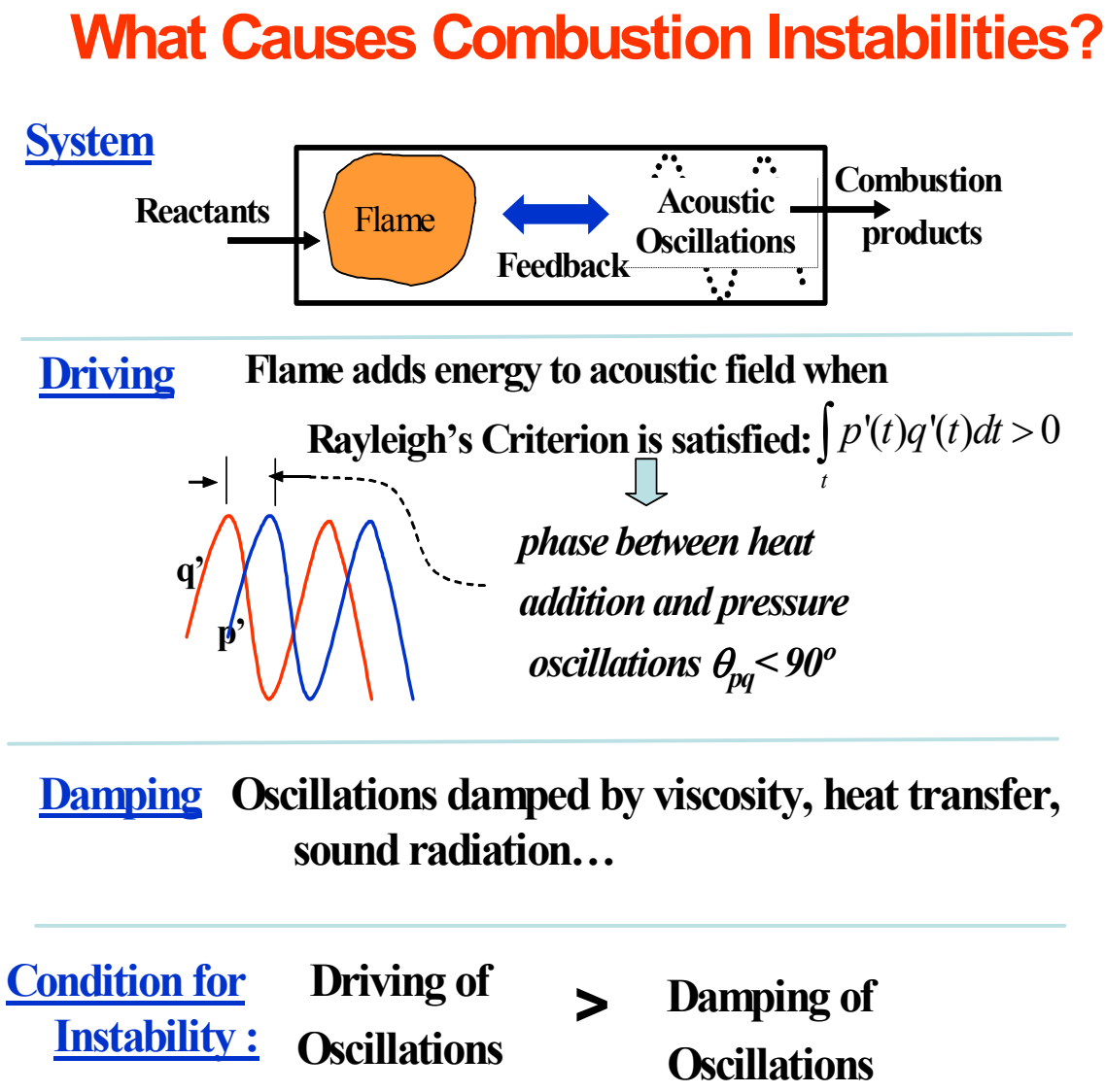

Figure 4: Conditions leading to combustion instabilities [4].

A fundamental understanding of how the flame responds to flow perturbations, and how this response varies with perturbation amplitude and flow conditions is required to predict the conditions under which instabilities occur and the limit cycle amplitudes. The flame's heat release response to a perturbation generally increases linearly with perturbation amplitude over a certain range of (low) amplitudes, before saturating or exhibiting more complex nonlinear behavior at high amplitudes [3,6]. These low amplitude linear dynamics generally control the balance between driving and damping processes at low amplitudes of oscillation and, thus, determine the regions under which self-excited oscillations can occur. On the other hand, the nonlinear combustor processes control the finite amplitude dynamics of the oscillations. This is well described by Yang and Lieuwen [4] who describe the dynamics of a system with disturbance amplitude (say A). The growth/decay of the disturbance is controlled by the driving, H(A), and damping, D(A), processes in the system. For example, in Figure 5 we see that a disturbance amplitude grows in the regimes where the driving exceeds the damping, i.e. $H(A) > D(A)$, stays constant when $H(A) = D(A)$, and decreases if $H(A) < D(A)$. The limit cycle of the disturbance (A_{LC}) describes the "steady state" amplitude of the self-excited oscillations. Therefore, predicting the limit cycle amplitude of self-excited oscillations requires an understanding of the nonlinear characteristics of the driving and damping processes present in the system. The key objective of this work is to characterize this nonlinear dependence and understand the physics behind the mechanisms causing such nonlinearities.

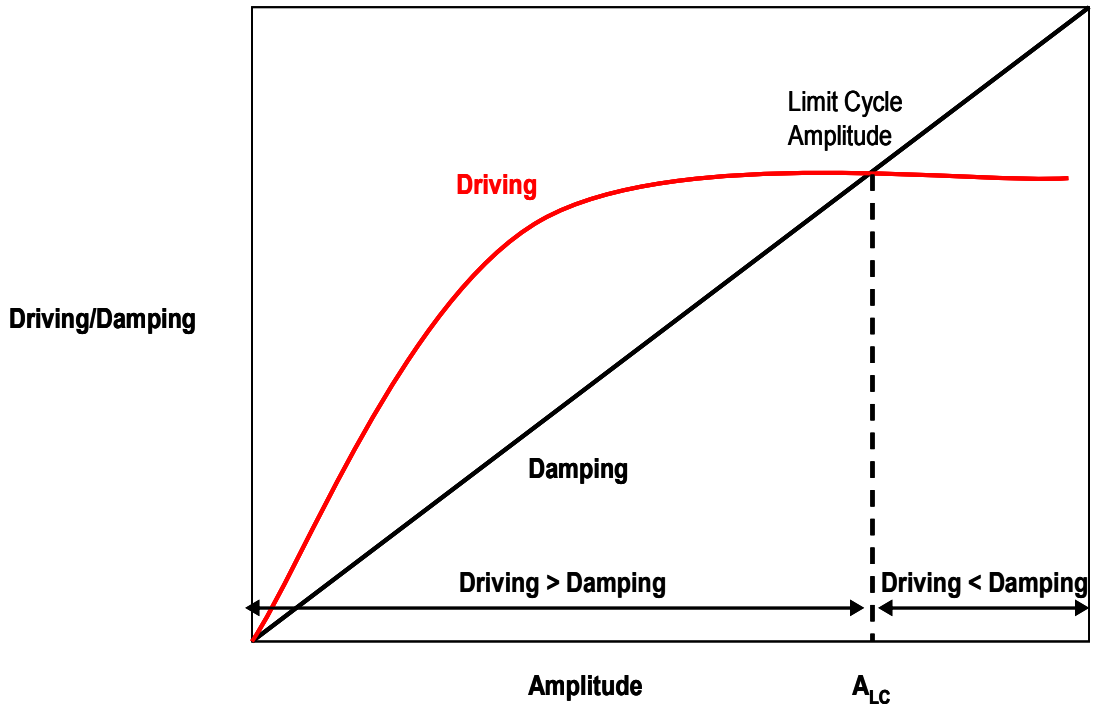

Figure 5: Driving and Damping as a function of instability amplitude (modified from Yang and Lieuwen [4]).

Numerous mechanisms have been proposed that attempt to explain this nonlinear flame response and these include local/global extinction of the flame [7], nonlinear boundary conditions [7], equivalence ratio perturbations [8], and flame front kinematics [9]. However, there are few experimental efforts that have actually characterized the nonlinear flame response to flow perturbations [10,11]. For example, Bellows *et al.* [12] and Kulsheimer and Buchner [13] and Santavicca *et al.* [14] quantified the nonlinear acoustic/heat release transfer function in turbulent, swirling flames, demonstrating that the flame response is linear at low forcing amplitudes and begins to saturate with further increase in amplitude. Bellows *et al.* [12] also identified flame liftoff and vortex rollup as two mechanisms that potentially cause nonlinearities in the flame response. Similar behavior was also reported by Balachandran *et al*. [15] in non-swirling flames. In addition, several modeling studies have treated the flame response as linearly increasing

with velocity perturbation amplitude before saturating at some prescribed amplitude [3,7]. The modulation of turbulent flame speed (S_T) through an acoustic cycle has also been suggested [16] as a possible mechanism causing non-linearities in the flame response. For example, if we assume that the instantaneous turbulent flame speed and flow velocity are proportional, then this will cause saturation in flame response.

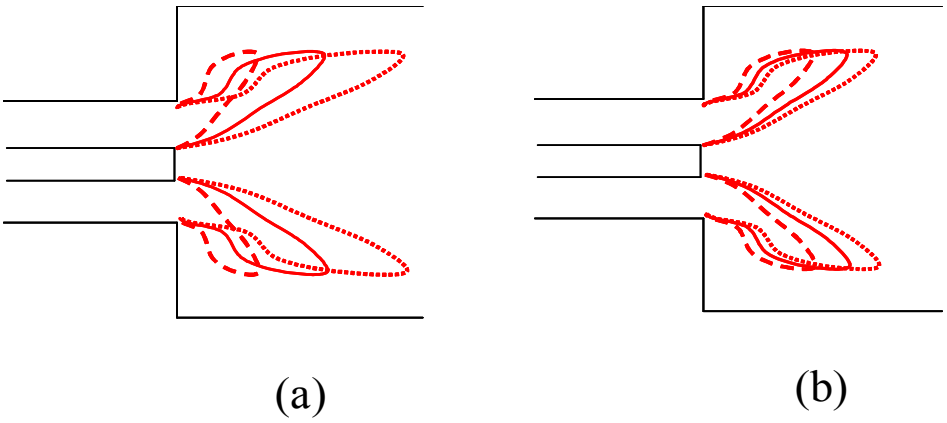

Figure 6: Illustration of fluctuations in ensemble averaged flame position for baseline case where turbulent flame speed is (a) constant and (b) oscillating in phase with the flow velocity.

To illustrate this, consider the scenarios depicted in Figure 6, which illustrate the ensemble averaged flame position at three points of the cycle without (left) and with (right) flame speed modulation. Without flame speed modulations, the flame position oscillates with some velocity amplitude dependent magnitude. If the flame speed increases with flow velocity, this will prevent the movement of the flame as far downstream as it would have if the flame speed remained lower. As such, the flame area will not increase as much as in the constant S_T case. In addition, as the flow velocity drops, the corresponding drop in S_T will result in the flame position not contracting back

upstream as much as in Figure 6 (a). Given the significance of turbulent flame speeds to the rest of this thesis, the next few subsections provide a brief background on it and its importance in combustion dynamics modeling.

Four definitions of the turbulent flame speed have been proposed [17]:

(1) Global Consumption speed - $S_{T,GC}$: This is the most basic definition and is in tandem to the definition of the laminar flame speed. The definition by Damkohler [18] states that the turbulent flame speed is estimate of the total fuel consumption rate (normalized by the reactant density and a reference flame area) across the entire flame surface. For example, as shown in Figure 7, if we have a turbulent flame front (as characterized by the highly wrinkled surface) and if each segment of the turbulent flame were assumed to propagate with a laminar flame speed S_L then it can be seen that the fuel consumption rate is given by:

$$\dot{m} = \rho_u A_T S_L \tag{2.1}$$

where $\dot{m}$ is the mass consumption rate, ρ_u is the unburnt reactant density and A_T is the turbulent flame surface area. If one were to assume that an effective flame speed with a flame surface area given by the area of the tube A_L and propagating at a turbulent flame speed given by $S_{T,GC}$ and with the same mass consumption rate i.e.

$$\dot{m} = \rho_u A_L S_{T,GC} \tag{2.2}$$

then by equating Equations (2.1) and (2.2) , one can see that the global turbulent flame speed is given by the ratio of the turbulent to laminar flame surface areas times the laminar flame speed.

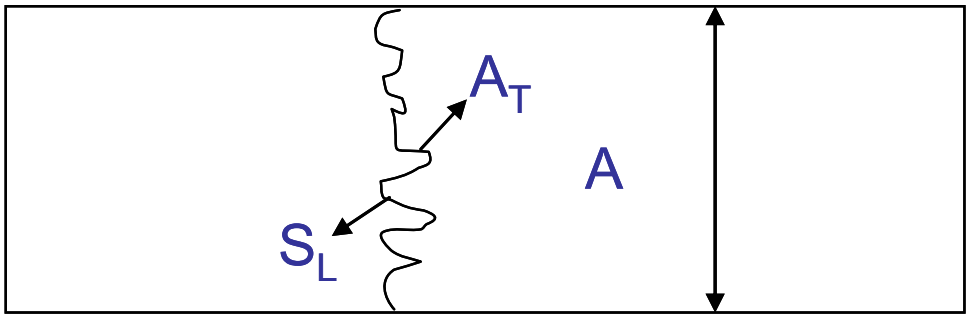

Figure 7: Turbulent Flame Segment and definition of turbulent flame speed.

This definition indicates that higher the flame surface area (A_T) of the turbulent flame, higher is the turbulent flame speed and hence higher is the fuel consumption rate. It should be noted that the global consumption speed is unique and independent of any coordinate axes – an issue that is seen to arise with other local definitions. The advantage of the global consumption speed is that one single number can be provided for a given combustion system (combustor configuration, fuel types etc.) at a given flow velocity, turbulence intensity etc. A drawback of this definition is that it necessarily averages over the entire flame brush whose local consumption rate might vary locally.

(2) Local Consumption Speed - $S_{T,LC}$ [17]: While the global consumption speed encompasses the entire flame and provides one single number for a given combustor configuration, the local consumption speed attempts to provide a more local and spatial description of the turbulent flame speed. This is particularly important to understand the underlying physics local to the flame surface. If we were to consider Figure 7 to be a segment of an entire flame then the definition of the turbulent flame speed becomes local in nature and is called the Local Consumption Speed $S_{T,LC}$. It should be noted however that this definition for the local segment is dependant on the coordinate axes chosen.

(3) Local Displacement Speed - $S_{T,LD}$ [17]: The local reactants speed normal to the flame brush at its leading edge maybe used to define a local displacement speed. The

flame brush is locally normal to the approach flow and by definition the mean axial velocity entering the flame brush is $S_{T,LD}$.

$$S_{T,LD} = \overrightarrow{U_f} - \overrightarrow{U_r} = |U| Sin\theta \tag{2.3}$$

(4) Global Displacement Speed - $S_{T,GD}$ [17]: The global displacement speed, $S_{T,GD}$ is the average of $S_{T,LD}$ over the entire turbulent flame brush. It is meaningful only for a system where the propagating flame brush has no edge. This condition is satisfied for example in an expanding flame kernel initiated by a spark in a combustion

$$S_{T,GD} = \frac{\partial r_f}{\partial t} - \overrightarrow{U_r} \tag{2.4}$$

While all the four definitions are unique in their own sense and are independent of one another, any of the four maybe used to describe the turbulent flame speed. In the current study, the global and local consumption speeds will be used - the importance of these speeds are further described in the next section.

Importance of Turbulent Flame Properties in Combustion Dynamics

There is very little work in the literature that emphasizes the variation of the turbulent flame properties such as flame brush and speed and flame brush with downstream distance and through an acoustic cycle. In the RANS models developed by Sathiah and Lipatnikov [19] to predict combustion dynamics, the authors assumed that the flame speed increased rapidly with downstream distance before reaching a constant value. The authors explained that the rationale behind this assumption being that the flame speed was impacted by small scales and hence by small time scales - thus leading them to believe that the flame speed was assumed to grow rapidly before reaching an asymptotic value. Zimont [20,21] and later Sathiah and Lipatnikov [19] also argued that

the flame brush thickness grew continuously for most practical systems and based most of their computational models on this argument [22]. For example, Figure 8 presents typical experimentally observed flame brush results for two kinds of flames – a conical Bunsen flame and a V-flame. From this figure, it can be seen that the flame brush grows monotonically with downstream distance. The generalized explanation provided for these results is that the turbulent diffusion is the major cause for the flame brush growth.

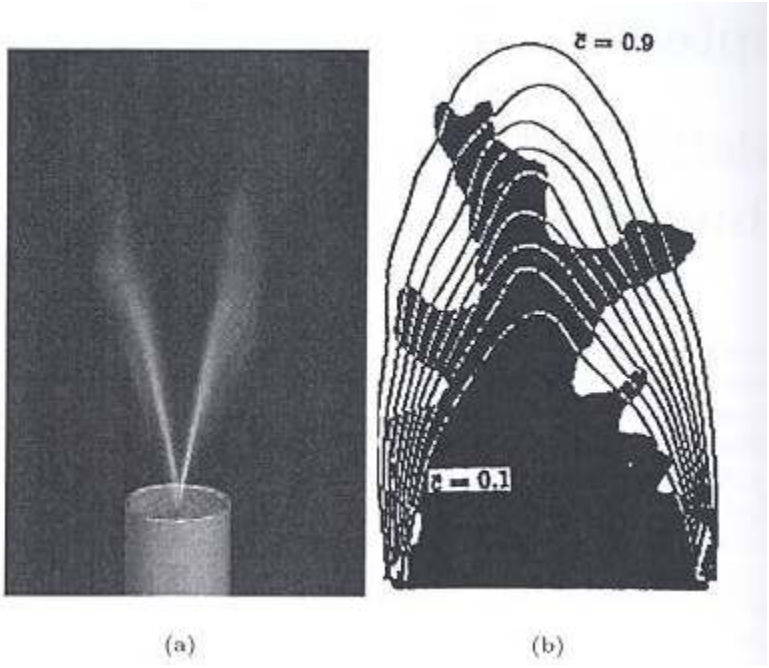

Figure 8: Growth of the turbulent flame brush in two types of flames (a) V flame and (b) conical Bunsen flame [19].

A common model for the flame brush thickness whose growth is determined by turbulent diffusion is given in Equation (2.5) where τ' represents the integral time scale, D_t represents a coefficient of diffusivity, t' represents the flame development time and σ represents the flame brush thickness. This model also shows that at small time scales, the flame brush thickness has a linear dependence with flame development time and at large times a square root type dependence.

It is generally assumed that in the presence of acoustics, the spatial variation of the flame brush is similar to that in the absence of acoustics. However, there exist no studies that examine this kind of behavior in the presence of acoustics - this is the additional motivation for the current research study.

$$\delta_t^2 = 2D_t t' \left\{ 1 + \frac{\tau'}{t'} \left[\exp\left(-\frac{t'}{\tau'} \right) - 1 \right] \right\} \tag{2.5}$$

$$\delta_t \propto \begin{cases} t' & if \quad t' << \tau' \\ \sqrt{t}' & if \quad t' >> \tau' \end{cases} \tag{2.6}$$

Next, based on this model for flame brush development, Zimont [20,21] proposed a closure model which was later extended by Lipatnikov [22] and is now known as the flame speed closure model. The model states that the turbulent flame speed may be assumed to vary in a similar manner as the flame brush thickness and is given in Equations (2.7) - (2.9).

$$S_{t,t} = S_t \left\{ 1 + \frac{\tau'}{t'} \left[\exp\left(-\frac{t'}{\tau'} \right) - 1 \right] \right\}^{1/2} \tag{2.7}$$

$$\frac{\partial \bar{\rho}\tilde{c}}{\partial t} + \frac{\partial}{\partial x_j}(\bar{\rho}\tilde{u}_j\tilde{c}) = -\frac{\partial}{\partial x_j}(\overline{\rho u''_j c''}) + \bar{\rho}\tilde{W} \tag{2.8}$$

$$\frac{\partial \bar{\rho}\tilde{c}}{\partial t} + \frac{\partial}{\partial x_j}(\bar{\rho}\tilde{u}_j\tilde{c}) = -\frac{\partial}{\partial x_j}(\bar{\rho} D_t \frac{\partial \tilde{c}}{\partial x_j}) + \rho_u S_t \left| \triangleq \tilde{c} \right| \tag{2.9}$$

Zimont proposed that the species equation - Equation (2.8) may be closed by assuming a diffusion model (i.e. by a diffusivity coefficient D_t) and by further assuming that a turbulent flame speed S_t exists along with the progress variable contours *č*. The rationale behind this assumption is that the turbulent flame speed is mainly affected by

small length scales. Hence, it is expected that at short time scales, the flame speed is expected to grow and saturate or increase very slowly at large time scales. The flame speed closure model is a model that is also commonly used in commercial software such as FLUENT and incorporates the above explained features for the species equation. Lipatnikov and Sathiah [19] used the Flame Speed Closure model to predict combustion instability amplitudes on a bluff body type combustor using RANS simulations. In their calculations the authors stressed the need for having a good description of the spatial variation of the turbulent flame speed and its impact on combustion instability predictions.

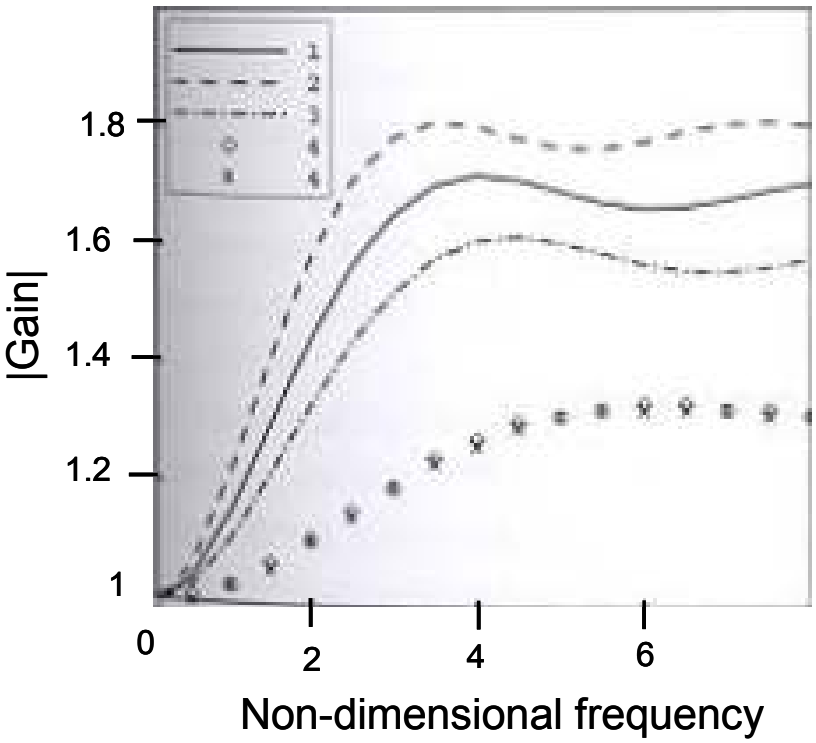

Figure 9: Effect of flame speed development on combustion dynamics predictions. Symbols assume constant flame speed and the solid lines are for different turbulent length scales [19].

Figure 9 reproduces one such sample result [19] which describes the effect of

having a constant flame speed (bold lines) and a spatially varying flame speed on the gain of the combustion instabilities across different turbulent length scales. From this figure it can be seen that by assuming a constant flame speed under predicts the amplitude of the instabilities in comparison to a spatially varying flame speed. This figure shows that flame speed development can impact the amplitude of the instabilities significantly and emphasizes the need to accurately predict the development of the turbulent flame speed.

Although, the above literature focuses on turbulent flames, there have been no fundamental studies on understanding the impact of acoustic forcing on turbulent flame brush and speed development. In addition, there have been no research studies attempting to experimentally validate the flame brush and speed development of the above mentioned models in the presence of acoustics. This also proves to be the motivation behind conducting a detailed analysis on the effect of acoustic forcing on turbulent flame properties.

CHAPTER 3

EXPERIMENTAL FACILITY

This chapter describes the experimental facilities, instrumentation and diagnostic techniques that were employed in the current research study. The two different kinds of combustors that were used are described, along with a description of the various instrumentation that were used in data acquisition including dynamic pressure, heat release and flow rates. Finally, the diagnostic techniques that were employed to visualize the flame front as well as conduct velocity measurements in the combustor are also described.

Swirl Combustor

The first type of combustor was a swirl stabilized combustor with a center body that was operated at atmospheric pressure and at ~ 20 KW thermal power. A schematic of the nozzle and the combustor section is shown in Figure 10. The fuel (natural gas) and air were premixed upstream of a choke point to prevent the occurrence of fuel/air ratio oscillations. The equivalence ratio was maintained at a constant value of 0.8 throughout the experiments. This was done in order to separate the response of heat release oscillations to acoustics from that of equivalence ratio fluctuations. The uncertainties estimated from the calibration of the rotameters is provided in Appendix 1 and were seen to be within 5% accuracy for the range of flow velocities for both the air and fuel rotameters.

Acoustic oscillations were excited using two drivers mounted upstream of the combustor. The two acoustic drivers were police sirens of model type: Galls SA 400 and with an operable range of 50 – 4000 Hz.

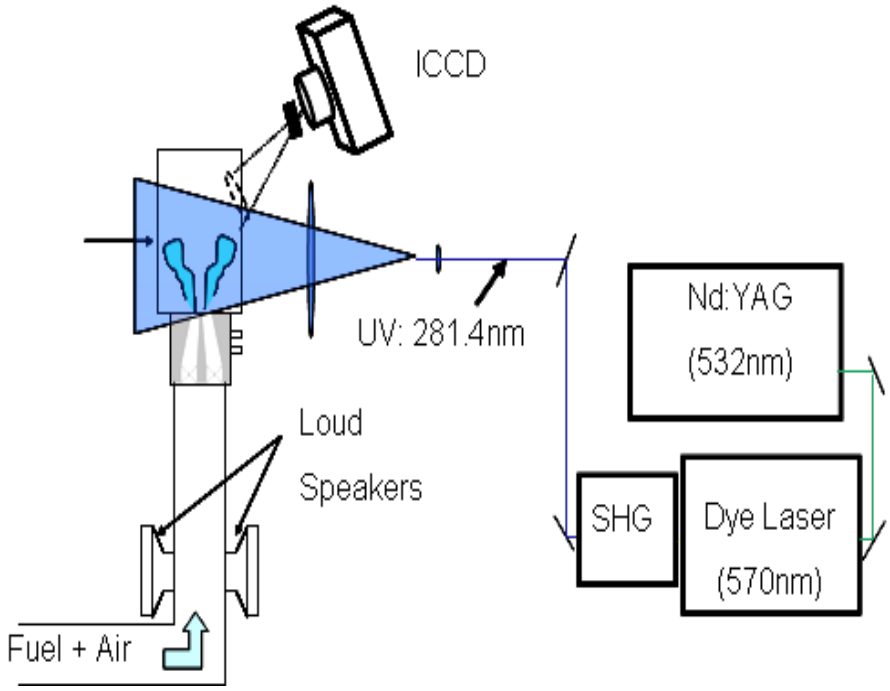

(a)

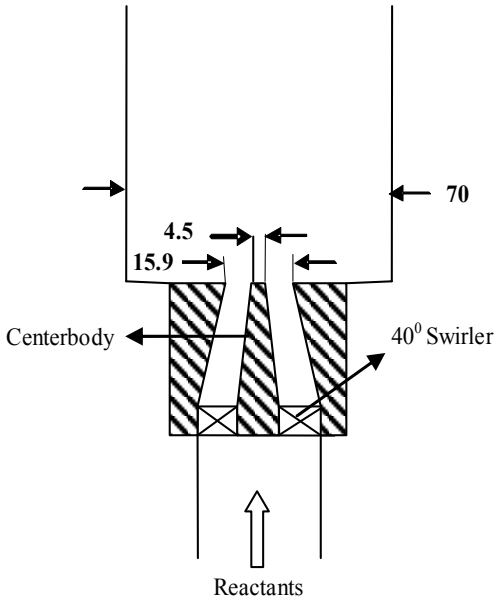

(b)

Figure 10: Schematic of the (a) experimental setup and (b) nozzle.

The sinusoidal input signals were provided by a Tektronix Signal Generator (AWG 300) which was then passed through a RadioShack amplifier that drove the two sirens.

Instrumentation

Dynamic Pressure and Velocity Measurements

Pressure oscillations were measured using two Model 211B5 Kistler type pressure transducers mounted downstream of the swirl vanes, located 5.85cm and 7cm upstream of the nozzle exit. The piezo-electric transducers were accurate within 1%. The sensitivities of the two transducers used were 50 *mV/psi* and had an operating range of 0-100 *psi*. The signal from the pressure transducers was amplified in order to achieve higher signal to noise ratios. Velocity oscillations were then calculated using the two microphone method which in the most general form uses the linearized Euler equation to relate the pressure and the velocity fluctuations [23,24]. The Euler equation here is a statement of the conservation of momentum with several assumptions. First, viscous losses are neglected. This assumption works well in acoustics outside of the boundary layer due to the long wavelengths of the flow disturbances. Secondly, for low Mach number flows, terms of the order of the mean flow are neglected. The effect of mean flow at low Mach numbers has been shown to have little impact on the calculations of the pressure amplitude [25]. By making these assumptions, the one-dimensional Euler equation then becomes:

$$\rho \frac{\partial u'}{\partial t} = -\frac{\partial p'}{\partial x} \tag{3.1}$$

Taking the Fourier Transform of this equation yields Equation (3.2) and is used most readily in acoustic processing because of the importance of the frequency content of

the signals. The capital letters indicate the Fourier Transforms of the velocity and pressure signals.

$$i\omega\bar{\rho}U = \frac{\partial P}{\partial x} \tag{3.2}$$

Finally, by making the assumption that the pressure measurements are taken at a relatively small distance apart, the spatial derivative can be discretized, and the final form of the equation, solving for the velocity, is given in Equation(3.3).

$$U = \frac{1}{i\rho c}\frac{P_2 - P_1}{k\Delta x} \tag{3.3}$$

In this form, Δx has been non-dimensionalized by the wave number k, where $k=\omega/c$. This method calculates the acoustic velocity half-way between the microphones, or $\Delta x/2$. P_2 and P_1 are frequency domain measurements recorded from the piezo-electric transducers.

Chemiluminescence Measurements

Heat release fluctuations were characterized from measurements of the global CH* and OH* chemiluminescence with photomultipliers (PMT) fitted with a 10 nm bandwidth filter centered at 430 nm and 310 nm, respectively. A typical wave number spectra showing the same is shown in Figure 11 [26]. The flame response is characterized by the OH* and CH* chemiluminescence and is measured using an optical fiber which is connected to two photomultiplier tubes that have 310 ± 10 nm (OH*) and 420 ± 10 nm (CH*) band pass filters on them.

Appendix 2 describes the operation of the PMT and shows that its output is linearly related to the input chemiluminescence (from the combustor) for the experimental conditions explained here. It should be noted that the field of view of the photomultipliers

was such that it covered the entire combustion region, so as to ensure that the global heat release rate from the combustor was being measured.

The chemiluminescence and hence the heat release fluctuations are susceptible to fluctuations in the flame area and equivalence ratio fluctuations. In order to isolate and study the effect of acoustics on the flame response separately; the focus of this research study, the equivalence ratio was maintained constant throughout the experiments.

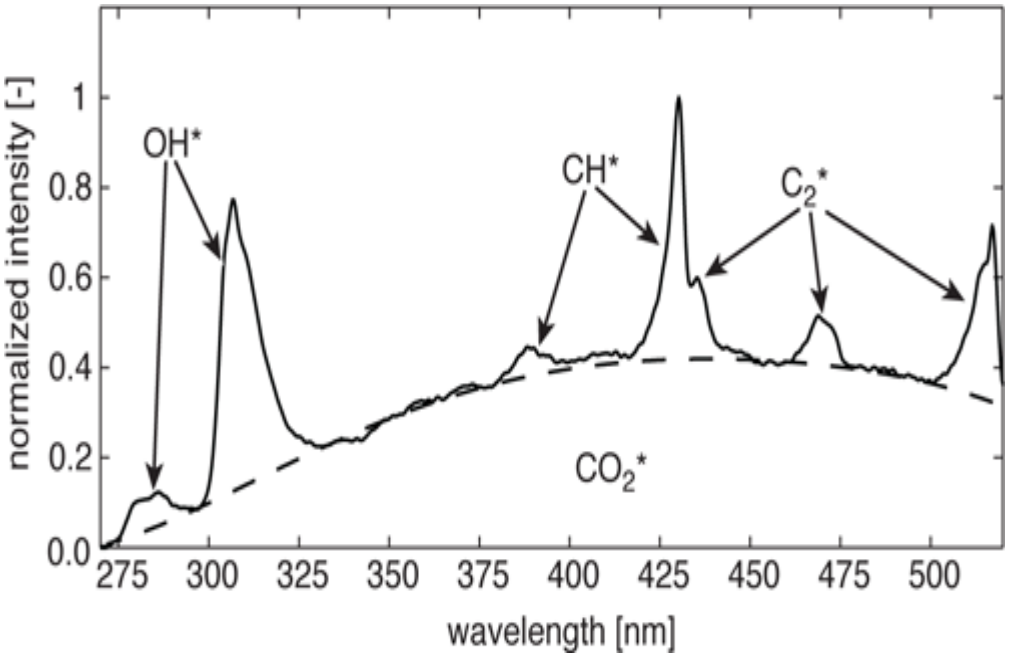

Figure 11: Typical chemiluminescence spectrum in a premixed combustor [26].

Data Acquisition System

The signal from the PMTs and the pressure transducers (after amplification) were filtered to cut out high frequency noise and were then passed through a National Instruments 12 bit Data Acquisition board (PCI – MIO – 16E -1). 10000 data samples were recorded every second and the number of samples recorded per data set was 16,384. This resulted in a frequency resolution of 0.61 Hz in the frequency domain. The post

processing of the data involved splitting the data into 8 continuous ensembles and taking the Fast Fourier Transform (FFT) of each ensemble to estimate the power spectrum. In order to minimize the variance in the spectral estimate, the FFTs were ensemble averaged and the amplitude and phase at the excitation frequency and its harmonics were then determined.

Diagnostic Techniques

Phase locked OH PLIF [27,28] was used to visualize the spatial dynamics of the flame at select operating conditions from the results of the chemiluminescence measurements. A schematic of the system is shown in Figure 10 (a). The laser system consists of a cluster of an Nd: YAG laser, a dye laser, and a high-resolution ICCD camera. For OH PLIF, the frequency-doubled output from the dye laser was tuned near 281.4 nm to pump the R_1 (9) transition of the $A^1\Sigma - X^2\Pi$ (1, 0) band. OH fluorescence integrated over a wave number range of 300-380 nm is captured by the ICCD camera through both a WG-305 and UG-11 Schott glass filter. Since the frequency of imaging was limited by the Nd: YAG laser to 10 Hz, successive phase-locked images were actually obtained several cycles apart from each other. Fifty flame images per phase were obtained at 6 phase angles, at a resolution of about 270 μm / pixel. The captured images were corrected for background noise and for beam profile in-homogeneities and were filtered using a 3-pixel width Gaussian filter.

Since the flames were highly multivalued, an automated technique to extract the flame edges from the OH PLIF was not possible. Hence, the flame edges were captured manually using the intensities as well as the gradients from the PLIF images. Since the flame edges were captured manually, it consequently is the key limiter in our ability to

quantitatively post-process these images. Determination of the flame front location was straightforward in most cases, and to minimize the errors in variability, the edges were captured by multiple personnel. While the majority of the results were qualitative in nature, the maximum variability in quantifying the results was less than 10%. This number was not significant to affect the analysis of the results.

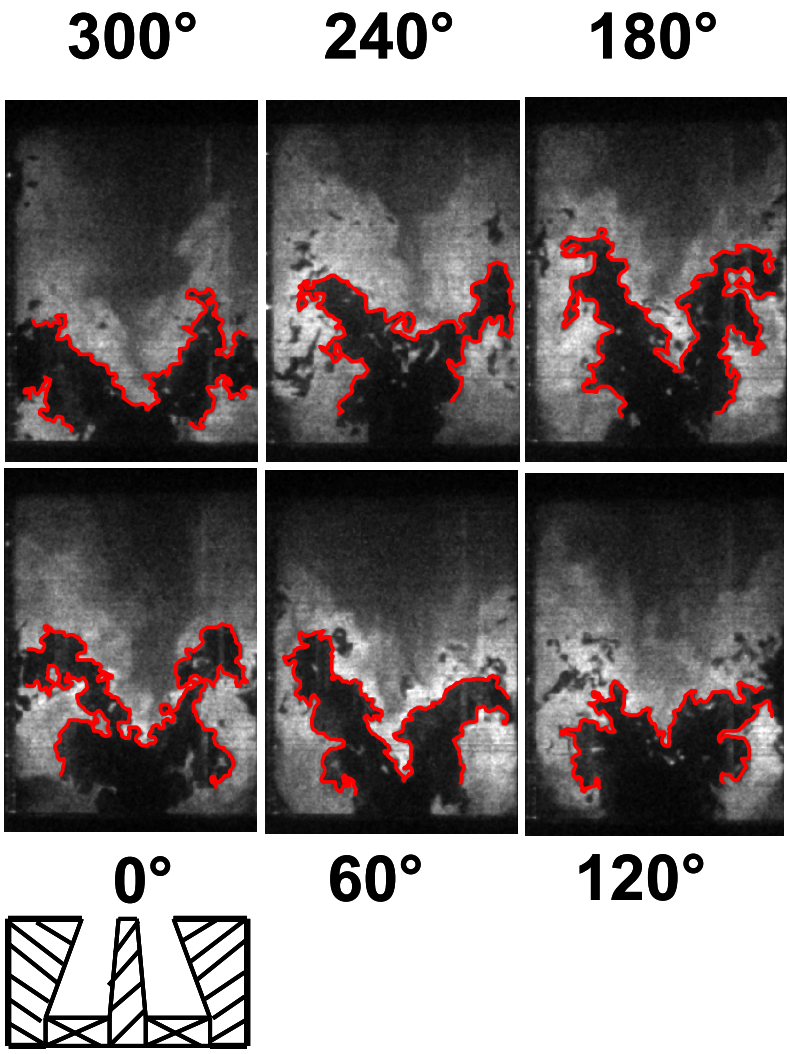

Figure 12: Sample instantaneous OH PLIF images at u'/u_o = 0.17 and *Re* = 44,000.

Figure 12 show sample instantaneous OH PLIF images at various phases of an acoustic cycle. Determination of the flame front location was straightforward in most

cases, except in regions where the flame is close to the combustor walls and/or where there is back mixing of OH laden products. In the latter case, determination of whether the interface between regions of high and low OH levels corresponded to a flame or a non-reacting, product-reactant interface was determined from the OH gradient. Gradient values that fell substantially below typical gradient levels for regions with known flames were not marked as flame fronts.

Bunsen Burner

Experiments were also conducted on an acoustically excited turbulent Bunsen flame (where the flow field was less complex). Figure 13 illustrates the axisymmetric Bunsen burner (ID 25.4 mm). The fuel (natural gas) and air were premixed upstream at an equivalence ratio of 0.85. Acoustic oscillations were introduced through a loudspeaker mounted upstream of the combustor. The flame was stabilized by a lean premixed pilot flame at low flow rates relative to the main burner (2 % of the main flow).

Turbulence Characteristics

Time resolved turbulence characteristics of the flow were obtained using hot wire anemometry at a sampling frequency of 10 kHz. The system used to characterize the turbulent field was a DANTEC 5P11 constant temperature hot wire anemometer. The experiments were conducted at a Reynolds number of 10,200 (based on the burner exit diameter and mean flow velocity of $u_o \sim 10$m/s). The turbulent spectrum at the centerline of the jet just downstream of the burner is shown in Figure 14. A line of slope -5/3 is also shown for reference and from this figure it can be seen that the turbulent field is isotropic and fully developed. In the unforced case, the centerline turbulent fluctuations were of the order of $u'_T/u_o = 0.05$. Forced excitation cases were obtained at f_o=200 Hz and at the

disturbance amplitude of $u'_A/u_o = 0.15$.

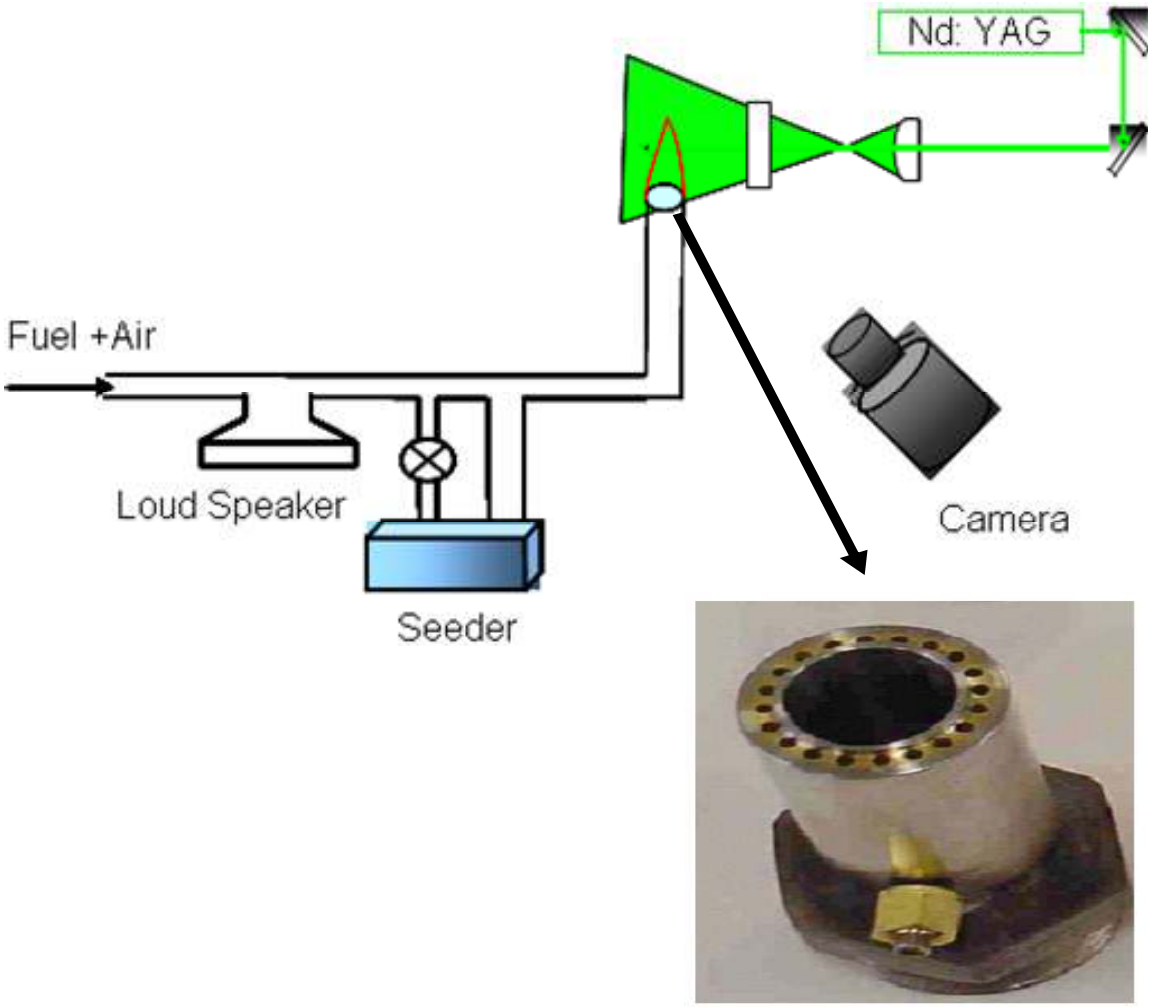

Figure 13: Schematic of the experimental setup used for studying the Bunsen flame

Optical Diagnostics

The spatial characteristics of the flame and the velocity field were measured using phase locked PIV measurements. A schematic of the experimental setup is shown in Figure 13. The PIV measurements were carried out using a double pulsed Nd:YAG laser, frequency doubled to 532 nm and sheet forming optics. In addition, a band pass filter at 532 nm was placed in front of the detection optics to suppress the interference from flame luminescence. The flow was seeded with aluminum oxide particles of diameter 0.5-1 μm

to ensure good tracking of the fluid motion.

Light scattered by the seeding particles was collected at right angles on a 1600 X 1200 ICCD camera fitted with a 55 mm f/5.6 Nikon lens. The spatial resolution of the images achieved by using this camera was around 50 microns/pixel. The velocity field was computed using a 32 X 32 pixel square window, with an overlap of 50%.

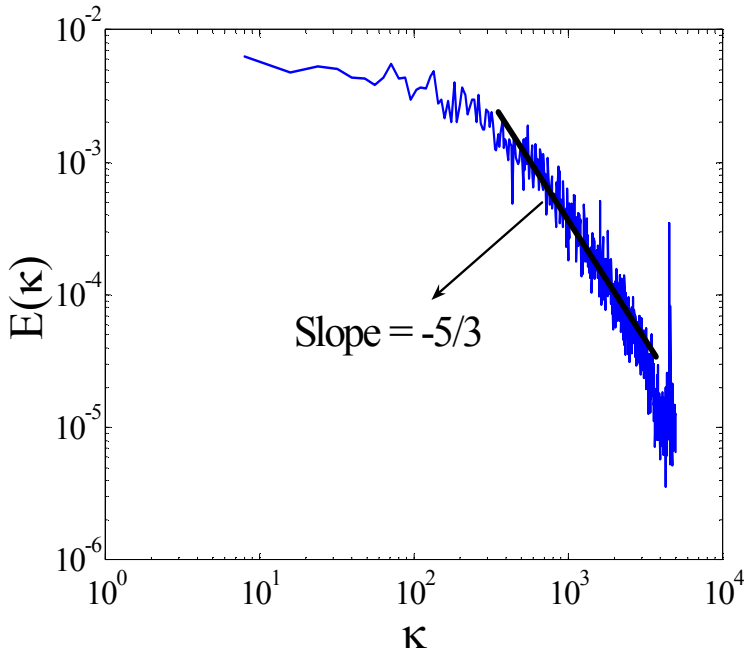

Figure 14: Centerline turbulence kinetic energy spectrum for Bunsen flame.

To achieve phase locking, the timing between the signal generator, the two laser heads and the camera shutter was synchronized using a delay generator.

At each excitation amplitude and at 8 phases of an acoustic cycle, 512 phase locked images were recorded. Figure 15 shows a sample instantaneous Mie-scattering image used for the PIV analysis.

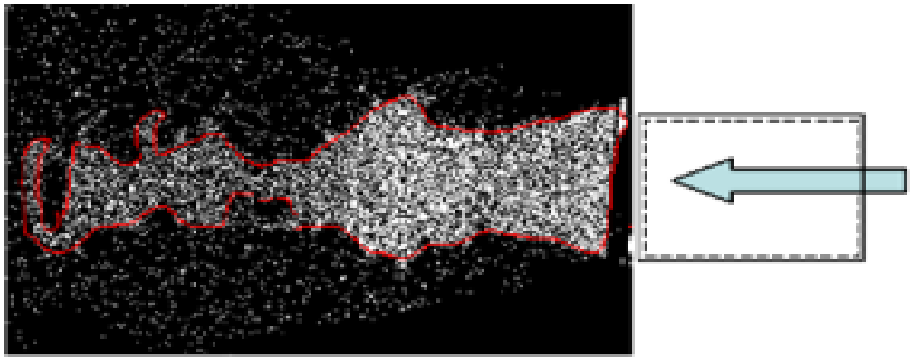

Figure 15: Sample PIV image showing the flame edge location (red line - gradients between the high seeding density in reactants and the low seeding density in products).

This sample image illustrates the high contrast between the high seeding density in reactants and the low seeding density in products.

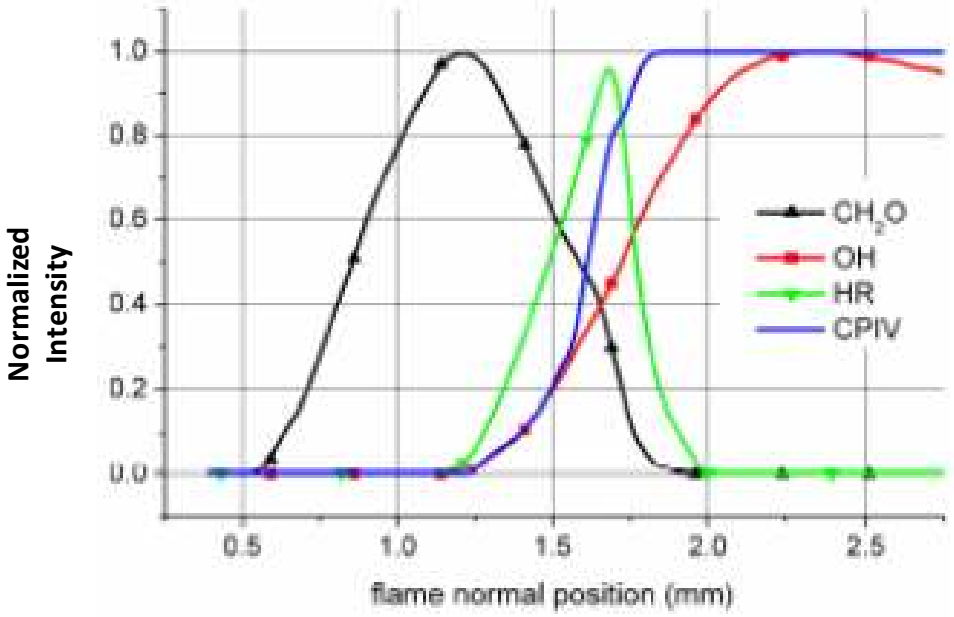

Figure 16: Comparison of flame normal positions from simultaneous LIF and CPIV for a turbulent Bunsen flame [29].

In addition, it can be seen that the flame is highly corrugated and multi-connected and although not shown here, the formation and burnout of pockets were also seen near the tip region of the flame.

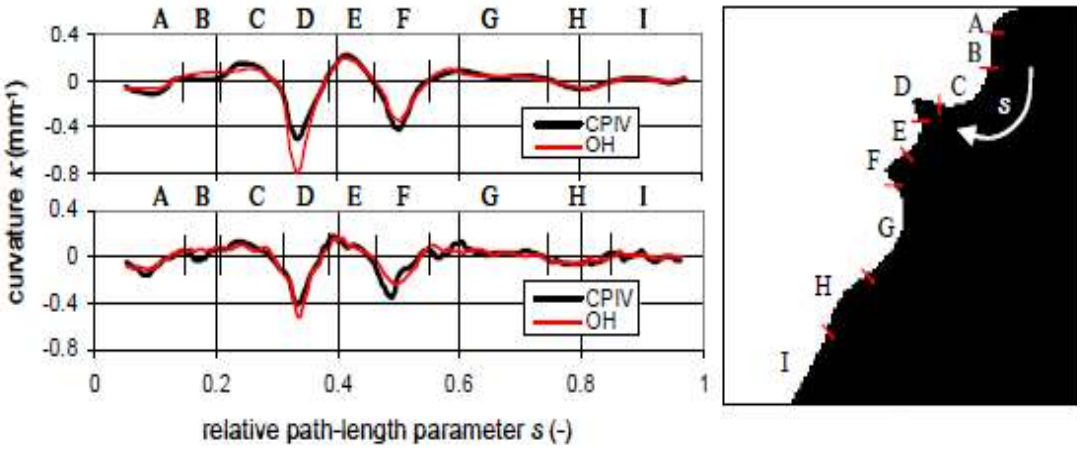

(a)

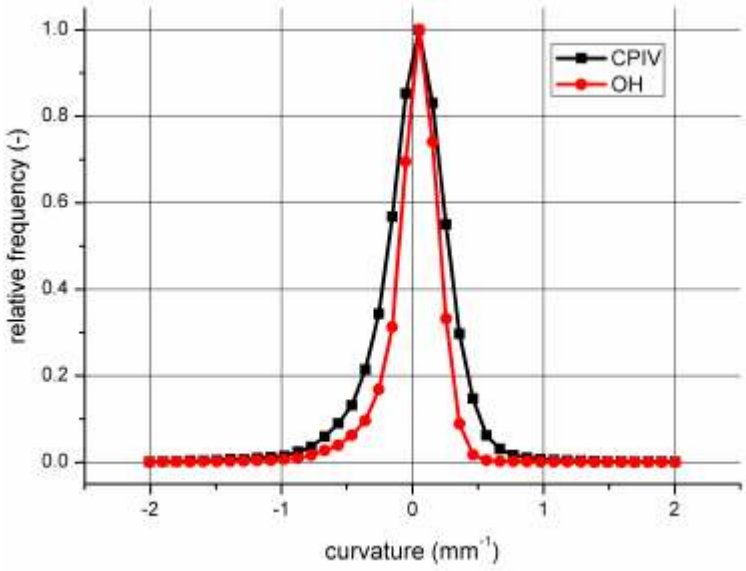

(b)

Figure 17: Comparison of flame statistics from OH PLIV and CPIV for a turbulent Bunsen flame [29].

This high contrast allows for tracking of the flame edge, as indicated by the red line in the figure. This technique has been used previously to capture the flame front and is commonly referred to as Conditional PIV (CPIV). Research studies [29] comparing this method with OH and CH_2O LIF measurements (see Figure 16 and Figure 17) show that there exists minimal difference (< 1mm) in the location of the flame front between the methods [30, 31]. This deviation is seen to be much lesser on computing the flame front statistics as shown in Figure 17 which compares the results from OH PLIF and CPIV. The conditions used in the above reference studies are very similar to the conditions used in the current study; hence it can be assumed that the statistics of the flame front are well captured by CPIV.

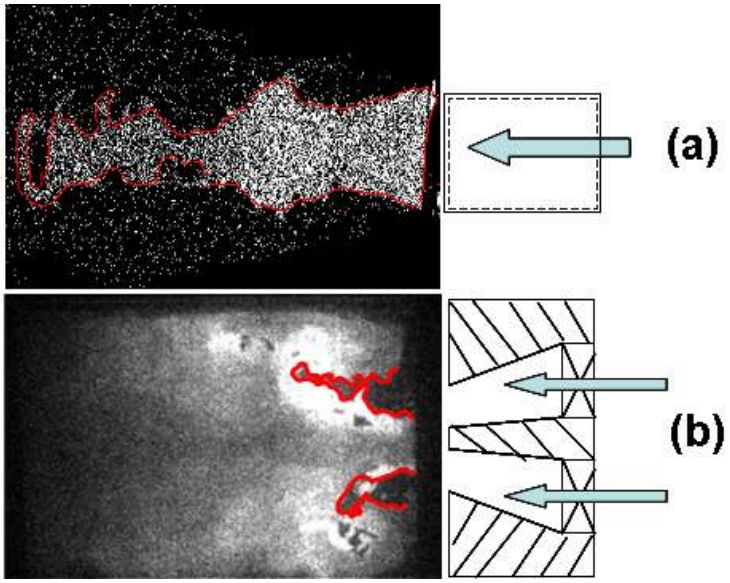

Figure 18: Sample instantaneous (a) Mie-scattering image used for the PIV analysis (f_o=200 Hz, u'_d/u_o=0.2, 0^o phase with respect to the forcing signal) and (b) OH PLIF image of the unforced swirl flame (Re=21,000).

Estimation of Turbulent Flame Parameters

The turbulent flame brush thickness and the local and global flame speeds of both the Bunsen and swirl flames were calculated in the following manner.

Flame Brush Thickness

Each instantaneous image (Figure 18) was converted into a binary image of reactants (progress variable $\bar{c}$ = 0) and products ($\bar{c}$ = 1). Next, these binary images were averaged at each phase to yield an ensemble averaged image (Figure 19) with the progress variable varying spatially from 0 to 1. The flame brush thickness was then determined as the distance between the contours of $\bar{c}$ = 0.3 and 0.7, along the normal drawn from the $\bar{c}$ = 0.5 contour. The variations in the flame brush thickness were obtained as a function of the axial distance along the centerline of the combustor. The flame coordinate was measured along the arc length of the $\bar{c}$ = 0.5 contour starting from the base of the flame and extending to the tip.

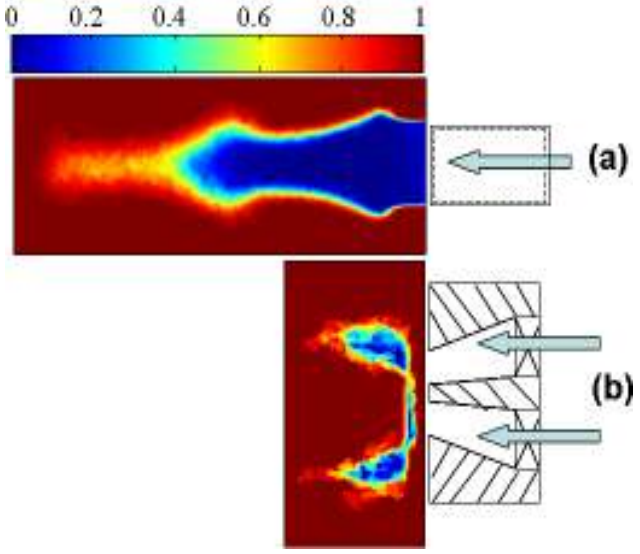

Figure 19: Sample images showing the variation of the ensemble averaged progress variable ($\bar{c}$ = 0 indicates reactants, while $\bar{c}$ =1 indicates products) for the (a) forced Bunsen flame and (b) forced swirl flame.

Fractal Dimension

In addition to qualitative image analysis of the flame front, the flame's topological characteristics were quantified using fractal approaches. Fractals are geometrical objects such as curves, surfaces, volumes, and higher-dimensional bodies that have rugged boundaries and obey certain self-similarity behavior. The application of fractals to premixed turbulent flames was first suggested by Gouldin [10].

The most important quantitative parameters of fractal analyses are the fractal dimension (D), the inner and outer cutoff length scales (ε_i and ε_o) – all of which are needed for estimating S_T. In a theoretical study by Kerstein [11], the theoretical maximum for D in three-dimensional Kolmogorov turbulence and for an unstretched turbulent flame was derived to be 7/3 and that this limit being independent of u'_T/S_L. However, numerical simulations by Menon *et al.* [12] suggested that D varied from 2.5 at low u'_T/S_L to 2.75 at u'_T/S_L =20. Experiments by various investigators and summarized by Gulder [13] report values of D varying between 2.1 and 2.4 depending on u'_T/S_L and the experimental configurations. Several of these studies [14,15,16,17] have used D as a representation of the extent of turbulence enhancement on S_T compared to S_L. All known models of the fractal behavior are known to assume the turbulence being homogeneous in the direction of flame front propagation and being statistically time invariant. However, it should be noted that the turbulent kinetic energy naturally decays away from its source unless restored by some external process - this inherent inhomogeneity may compromise the self-similarity that leads to fractal behavior.

There exist a number of techniques to determine the fractal dimension of structures and the dimension of a set may vary depending on the definition being used [32,33,34].

Examples include the box counting method [35], the caliper method [36] and the quadratic method [37]. Studies related to flame topology have shown that the best methods employ the caliper technique [32], which is used here too. In the caliper technique, the length of the flame front is determined at different scales. If the surface is characterized by a single fractal dimension, D, a line of constant slope, given by 1- D, will divide the inner and outer cutoff lengths of the flame, denoted by ε_i and ε_o, [38].Note that if a surface is statistically isotropic, it can be shown that a fractal dimension estimated from these data, $D_2 = D_3$-1, where D_3 corresponds to the fractal dimension of the surface through which the cut is made.

Now, if the number of measuring scales is N and the measuring length of each scale is γ, then the fractal dimension D can be quantified from Equation(3.4).

$$N\gamma^{D} = 1 \Rightarrow D = -\frac{\log N}{\log \gamma} \tag{3.4}$$

Thus, if the object exhibits self-similarity, a plot of *log(N)* vs. *log(γ)* would give a straight line with a slope of $-D$. The length of a wrinkled curve 'L' is therefore the sum of N units, each of length γ, given by Equation(3.5).

$$L \sim N\gamma = \gamma^{1-D} \Rightarrow 1 - D = \frac{\log L}{\log \gamma} \tag{3.5}$$

This self-similar representation is shown in Figure 20(a). The similarity behavior of a fractal phenomenon is expected to break down for sufficiently large and small values of γ, called the outer and inner cutoffs, also shown in Figure 20. This happens either due to the resolution of the measurement or due to the inherent limit on the smallest scale attained based on the physics in play. For turbulent flows, it is reasonable to identify these scales, as the integral (l_o) and Kolmogorov scales (l_K), respectively.

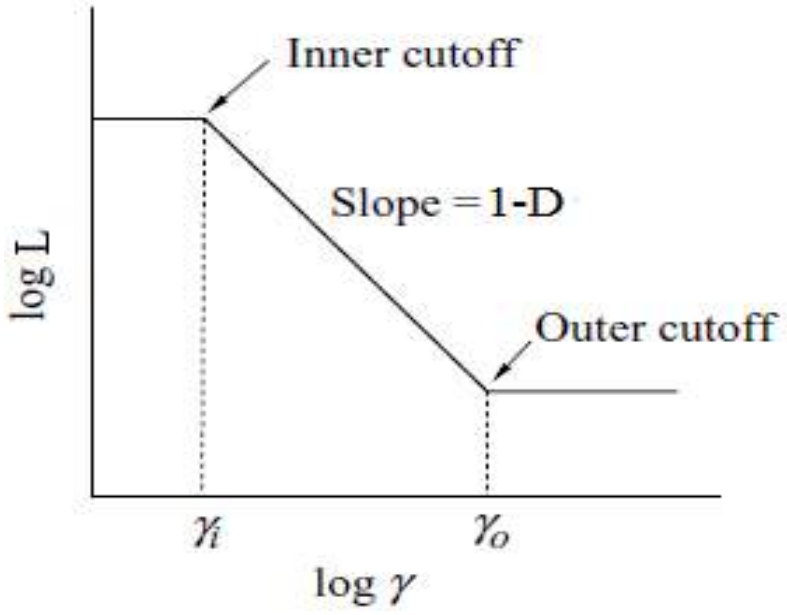

Figure 20: Self-similar representation of a fractal curve for a theoretical case.

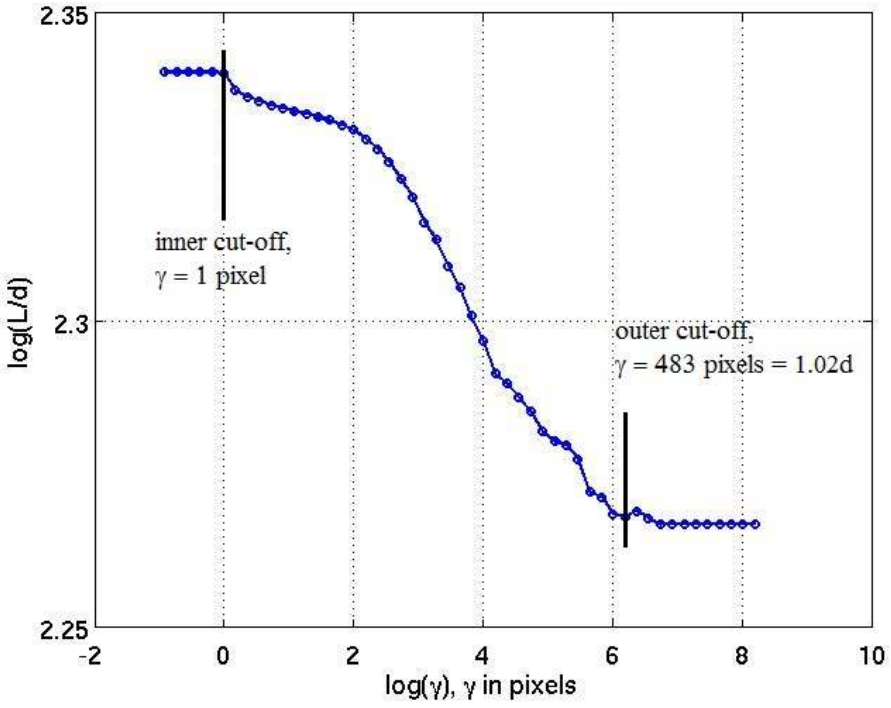

Figure 21: Sample Richardson plot for an acoustically forced Bunsen flame (f_o=200 Hz, u'_a/u_o=0.2, 0^o phase with respect to the forcing signal).

The integral scales can be associated to that of the laminar flame, and the Kolmogorov scales can be associated with the wrinkled turbulent flame, to give Equation(3.6).

$$\frac{S_{T,GC}}{S_L} = \frac{L_T}{L} = \left(\frac{\gamma_{inner}}{\gamma_{outer}}\right)^{(1-D)} = \left(\frac{l_K}{l_o}\right)^{(1-D)} = \mathrm{Re}_o^{3(D-1)/4} \tag{3.6}$$

Further studies by Kerstein [11] have shown that a better representation of the inner cutoff is the Gibson scale (l_G) at which the connected laminar flame structure could be destroyed through flame corrugation and local extinction. Hence, Equation (3.6) along with the energy cascade, becomes

$$\frac{S_{T,GC}}{S_L} = \left(\frac{l_G}{l_o}\right)^{(1-D)} = \left(\frac{u'}{s_L}\right)^{3(D-1)} \tag{3.7}$$

In the case of an unforced flame, the sole source of D would be u'_T/S_L, and hence from Equation (3.7) we can see that for a given u'_T/S_L, the value of S_T/S_L is fixed. In the case of acoustic forcing, even for a given imposed turbulence intensity if the turbulent field is modified this would lead to changes in D and $S_{T,GC}/S_L$ even for a fixed u'_T/S_L.

Local Consumption Speed ($S_{T,LC}$)

The first step in the estimation of the local consumption speed involved the determination of the $\overline{c}$ = 0.5 contour which was found exactly in the same manner as described in the previous section of "Flame Brush Thickness". Next, for each instantaneous image, normals were drawn from the $\overline{c}$ = 0.5 contour to intersect the instantaneous flame front. The area of the instantaneous flame front within consecutive normals or "tubes" was then recorded (accounting for multi-valued flame fronts if necessary). A sample image of the $\overline{c}$ = 0.5 contour, the normals and the instantaneous flame front is shown in Figure 22.

An ensemble average of the area enclosed within each tube at every phase was then recorded. Using mass continuity, the ratio of the ensemble averaged area (A_T) to the tube width (taken as the nominal flame surface area $A_{L,ref}$) is an estimate of the local consumption – see Equations (3.8) and (3.9).

$$\rho_u A_T S_{L,ref} = \rho_u A_{L,ref} S_{T,LC} \tag{3.8}$$

$$\frac{S_{T,LC}}{S_{L,ref}} = \frac{A_T}{A_{L,ref}} \tag{3.9}$$

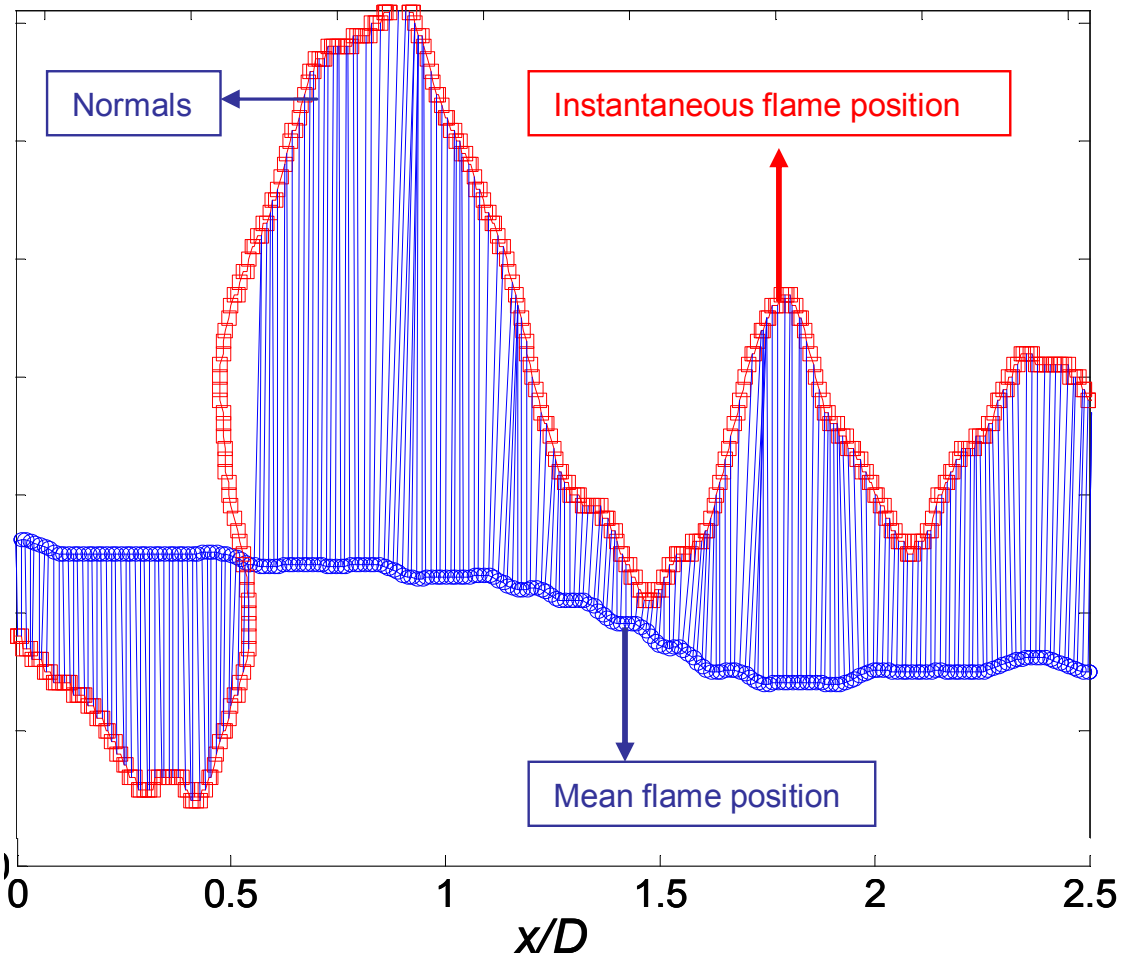

Figure 22: Sample image of normals drawn from the mean ($\bar{c}$ = 0.5) contour to an instantaneous flame edge (red curve) at an acoustic amplitude of u'/u_o = 0.1 and excitation frequency of 300 Hz.

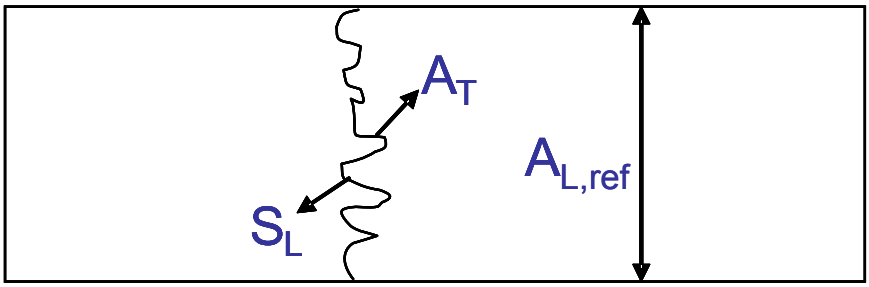

Figure 23: Turbulent Flame Segment.

CHAPTER 4

CHARACTERIZATION OF HARMONICALLY EXCITED SWIRL FLAMES

This chapter presents results of the flame response of the atmospheric swirl combustor to harmonic excitation. Initially, results from the chemiluminescence experiments are presented for the range of conditions encompassing flow velocities, excitation frequencies and amplitudes. The results from the OH PLIF experiments are then presented characterizing the different flame shapes as well as the spatial movement of the different locations of the flame front and the influence of the different regions of the flow field on the flame front. Finally, the different mechanisms influencing the flame response are proposed and presented.

Measurements of the flame response to harmonic forcing

The flame response was measured at different flow velocities, forcing frequencies and amplitudes. The objective of these experiments was to obtain the transfer function of the flame, i.e. the flame response at various acoustic pressure amplitudes; hence a forced system was used rather than a self-excited system. The nozzle exit flow velocities were 21, 30, and 44 m/s, which corresponded to exit Reynolds numbers (based on the nozzle exit hydraulic diameter) of 21,000, 30,000 and 44,000, respectively. At each flow velocity, the flame's global chemiluminescence response (CH* and OH*) was obtained over a range of frequencies and forcing amplitudes. It should be noted that the experiments were checked for repeatability by switching the optical fiber location multiple times while still maintaining the field of view to cover the entire combustor.

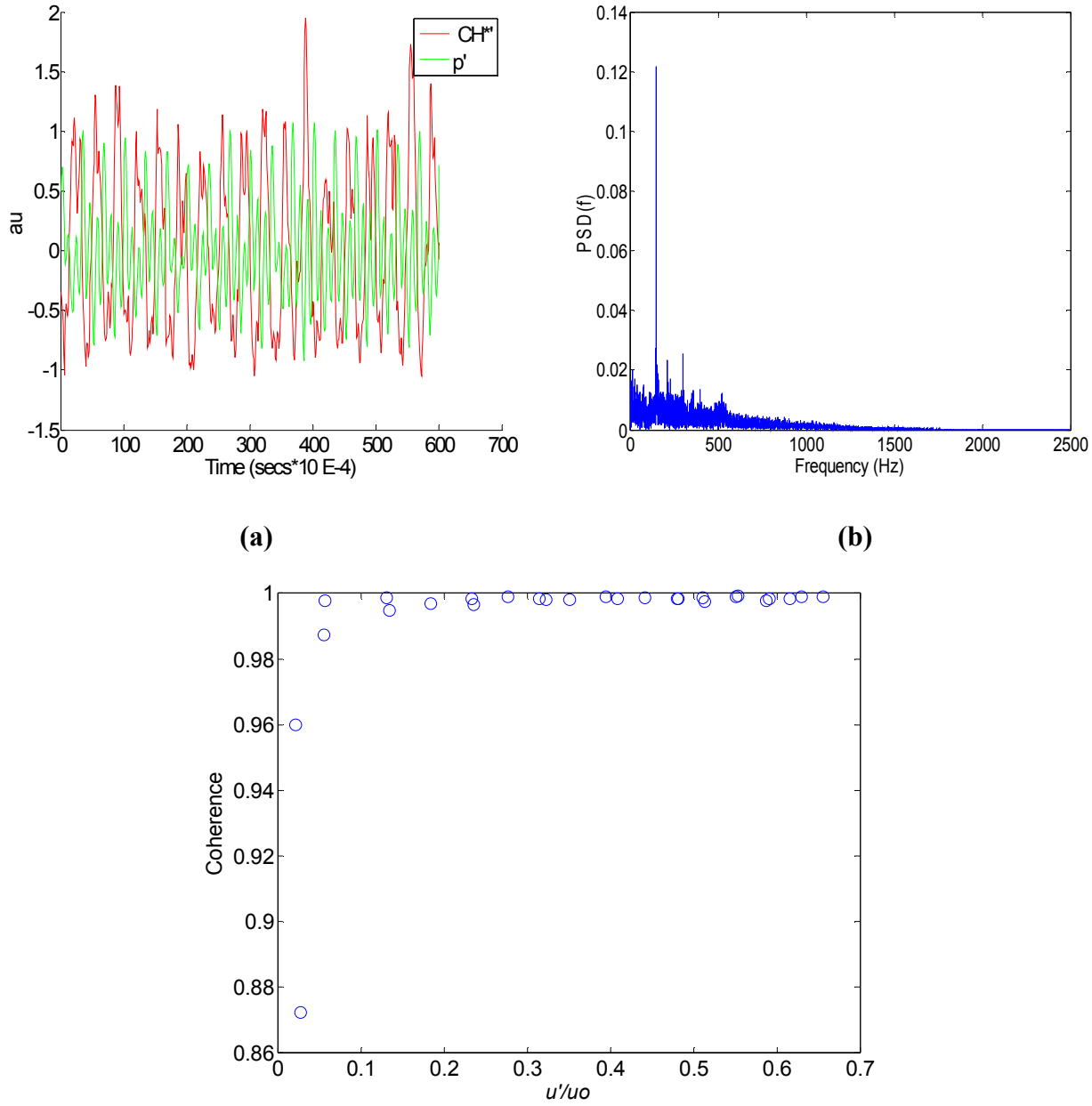

Figure 24 : Sample CH* fluctuations showing (a) time stamps (b) Powers Spectral Density (PSD) and (c) Coherence magnitude at 150 Hz and *Re* = 21,000.

For all conditions of operation, the combustor was always stable i.e. there were no self-excited instabilities inherent in the system.

Figure 24 shows the sample results at a flow velocity of 21 m/s. Figure 24(a) is a

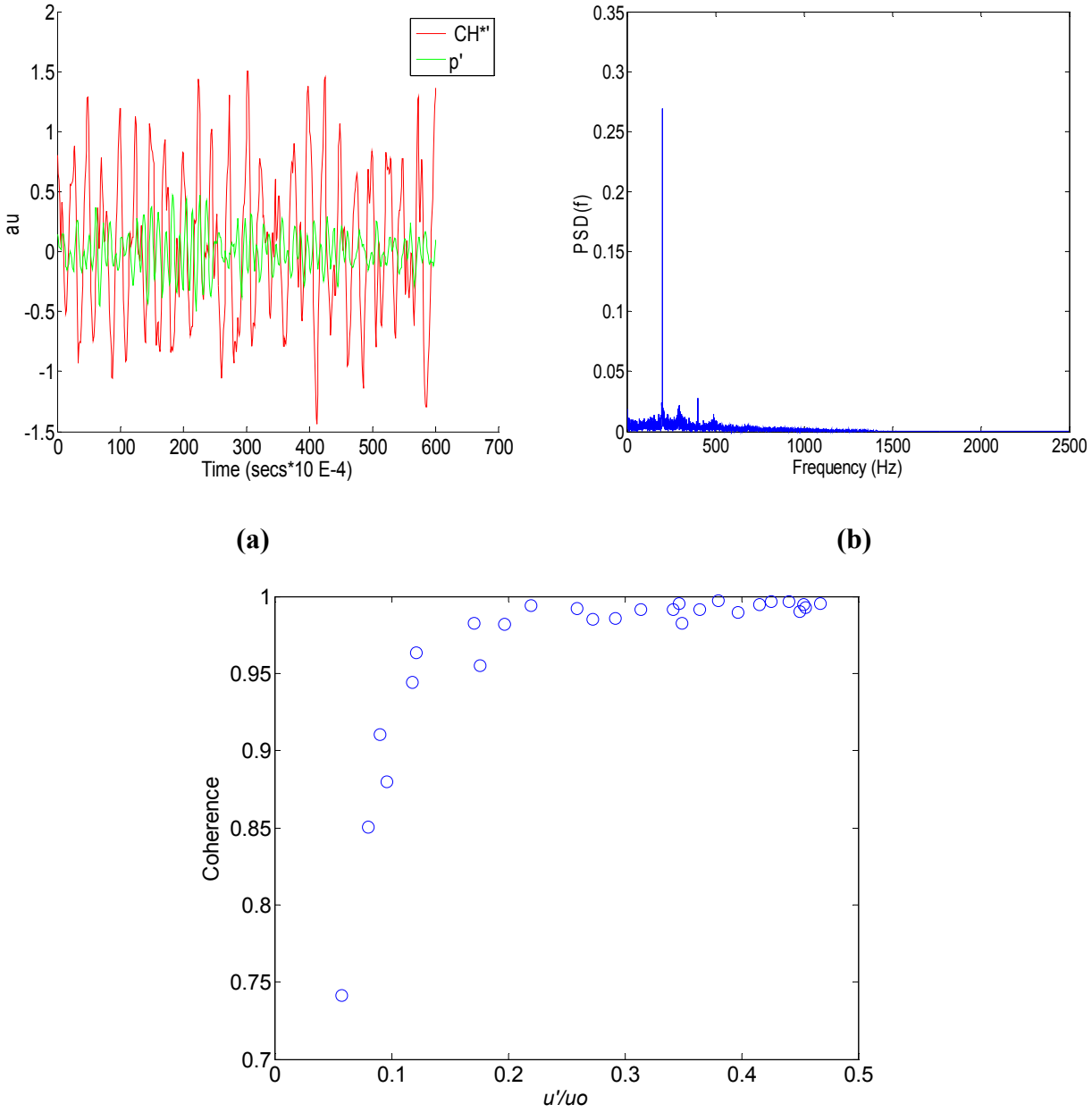

Figure 25 : Sample CH* fluctuations showing (a) time stamps (b) Powers Spectral Density (PSD) and (c) Coherence magnitude at 200 Hz and *Re* = 30,000.

sample plot describing the time series of the fluctuating chemiluminescence signal and one can see the clear harmonic variations of the signal as well as the presence of multiple other frequencies.

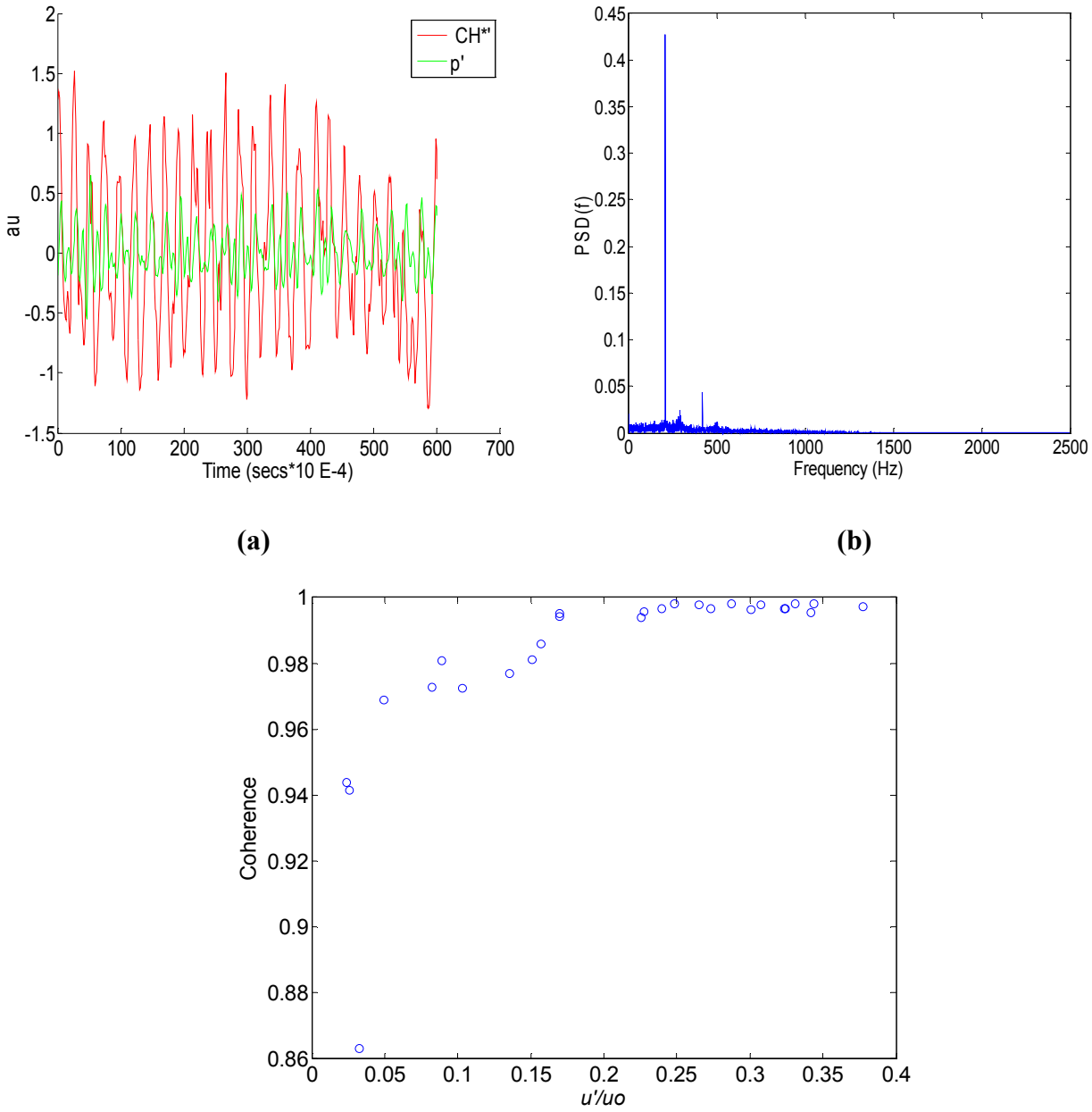

Figure 26 : Sample CH* fluctuations showing (a) time stamps (b) Powers Spectral Density (PSD) and (c) Coherence magnitude at 150 Hz and *Re* = 44,000.

Also shown in this figure is the corresponding pressure trace as recorded by the pressure transducer located just upstream of the combustor. Figure 24(b) shows the

corresponding FFT of both the chemiluminescence and the pressure signal. One can see the clear response peak at the forcing frequency of 150 Hz as well as the presence of the harmonics.

Figure 24(c) shows the coherence plot of the chemiluminescence for the range of amplitudes at the excitation frequency of 150 Hz and Re = 21,000. It can be noted that the coherence magnitude usually remains above 0.9 except for the lowest amplitude of excitation. A high coherence magnitude between the chemiluminescence and the pressure signal indicates a good correlation between the acoustic fluctuations and the heat release fluctuations. Figure 25 and Figure 26, show similar representative plots of the flame response at the flow velocities of 30 and 44 m/s.

The flame response at the forcing frequency was then determined from the frequency spectra of the OH* and CH* signals. The fluctuating part was determined after subtracting the mean component and a FFT was performed to yield the fluctuating amplitude and phase (w.r.t. to the pressure transducer) and the CH*' and OH*'. Note that due to nonlinearities, the flame also responds at harmonics of the forcing frequency. Figure 27 shows a typical comparison between the OH* and CH* signals at the four flow velocities. The variation of the OH* fluctuations followed the same trend as the CH* fluctuations – henceforth, only CH* results are presented.

The flame response at each flow velocity is summarized in the Figure 28, Figure 29 and Figure 31.

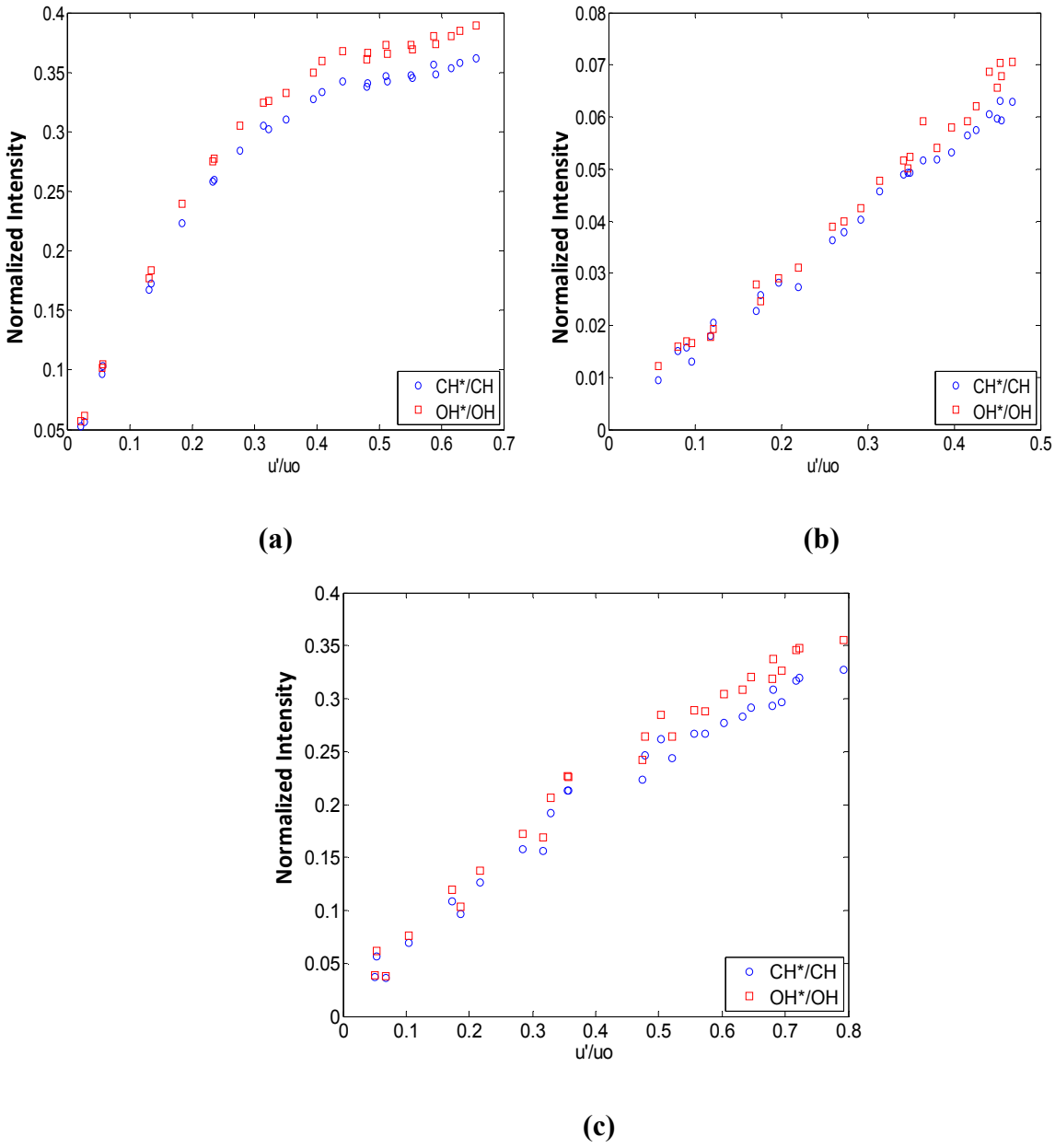

Figure 27 : Comparisons between CH* and OH* response at the forcing frequency of 200 Hz and (a) *Re* = 21,000, (b) *Re* = 30,000, (c) *Re* = 44,000.

The topological character of the flame response can be visualized from the 3-D map and contour plot, while the quantitative details of the flame response can be obtained from the 2-D plot.

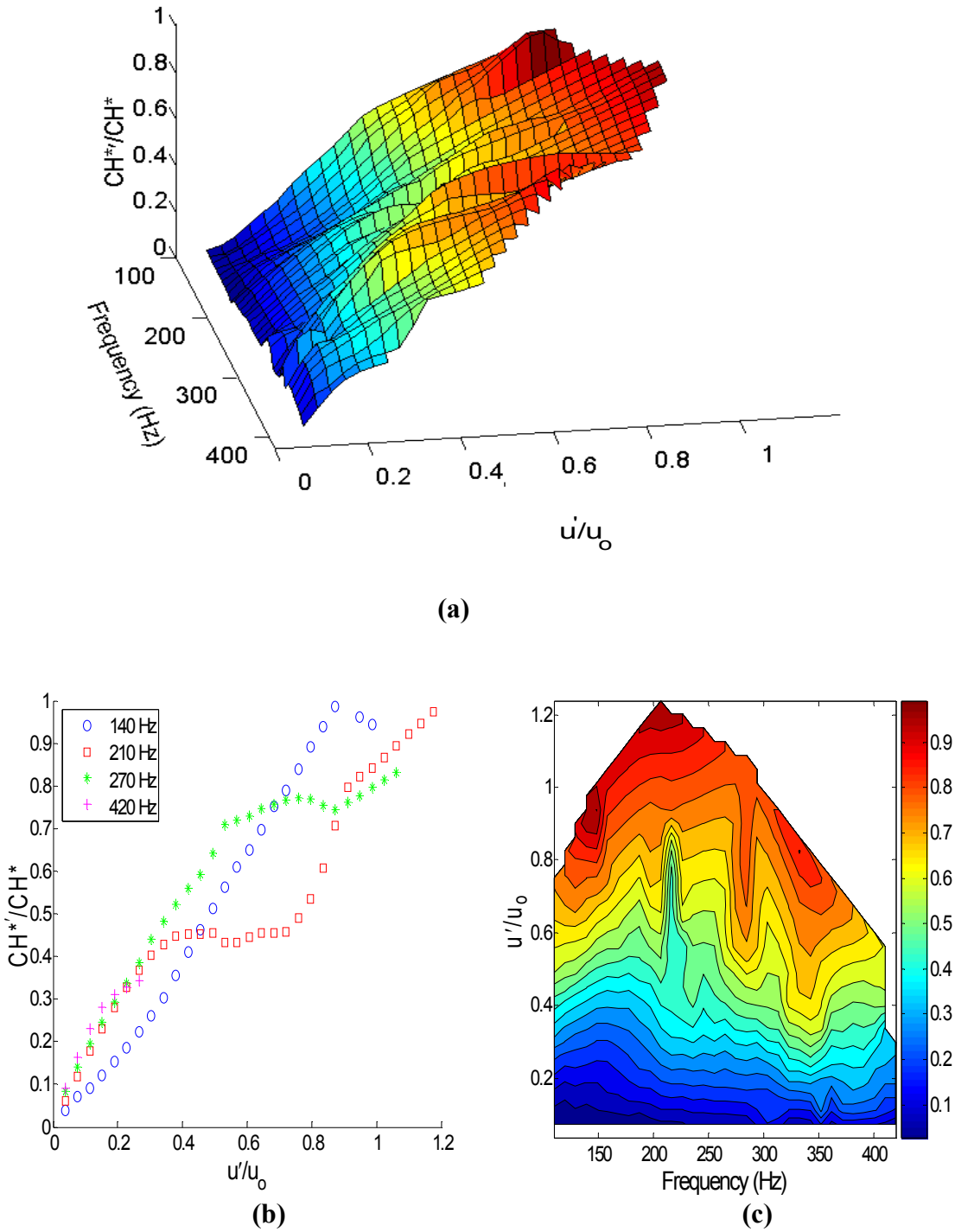

Figure 28 : Three views of the variation of CH*'/CH* with *u'/u$_o$* and frequency at Re = 21,000.

Depending upon the proximity of the forcing frequency to the system's resonance, the range of *u'/u$_o$* amplitudes achievable varies strongly with forcing frequency. In order to

best visualize the topology of these maps, we filled in values from 2-D interpolation in the surface and contour plots. Actual data and attainable data ranges can be determined from the 2-D maps. Note that the attainable dimensionless disturbance amplitude values, u'/u_o, decreases because of the increase in flow velocity u_o; i.e., the attainable u' values stay roughly constant.

We start with the 21 m/s flow velocity case, which nominally exhibits the flame shape shown in Figure 32 (d) in the absence of forcing. Figure 28 (b) describes the variations in the flame response at this flow velocity. Note the initial linear increase in flame response with flow forcing, followed by saturation at chemiluminescence fluctuation levels ranging from 40-100% of the mean. In some cases, the saturation plateau ends with further increases in amplitude and the flame response increases again. Presumably, this is followed by saturation at even higher amplitudes which were generally not attainable in our system – although this is apparently what is happening in the 210 Hz case. These results illustrate that the forcing frequency strongly impacts both the linear gain, as well as initial saturation amplitude.

More global views of the flame response can be inferred from Figure 28 (a) and (c). In interpreting the contour plot at a fixed frequency, it is helpful to note that a nonlinear flame response implies a non-uniform vertical spacing of iso-contours. This graph shows that a number of frequencies were observed where no saturation was observed (e.g.190 Hz) over the amplitude ranges considered. In fact, it shows that the saturation regions occur in very narrow regions in frequency space. This result shows that a range of conditions were observed where no saturation occurred, even at velocity and heat release fluctuation amplitudes with appreciable fractions of their mean value.

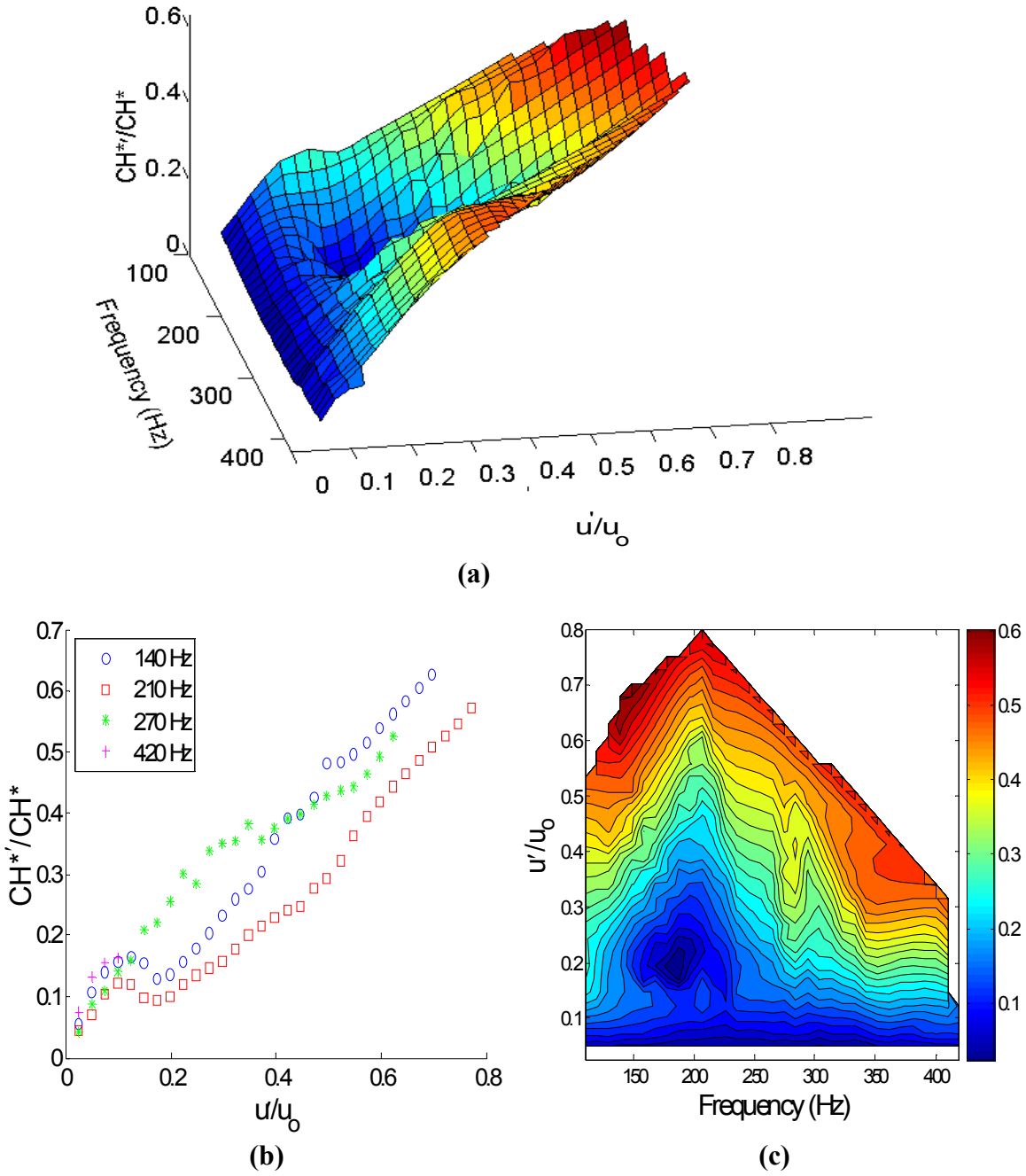

Figure 29 : Three views of the variation of CH*'/CH* with *u'/u$_o$* and frequency at Re = 30,000.

Figure 29 plots these results for the 30 m/s flow velocity case, which nominally exhibits the flame shape shown in Figure 32 (c). Note that the flame is not attached to the inner centerbody but is situated farther downstream. As such, this central, lower

region of the flame is controlled by the vortex breakdown bubble dynamics, while in the 21 m/s case it is probably not.

Here, it can be seen from Figure 29 (a) that in certain frequency ranges the flame response first increases, and then decreases before increasing once again. This decreasing response is quite puzzling as it shows that *increasing forcing amplitude causes a decreasing response* at the forcing frequency. For example, from Figure 29 (b) we see that at the frequencies of 140 and 210 Hz, the flame response drops at $u'/u_o \sim 0.2$.

Figure 29 (c) shows that this non-monotonic behavior is localized in frequency space to the 140 – 240 Hz range. This contour plot also shows the angle of the contours in the frequency space, change slope in moving from the left to the right side of this region. That is, they angle upward at the lower frequencies, implying a decreasing flame response at fixed amplitude and increasing frequency – i.e., low pass filter character. They angle downward at the higher frequencies, implying a high pass filter character.

Figure 31 plots these results for the 44 m/s flow velocity case, which nominally exhibits the flame shape shown in Figure 32 (c). It can be seen that the non-monotonic nature of the flame response is even stronger in this case, as the flame response drops nearly to zero at 270 Hz, u'/u_o=0.2. The frequency regime where the flame response drops now ranges from 210 to 340 Hz, a shift from the 30 m/s flow velocity case. Overall, we observe that at the flow velocities of 30 and 44 m/s, the flame response is non-monotonic with amplitude , as opposed to at 21 m/s. An important point of observation is that at the flow velocities of 30 and 44 m/s velocities and in the absence of forcing, the flame exhibits the shape shown in Figure 32 (c) – as such, a key difference is the flame stabilization by the vortex breakdown bubble, as opposed to the nozzle inner

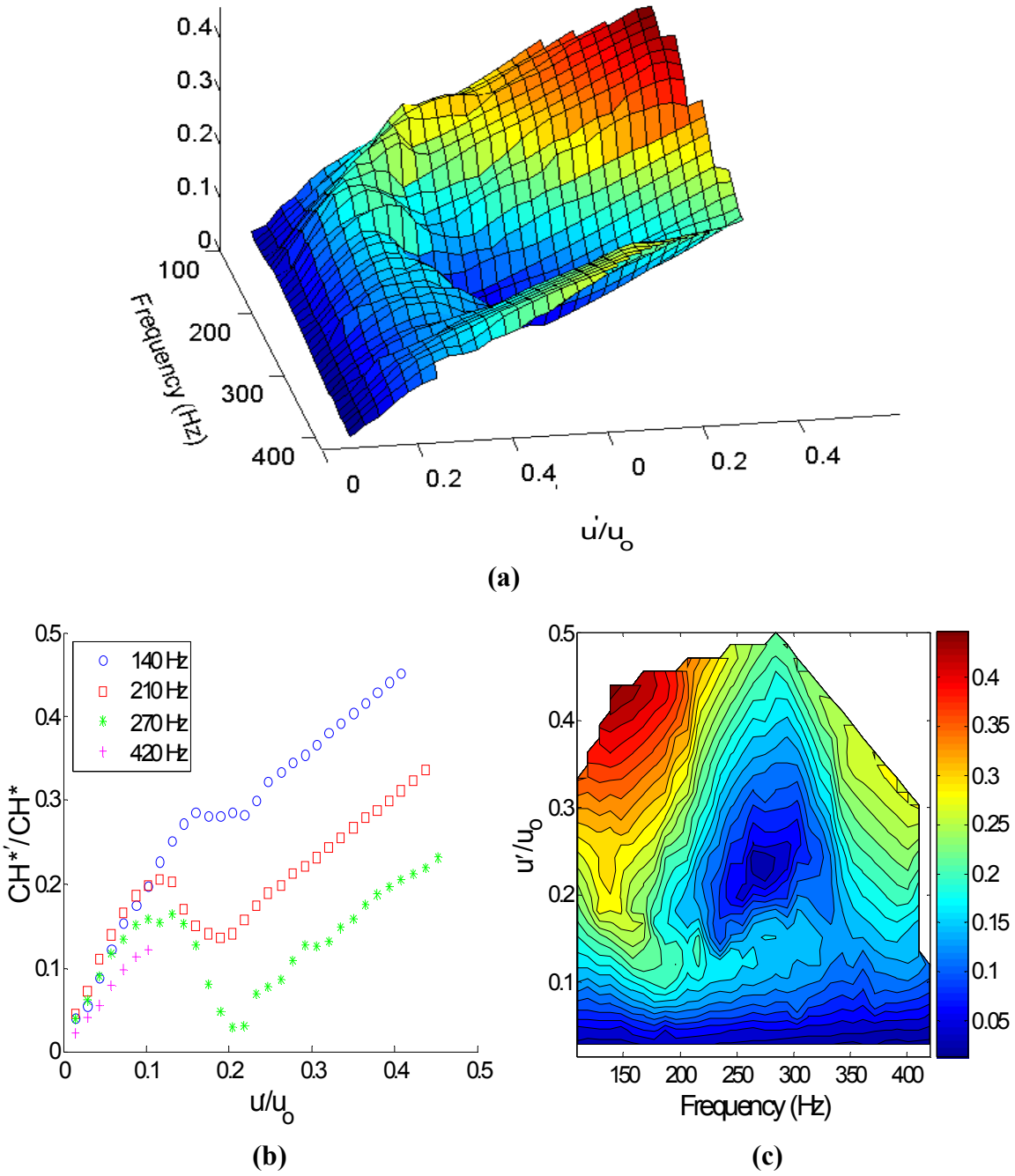

Figure 30: Three views of the variation of CH*'/CH* with *u'/u$_o$* and frequency at Re = 44,000.

annulus.

The phase difference between the chemiluminescence signal and the upstream transducer at different excitation frequencies and amplitudes is shown in Figure 31. From this figure, it can be seen that there is no clear trend existing at the different excitation

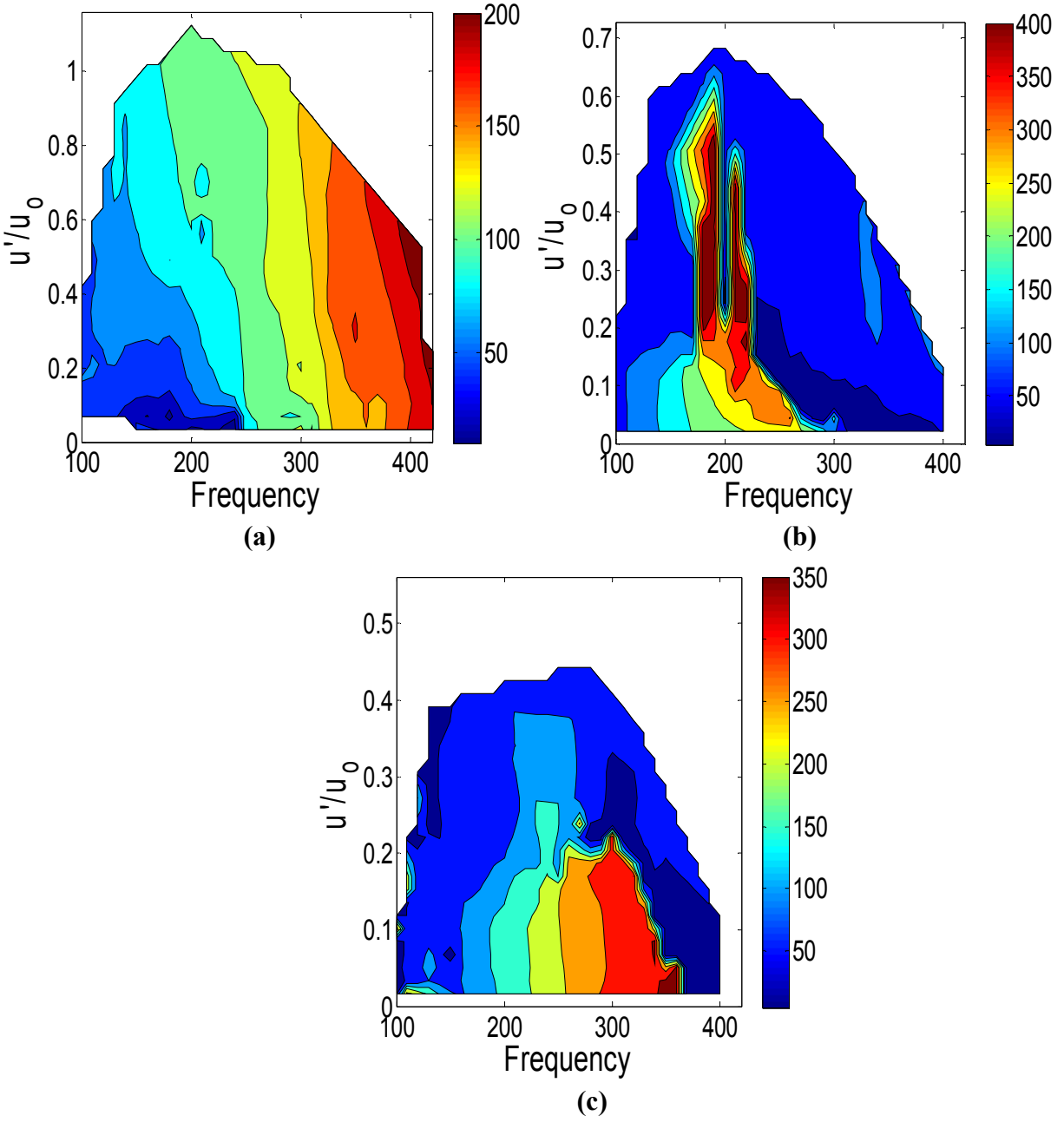

Figure 31: Contour plots of the variation in phase difference (in degrees) between the chemiluminescence signal and the pressure transducer with u'/u_o and excitation frequency at (a) Re = 21,000, (b) Re = 30,000 and (c) Re = 44,000.

parameters or flow velocities. It should be noted that the phase is measured with the pressure transducer located upstream of the combustor section and not in the combustion region. This could have a minor contribution towards the overall observed magnitudes.

The next section attempts to explain the above observed trends in the flame response. As will be detailed later, it can be shown that in the cases where the flame response decreases with increasing driving, the movement of the IRZ can be correlated with the flame response. Numerous mechanisms are presented that are shown to influence the amplitude response of the flames to acoustic excitation. However, it should be noted that despite examining the behavior of the flame front over a wide range of conditions, except for the movement of the IRZ, no other mechanisms were seen to correlate directly with the flame response.

OH – PLIF Image Analysis

To understand the physics underlying the nonlinearities present in the flame response and to trace the changes in the flame structure, OH PLIF images were analyzed. It should be noted that the interpretation of these images are limited by the fact that the flow is actually highly three dimensional with the flame coming in and going out of the images. Also, the consecutive phase images are actually taken several cycles apart.

Now, in order to provide some context for interpreting the results of this study, a brief overview of the key flame and fluid mechanical characteristics of this system are provided below. In a time averaged sense, the flow field consists of four main regions*, see Figure 32: (1) the outer recirculation zone (ORZ), a toroidal recirculating regime generated by the rapid expansion of the nozzle into the combustor, (2) the inner recirculation zone (IRZ, also referred to here as the vortex breakdown bubble), due to vortex breakdown accompanying the swirling flow, (3) the high velocity, annular fluid jet that divides these regions, and (4) two annular shear layers that divide the ORZ and

* In addition, there maybe a small recirculation zone downstream of the centerbody.

annular jet, and the IRZ and the annular jet. Visualizations of these features can also be seen in Huang and Yang [39] and Santavicca *et al.* [40]. Each of these flow features have their associated fluid mechanic instabilities which are highlighted in the next section.

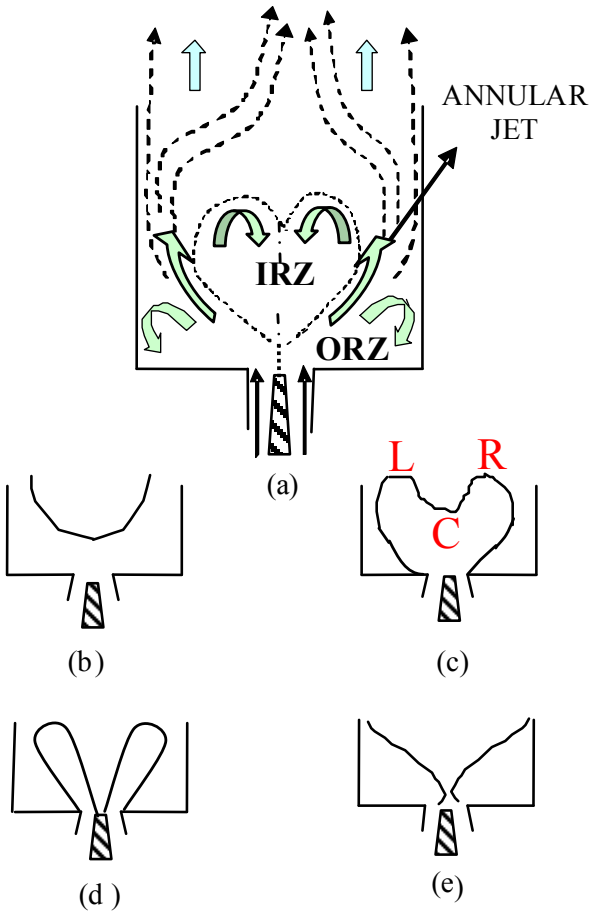

Figure 32: Time averaged base flow field (a) and flame structures (b-e).

Velocity perturbations most visibly affect the flame by modulating the velocity of the annular jet, causing the flame to surge back and forth axially. In addition, they apparently cause the IRZ recirculation strength to fluctuate and to move axially back and forth in location. The perturbations exhibit a similar effect upon the ORZ, apparently causing its strength and axial length to fluctuate. Finally, they influence the shear layer

by synchronizing its rollup due to the Kelvin-Helmholtz instability.

The flame itself can be spatially distributed in several basic configurations, depending upon fuel/air ratio and flow velocities, see Figure 32 *(b)-(e)*. As shown, it can be stabilized in the shear region at the inner center body or outer center body or downstream by the vortex breakdown bubble. How the flame is stabilized plays a crucial role in determining which physical processes control its dynamics. For example, the configuration shown in *(d)* is clearly affected by the dynamics of both shear layers, while that in *(c)* is presumably less affected by the shear layer from the center body. Similarly, the dynamics of the central portion of the flame is strongly influenced by vortex breakdown bubble dynamics in configurations *(b)* and *(c),* while configurations *(d)* and *(e)* are presumably less affected. As will be shown below, the time averaged stabilization location can vary with perturbation amplitude, implying that one set of fluid mechanic processes is important at low amplitudes, and another at higher amplitudes.

A typical set of PLIF images of a flame at six phases of an acoustic cycle and forced at various forcing amplitudes are shown in Figure 33. The forcing frequency here was 140 Hz at a Reynolds number of 44,000, (the corresponding flame response is shown in Figure 32 (c)). The phase angles correspond to the difference in phases between the heat release and the nozzle exit velocity fluctuations. In each of these images, the red lines represent the location of the flame front (marked by the steepest change in the gradient). The nozzle exit is located at the bottom of the image – note that the nozzle image shown in the picture is translated downward from its actual position. Also, it should be noted that only the main flame features have been highlighted and many of the smaller islands that are present have not been outlined.

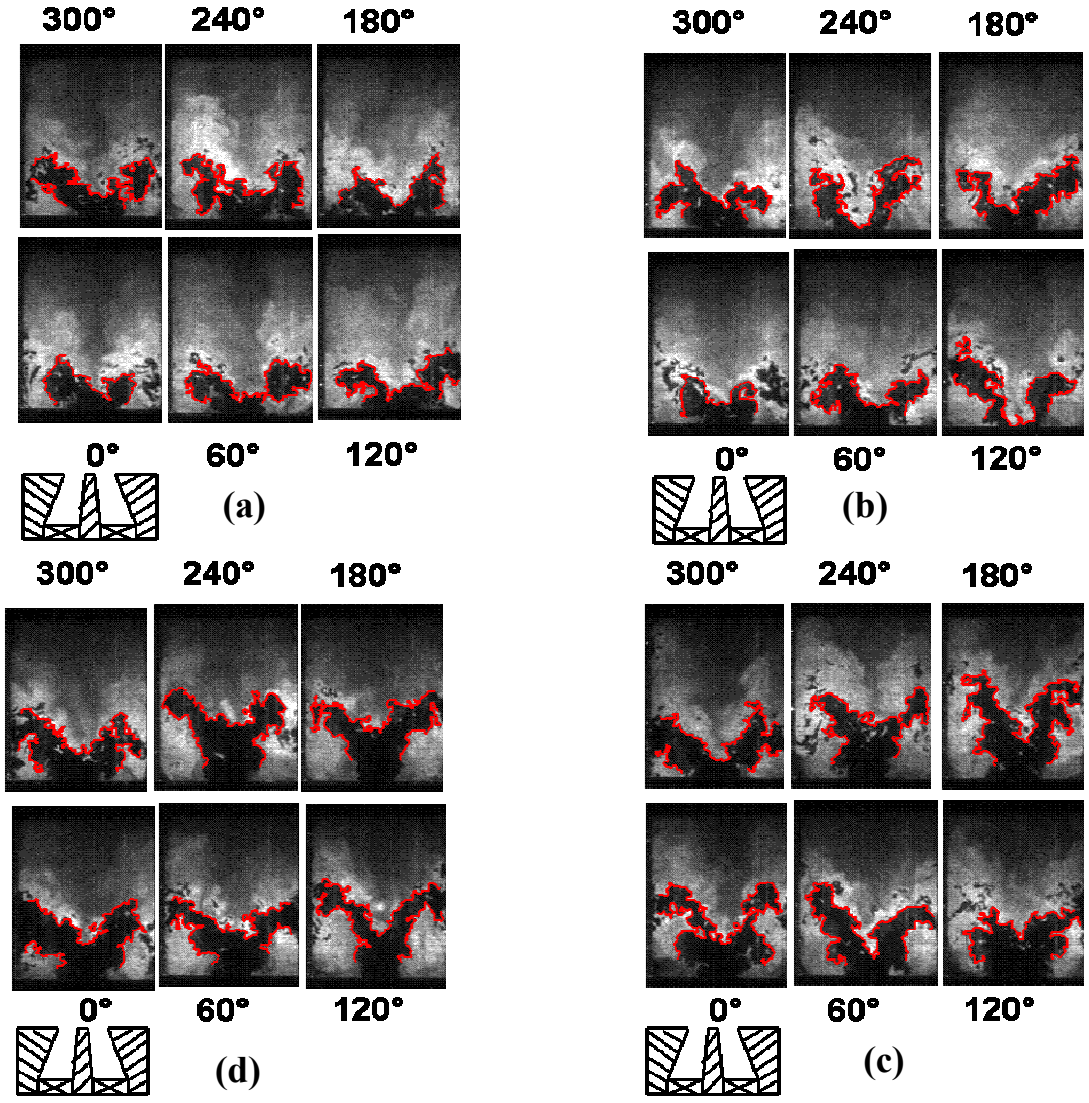

Figure 33: OH PLIF images showing flame structure at the forcing frequency of 140 Hz, Re=44,000 and amplitudes of (a) u'/u_o = 0.07, (b) u'/u_o = 0.1, (c) u'/u_o =0.17 & (d) u'/u_o =0.24.

At this condition, the flame is attached on the outer annulus but not to the inner one, similar to what is shown pictorially in Figure 32 (c). Figure 33 (a) and (b) describe the flame structure at low forcing amplitudes; i.e. in the linear regime of flame response. Figure 33 (c) & (d) are images of the flame under large forcing amplitudes, and correspond to the cases where the flame response saturates, and when the flame response

starts rising once again after the saturation regime, respectively. In general, from Figure 33, it can be seen that the flame is surging back and forth axially, due to the oscillating flow velocity in the annular jet region shown in Figure 32 (a). This phenomenon is well illustrated in Figure 33 (d) – at various phase angles, the flame in the ORZ and "Jet" region is moving up and down - hence resulting in fluctuations of the overall flame length. The overall level of fluctuation of the flame length is seen to grow with forcing amplitude. Moreover, the size of the ORZ is also modulated, as is evident from the oscillating angle of the flame front facing the ORZ (e.g., compare the images at 180 and 300 degrees). Further, at higher forcing amplitudes, the location of the flame at the centerline is oscillating axially, suggesting a corresponding fluctuation in location of the vortex breakdown bubble.

Forced Flame Results

From the discussion in the previous section (see Figure 32), it can be seen that the key physical processes controlling the response of the flame to acoustic oscillations are jointly controlled by fluid mechanics and the flame configuration. Based upon analysis of several thousand instantaneous OH PLIF images, four key processes are proposed: (1) flame stabilization, (2) annular jet fluctuations, (3) excitation of and flame interactions with wake mode, jet column, swirl flow, and Kelvin-Helmholtz fluid mechanic instabilities, and (4) turbulent flame speed and brush development. Flame stabilization and flame interaction with the jet column have been addressed by others including Bellows *et al*.[12] and Balachandran *et al.* [15], while the remaining mechanisms remain to be understood and are addressed separately in the sub-sections below. The last mechanisms of turbulent flame speed and brush development influencing the flame

response are taken up in detail in the next chapter.

Some of these processes appear in isolation, but they usually appear in combination with others. For example, oscillations of the jet and inner recirculation zone usually occur simultaneously – however, they may not have the same phase or amplitude dependence.

Fluctuating annular jet velocity

Because of sufficient swirl in the flow, vortex breakdown occurs, leading to flow reversal which, in a time-averaged sense, is equivalent to placing a blockage in the flow. This causes the axial flow to remain in an annular, high speed fluid column, between the IRZ and ORZ. Acoustic excitation causes an oscillatory flow velocity in the jet between the IRZ and ORZ, causing a fluctuation in flame length and, therefore, heat release due to the expanding and contraction of the flame surface area.

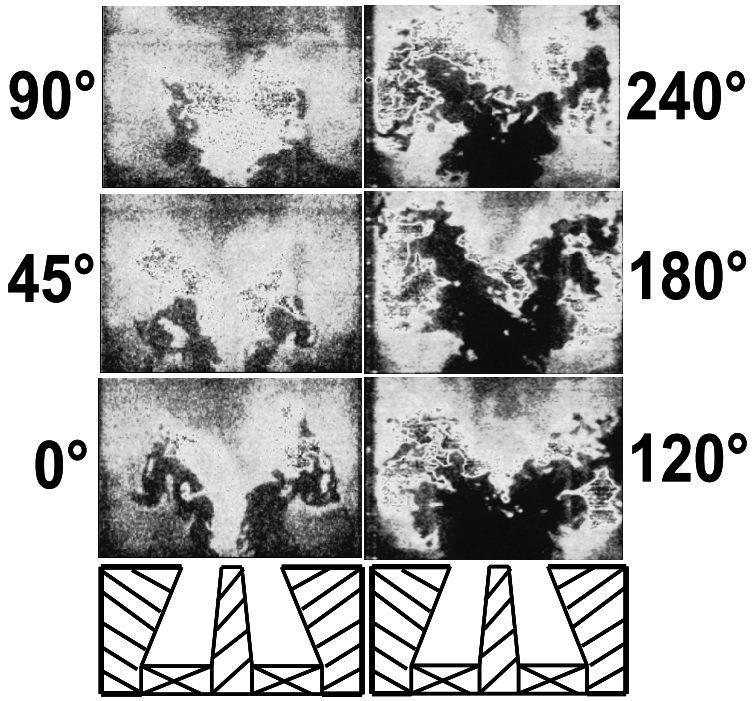

Figure 34: OH PLIF images showing flame structure at *(a) Re*=21,000, forcing frequency 410 Hz and u'/u_0 = 0.3 *(b) Re*=44,000, forcing frequency 270 Hz and u'/u_0 = 0.21.

Two sets of PLIF images of a flame at three sample phases of an acoustic cycle are shown in Figure 34 (indicated phase angles are with respect to excitation source). At the lower velocity condition of *Re*=21,000, the flame can be seen attached to the inner annulus. At *Re*=44,000, the flame is attached on the outer annulus but not to the inner one, similar to what is shown in Figure 32 *(d)* and *(c)*, respectively. In general, from Figure 34, it can be seen that the flame is surging back and forth axially, due to the oscillating flow velocity in the annular jet region. These oscillations result in fluctuations of the overall flame length which also increases with forcing amplitude.

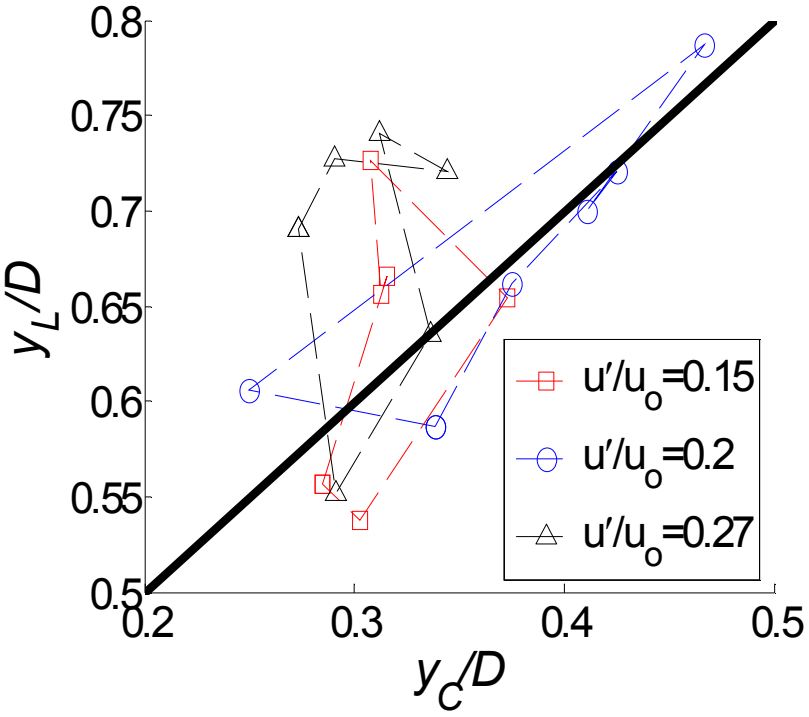

Figure 35: Relationship between ensemble averaged axial locations of the left branch flame length (y_L) and flame center (y_C) across an acoustic cycle, for different disturbance amplitudes (f=210 Hz, Re = 44,000).

The relationship between the oscillating fluid velocity in the annular jet (and, therefore, oscillations in flame length) and that at the nozzle exit depends also on the corresponding dynamics of the ORZ and IRZ.

For example, if the IRZ and ORZ size and location remain unaffected, then there is a one-to-one correspondence between the fluctuating volume flow at the nozzle exit and cross-sectional slices of this annular region at various downstream locations, as dictated by mass conservation. If, however, during a point of high nozzle exit velocity, the IRZ leading edge moves downstream and/or the ORZ or IRZ shrinks in size, then the annular cross sectional area can change as well, complicating the relationship between nozzle exit and annular jet velocity and, therefore, the response of the flame position.

To illustrate this point quantitatively, the ensemble averaged flame position at the maximum y (axial) location on the left and right sides of the centerline, as well as the near-centerline minimum, were calculated at each phase, referred to as positions L, R, and C in Figure 32 *(c)*. The uncertainty in ensemble averaged location, Δ, is approximately $\Delta(x,y)/D = 0.02$, where D is the combustor diameter. Figure 35 plots the relationship between the ensemble averaged locations of the axial coordinate of the positions L and C through an acoustic cycle. The solid line has a slope of unity and illustrates the limiting behavior of fluctuations in-phase and with equal magnitude. It can be seen that these fluctuations are not generally in phase (i.e., the locus of points traces out a rotated ellipse), or of the same magnitude. At the lower amplitude conditions, point L is clearly moving with a larger magnitude than point C, while their fluctuation magnitudes are similar at the largest forcing amplitude.

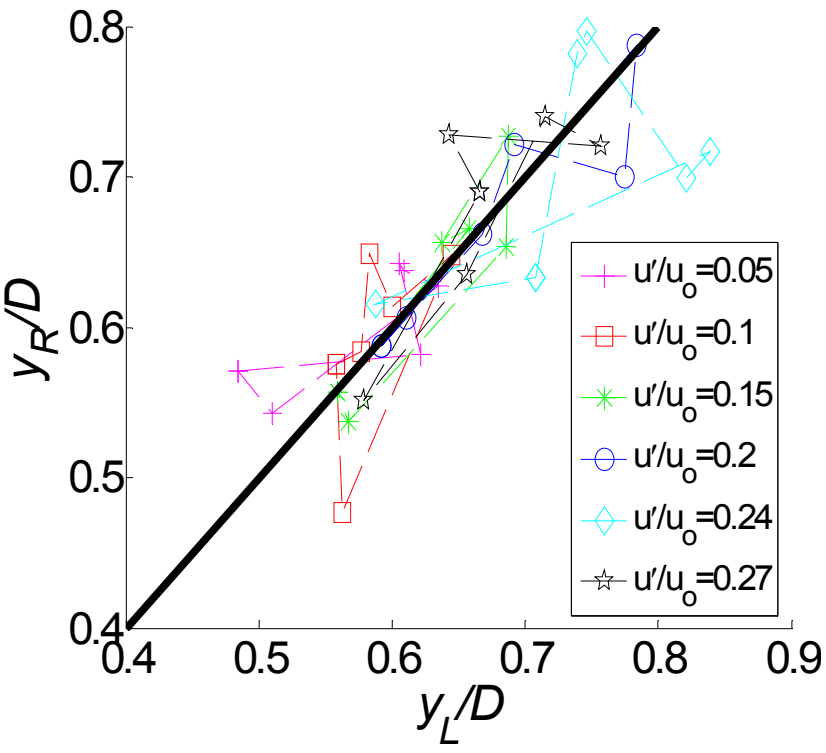

Figure 36: Relationship between ensemble averaged axial locations of the right (y_R) and left (y_L) flame lengths across an acoustic cycle, for different disturbance amplitudes (f=210 Hz, Re = 44,000).

In contrast, points *L* and *R* were found to always move in phase and with the same magnitude, as shown in Figure 36. This illustrates that the annular jet fluctuations are axisymmetric and do not appear to be precessing around the centerline (evidence for precession of point *C* was observed, however, see Figure 41).

Flame interactions with fluid mechanic instabilities

The fluid mechanics of a swirl combustor is complex, due to several inherent flow instabilities which are simultaneously present.

i.Swirling Annular Jet Column and IRZ Dynamics

The swirling jet column possesses a range of instabilities ranging from helical disturbances to strong spiral and axisymmetric vortex breakdown states [41,42,43].

While the influence of these helical and spiral modes is difficult to elucidate from planar images, the axisymmetric rollup of the flame into the IRZ is clearly evident under certain conditions, such as shown in Figure 37 *(a)* by Bellows *et al*.[12].

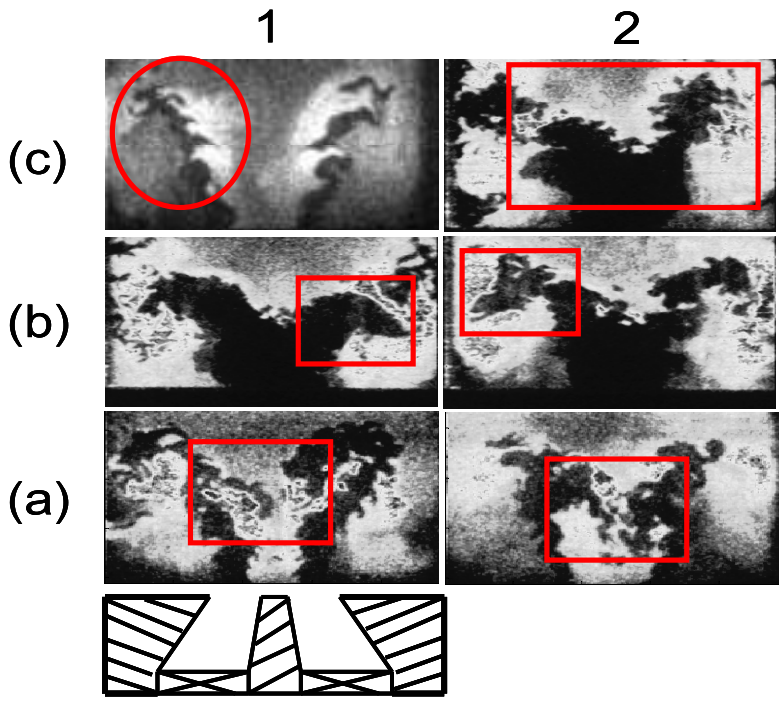

Figure 37: PLIF images showing *(a)* vortex rollup in IRZ at 130 Hz, *Re*=21,000, u'/u_0 = 0.9 (Bellows *et al*.[12]), *(b)* vortex rollup in ORZ at 210 Hz, *Re*=44,000, u'/u_0 = 0.2 and (c) shear layer instabilities manifested in the flame at 130 Hz, *Re*=21,000, (1) u'/u_0 = 0.2 and at 270 Hz, *Re*=44,000, (2) u'/u_0 = 0.05.

In addition, the location and width of the IRZ oscillates axially. This has important influences upon the flame dynamics for situations where the flame is IRZ stabilized, as in the two configurations shown in Figure 32 *(b)* and *(c)*. In general, the dynamics of the bubble itself are not well understood (even in the non-reacting case) and the results from this indicate that it has complex frequency-amplitude dependence.

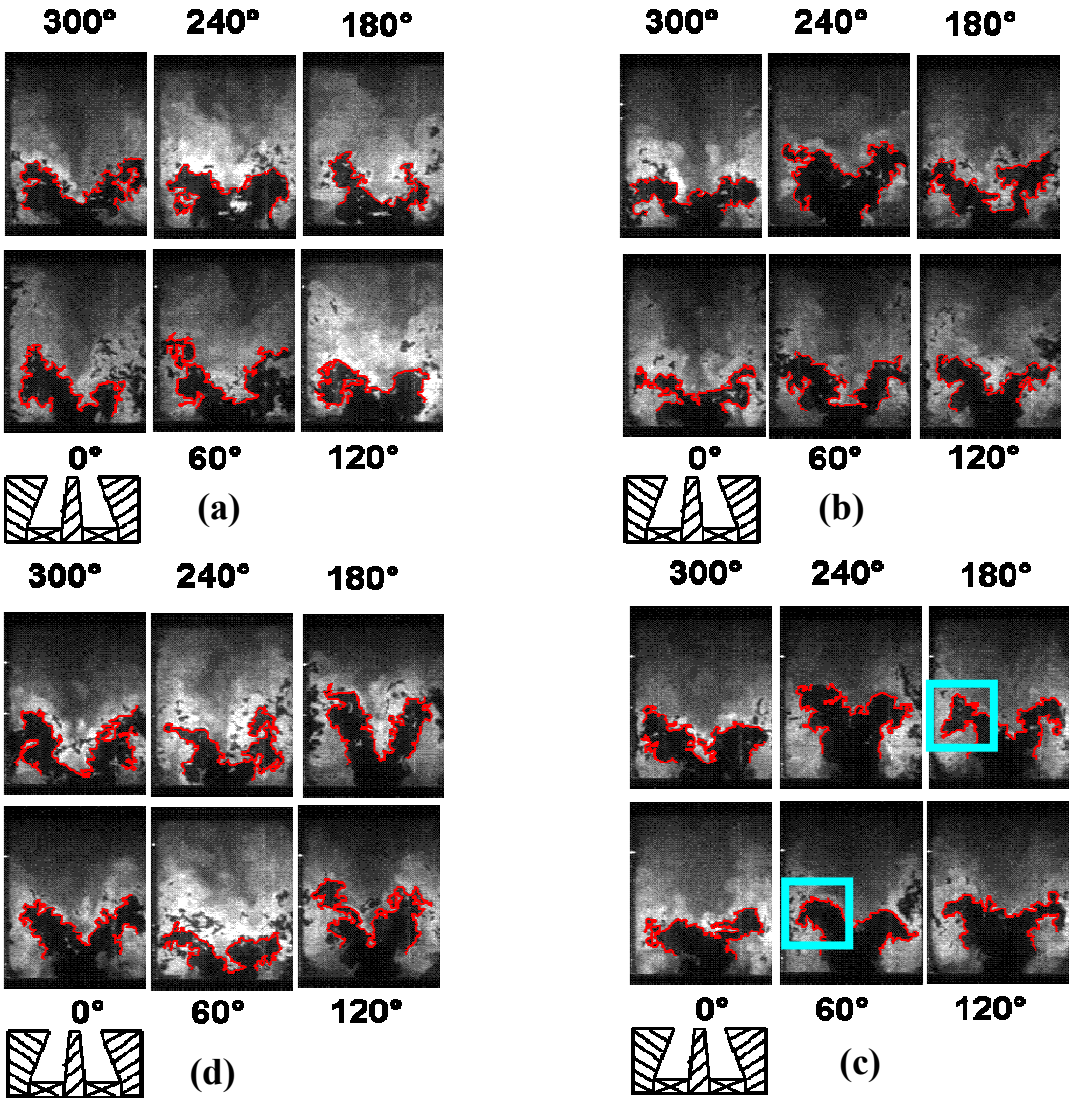

Figure 38: Flame locations at the forcing frequency of 210 Hz, Re=44,000, and amplitudes of (a) u'/u_0= 0.05, (b) u'/u_0= 0.13, (c) u'/u_0=0.2 & (d) u'/u_0=0.25.

Another feature that can be observed from these images is the movement of the vortex breakdown bubble, the IRZ, due to the external forcing. Figure 33 (a), taken at 140 Hz and u'/u_0 = 0.07 illustrates this phenomenon – moreover, it appears that the recirculation bubble oscillates at frequencies higher than that of the forcing.

In addition, if we look closely at Figure 33 (c), taken at u'/u_0 = 0.17 (where the flame response saturated) it can be seen that the flame position at the centerline barely

oscillates, indicating minimal oscillations in IRZ location. Furthermore, at the next higher forcing amplitude, u'/u_0 = 0.35, where the flame response again grows with perturbation amplitude, the location of the flame centerline begins to oscillate again - see Figure 33(d).

This behavior should be contrasted with the 210 Hz forcing frequency case, where the flame response exhibits non-monotonic amplitude dependence. It can be observed from Figure 38 that the location of the breakdown bubble is oscillating in all the images.

The dynamics of the flame forced at 270 Hz are of special interest, as the flame response is non-monotonic (as in the 210 Hz case) and nearly drops to zero at u'/u_0 = 0.21. From Figure 39 (a), taken at u'/u_0 = 0.05 where the flame response is well within the linear regime, we observe that the IRZ is oscillating axially. The same may be observed in Figure 39 (b), taken at u'/u_0 = 0.14, where the flame response reaches a local maximum. It can be seen that the magnitude of fluctuations of both the breakdown bubble and annular jet region is larger, as might be expected. Figure 39 (c) shows the flame response at u'/u_0 = 0.21, where the flame response at the forcing frequency is nearly zero. These images show that the IRZ location undergoes relatively small translational changes in its position, as compared to the lower forcing amplitude cases. Finally, Figure 39 (d) plots the flame response at u'/u_0 = 0.35, where the flame response again grows with perturbation amplitude. The axial movement of the IRZ, the flame position in the annular jet, and some rollup of the flame into the ORZ are all evident in these images.

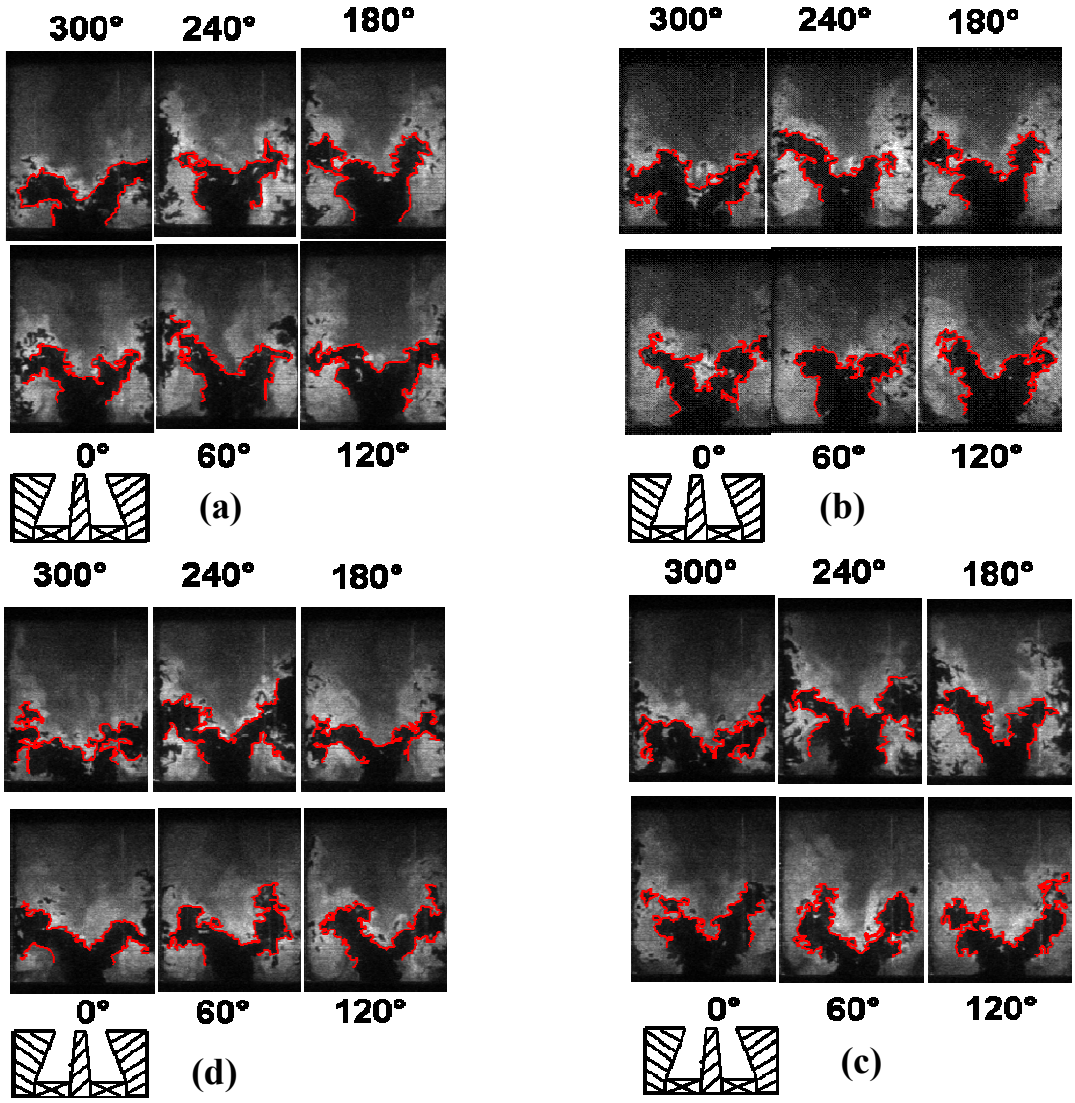

Figure 39: Flame locations at the forcing frequency of 270 Hz, Re=44,000 and amplitudes of (a) u'/u_0= 0.05, (b) u'/u_0= 0.14, (c) u'/u_0=0.21 & (d) u'/u_0=0.35.

Figure 40(a) and Figure 41 (a), plot the location of the flame front at the excitation frequency of 210 Hz - where a slight dip in flame response occurs at u'/u_o = 0.2, show that increased amplitude velocity fluctuations result in larger fluctuations in flame length and flame stabilization point *C*.

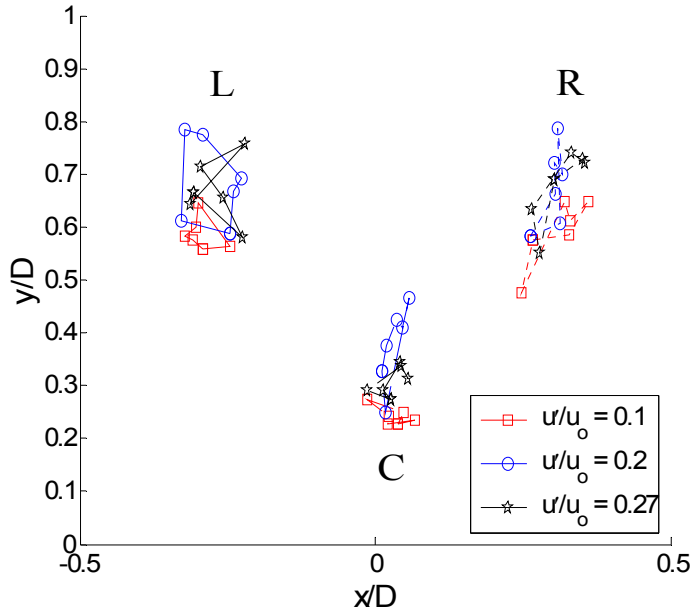

(a)

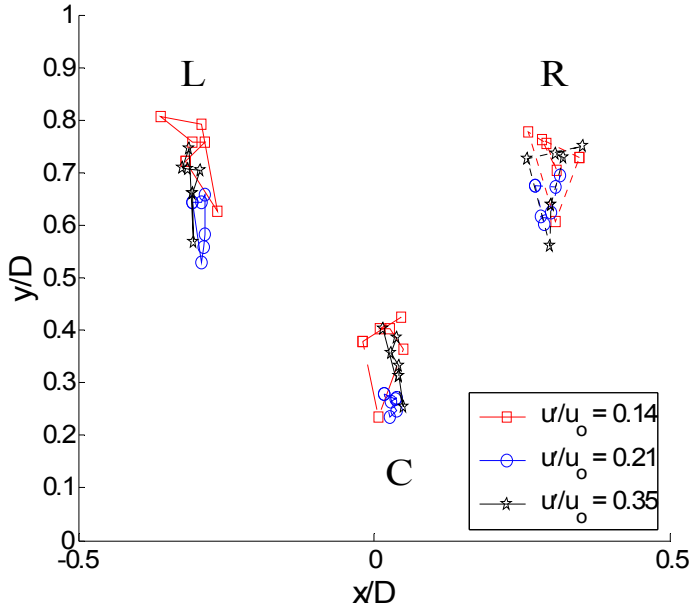

(b)

Figure 40: Locations of the flame positions L, C and R across an acoustic cycle for different disturbance amplitudes and forcing frequencies of (a) 210 Hz and (b) 270 Hz at Re = 44,000.

In addition, the apparent precession of the IRZ is evident by the simultaneous oscillation of the *x* location of point *C* through the cycle; see Figure 41 (a). At the

highest amplitude velocity fluctuation, u'/u_0 = 0.27, the fluctuation in point *C* is somewhat reduced and the flame length fluctuation is roughly the same as at u'/u_0 = 0.2. The correlation between fluctuations in the *y* location of points *C* and *L* is shown in Figure 42. This plot indicates that these fluctuations are in phase (i.e., y_c and y_L increase and decrease together).

Figure 40(b) and Figure 41 (b) plot the variation in the positions of *L*, *C* and *R* with perturbation amplitude at the forcing frequency of 270 Hz where the flame response experiences significant non-monotonic behavior and essentially goes to zero at u'/u_0 = 0.2. Both figures show that at the lower and higher amplitude cases of u'/u_0 = 0.14 and 0.35 the vortex bubble and the annular jet regions show significant fluctuations.

However, at u'/u_0 = 0.21 both the base of the flame and the annular jet regions seems to undergo very little fluctuation as can be observed from Figure 35. In particular, the amplitude of fluctuation of y_c is negligibly small. Moreover, its level of fluctuation across the whole disturbance amplitude range seems to mirror that of the overall transfer function. These oscillations are manifested in fluctuations in the location of point *C*; see Figure 41, which plots the variation in the radial and axial positions of point *C* across the acoustic cycle at several perturbation amplitudes.

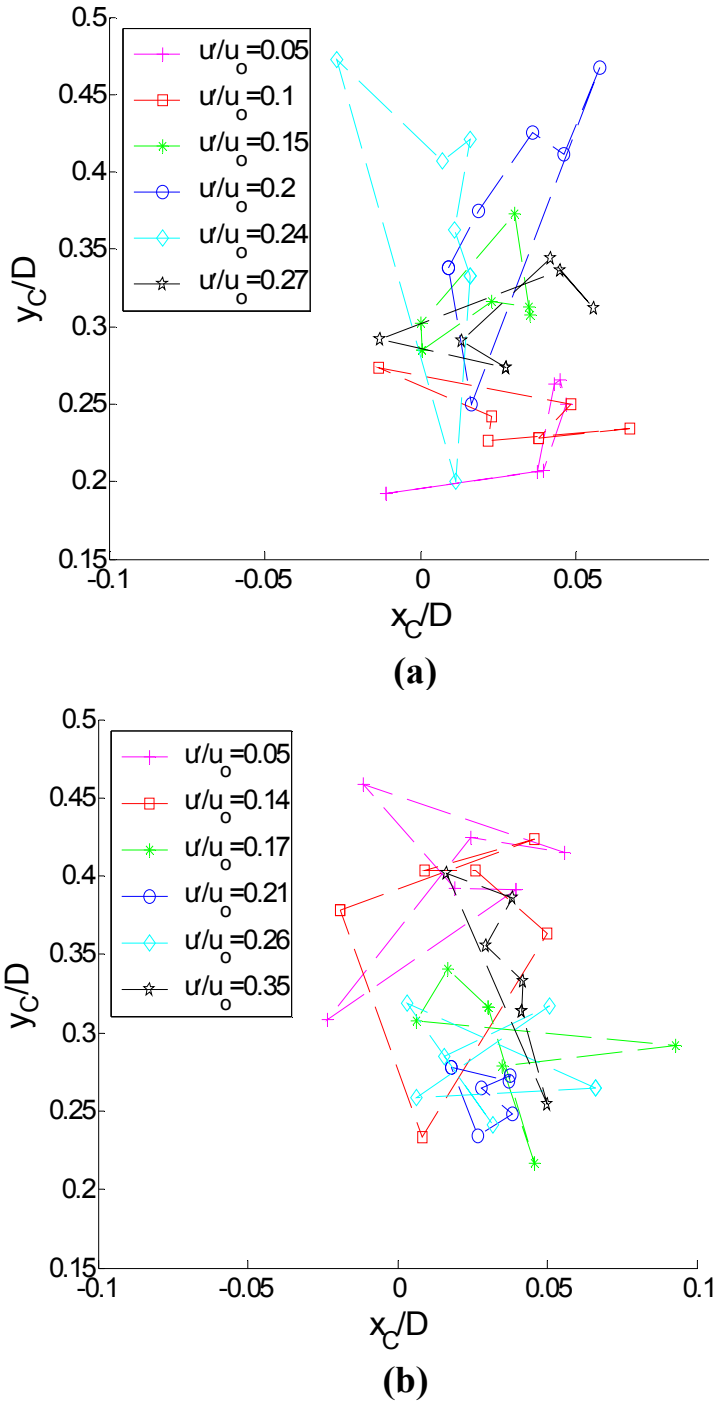

Figure 41: Locations of the flame position C across an acoustic cycle for different disturbance amplitudes and forcing frequencies of (a) 210 Hz and (b) 270 Hz at Re = 44,000.

From this figure, it can be seen that the amplitude of the axial response of point *C* is not monotonic with disturbance amplitude – in fact, in some cases, an increase in

perturbation amplitude results in decreasing the amplitude of fluctuation of point *C*. For example, in Figure 41 (b), with an increase in excitation amplitude of 0.14 to 0.21, the amplitude of fluctuations decreases while a further increase in amplitude to 0.35 causes an increase in the fluctuation amplitudes. These trends mirror those of the overall flame response at this flow condition (see Figure 31), suggesting a relationship between the non-monotonic flame response to disturbance amplitude with the IRZ bubble dynamics.

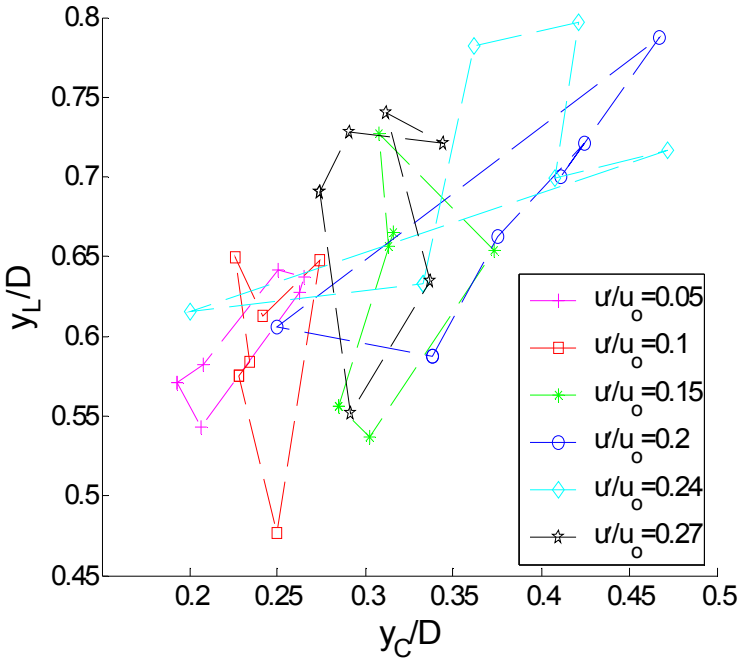

Figure 42: Relationship between ensemble averaged y locations of the left branch flame length (y_L) and flame center (y_c) across an acoustic cycle, for different disturbance amplitudes and forcing frequencies of (a) 210 Hz and (b) 270 Hz at Re = 44,000.

ii. ORZ Dynamics

The rapid expansion at the dump plane causes wake-type mode instabilities, as discussed by Najm and Ghoneim [44]. As shown in their simulations, the recirculating flow in the ORZ periodically detaches and travels downstream. This strongly

recirculating flow influences the annular jet trajectory under certain circumstances, causing it to roll-up in the outward direction, see Figure 37 *(b)*. As in the related case for roll-up into the IRZ, this process is amplitude dependent and grows in prominence with increasing disturbance amplitude.

From our experiments, we have also observed cases where vortex rollup occurs towards the outer recirculation zone. Figure 38 shows the flame structure at a Reynolds number of 44,000 and at a forcing frequency of 210 Hz. As shown in Figure 31 the corresponding flame response from chemiluminescence measurements begins to decrease at u'/u_0 =0.13, and then rises monotonically for $u'/u_0 > 0.2$. Figure 38 (a) illustrates the flame response through the cycle at u'/u_0=0.05, which lies in the initial linear regime. At this low forcing amplitude, we see that the flame oscillates back and forth, apparently due to velocity oscillations in the annular jet. There is not much fluctuation in the IRZ region. At the forcing amplitude of $u'/u_0 = 0.13$, (where the flame response begins to fall) the corresponding images of the flame are shown in Figure 38 (b).

Figure 38 (c) shows the flame structure at u'/u_0 =0.2-the forcing amplitude where the flame response is near the local maxima. The phenomenon of vortex rollup in the ORZ (indicated by the square marked regions) can be seen from these images. It can also be seen that the flame front seems to be flat in most cases - with the result that the flame surface area and consequently the heat release decreases. Figure 38 (d) shows the flame response at u'/u_0 =0.25, where the flame's heat release is growing with amplitude. It can be seen that the base of the flame fluctuates wildly in addition to the fluctuations in the "Annular Jet" region – this indicates a strong axially oscillating position of the IRZ.

In addition, pockets of the flame can be seen in the ORZ for select cases (e.g., see

Figure 38 (d), phase angle 300^0), hence indicating that the recirculation zones are affected independently by the external forcing. The images also indicate that several complex flow processes – in this case, rollup of the flame into the ORZ and oscillations in the flame base position due to axial fluctuation in the IRZ position, can occur simultaneously. Additional images of the rollup into the ORZ are presented in Figure 43 for two conditions – at low flow velocities (in which the flame was attached to the center body) as well as higher flow velocities (where the flame was lifted off and attached to the outer annulus of the nozzle).

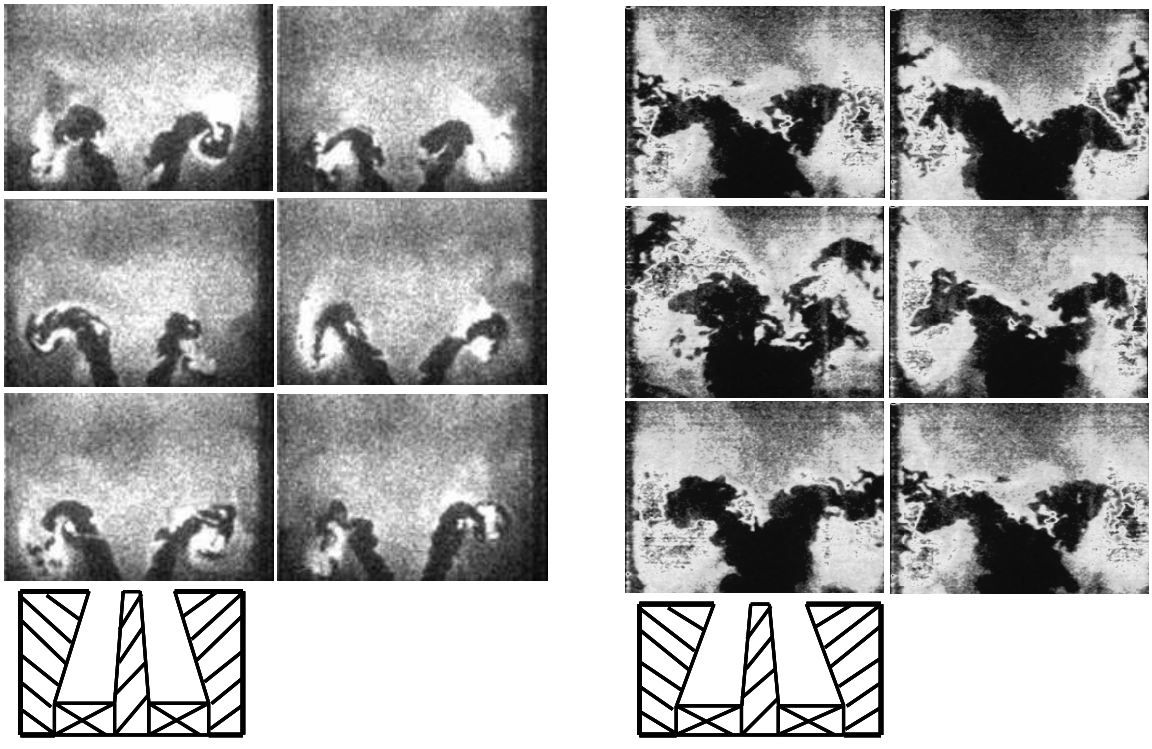

(a) **(b)**

Figure 43: Rollup of the flame into the ORZ at (a) *Re* = 21,000 (flame attached to the center body) and (b) *Re* = 44,000 (flame attached to the outer annulus).

Even in cases where the ORZ does not cause flame-rollup, its size is apparently

modulated through the cycle. This is evident in many images at high flow velocities that show a fluctuating angle of the outer rim stabilized flame, which is riding along the shear layer between the annular jet and ORZ – (shown in Figure 66 of Chapter 4).

iii. Shear Layer Dynamics

The shear layers between the annular jet and IRZ, and the IRZ and ORZ are unstable and subject to rollup, due to the Kelvin-Helmholtz instability. From non-reacting flow studies, this rollup phenomenon is known to exhibit spatio-temporal organization when periodically forced [45].

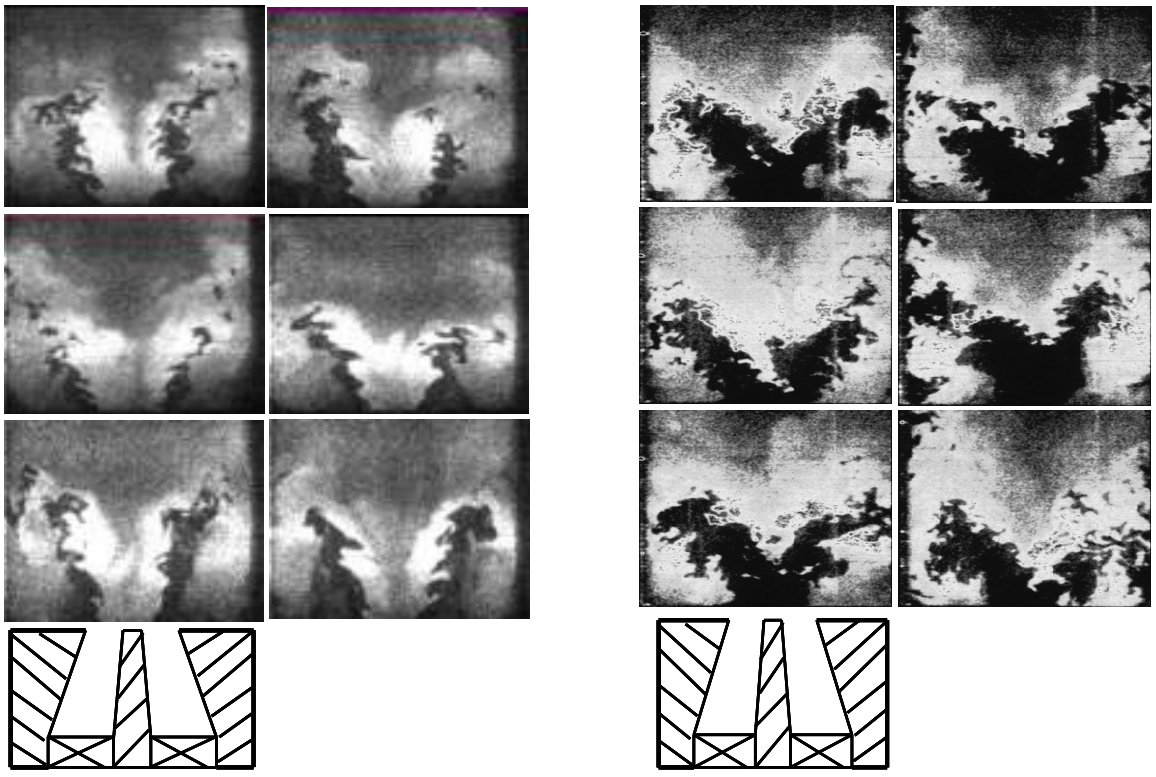

(a) **(b)**

Figure 44: Shear layer instabilities manifested in the flame at (a) *Re* = 21,000 (flame attached to the center body) and (b) *Re* = 44,000 (flame attached to the outer annulus).

As shown in Figure 37 (a) and Figure 44, this rollup phenomenon can occur in the

shear layers between the annular jet and IRZ, the annular jet and ORZ, or both. Images of these vortical structures in the shear layer can also be seen in the computations of Yang [39] and Najm & Ghoneim [46], who also present analyses of their temporal characteristics.

Global Consumption Speed variations

A prior qualitative observation made by Bellows *et al.* [47] was made included the seemingly presence of modulation of "flame wrinkling" through an acoustic cycle. For example, as shown in Figure 3, it can be seen that through the different phases of the acoustic cycle, the degree of flame wrinkling seemed to modulate indicating that the turbulent flame speed was being modulated. In order to quantify this observation, the global consumption speed was estimated using a fractal approach of the flame edges from the OH PLIF images. The caliper method was used to evaluate the fractal characteristics of the flame. A sample result is shown in Figure 45 which shows the Richardson plots at the various phases and excitation amplitudes of u'/u_0 = 0.45 and 0.9 and at a forcing frequency of 130 Hz. The figure illustrates the variation in the length of the flame, L, (normalized by the combustor diameter, D = 70 mm) as estimated using a scale of varying length ε, at two different forcing amplitudes. For reference, the pixel scale corresponds to Ln (ε/D) = -5.45. For small length scales, the flame length tends towards an asymptotic value, but becomes a function of the measurement scale size for larger length scales. The fractal dimensions determined at each phase were then averaged, yielding an ensemble averaged fractal dimension at each phase of the cycle and the results are plotted in From these plots it may be noted that, first, the flame length oscillates through the cycle, as is obvious from the raw images.

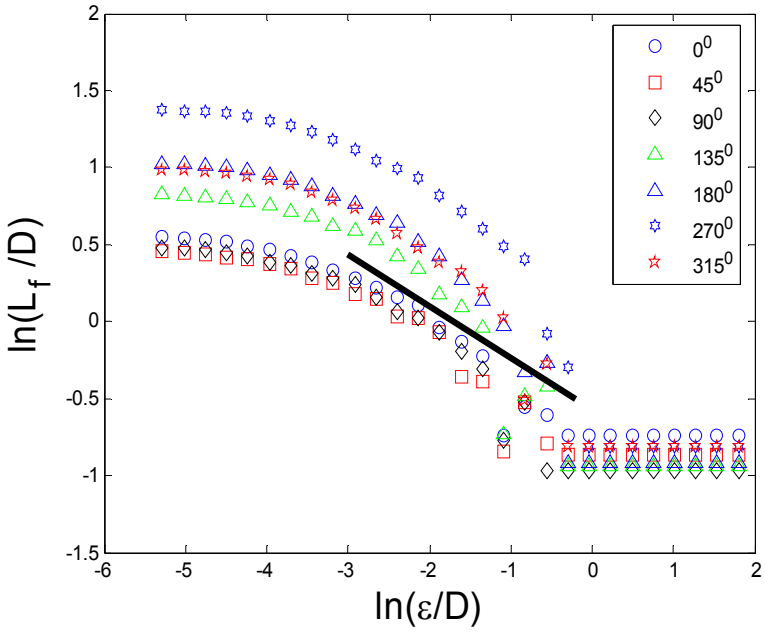

(a)

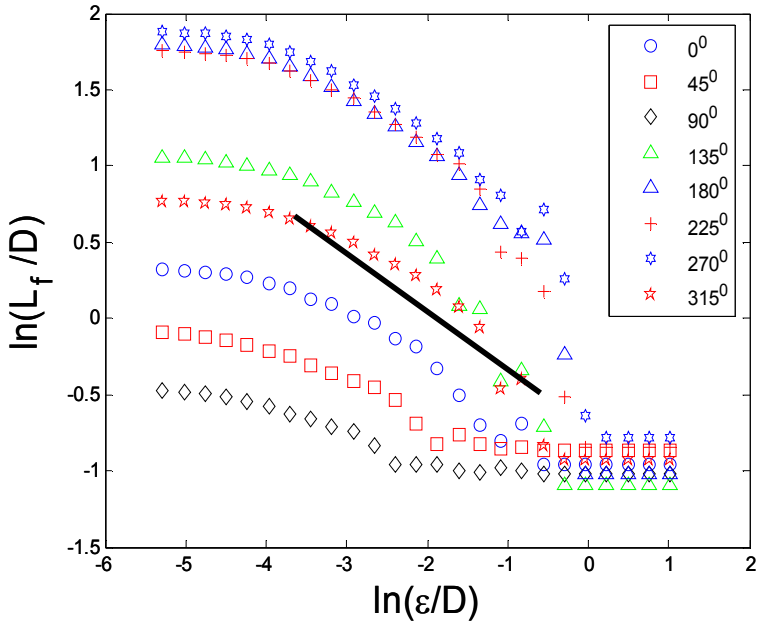

(b)

Figure 45: Richardson plot at the various phases for the forcing frequency of 130 Hz, at (a) u'/u_o =0.45 and (b) u'/u_o =0.9 and at Re=21,000. The black lines on either figure correspond to a fractal dimension of 2.33.

Second, and the point of significance to this discussion, is that the slopes of the curves also oscillate throughout the cycle. Recalling that this slope is related to the flame

fractal dimension, this clearly corroborates our conjecture that the degree of flame wrinkling is modulated. In turn, this implies that the turbulent flame speed (S_T) oscillates throughout the cycle, with a fluctuation level that grows with the velocity forcing amplitude.

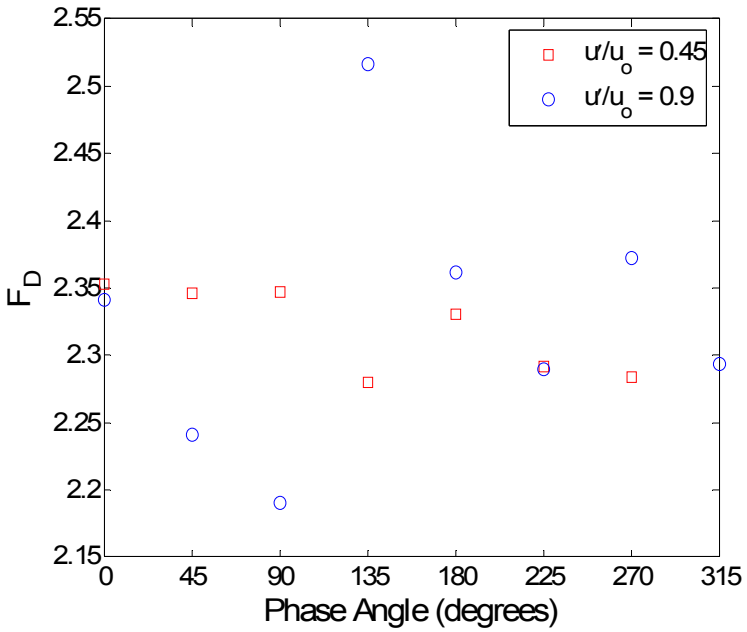

Figure 46: Variation of ensemble averaged fractal dimension (F_D) throughout one cycle of forcing phases at forcing frequency of 130 Hz and Re=21,000.

This latter point can be seen by recalling that the turbulent flame speed, fractal dimension, and inner and outer length scale are related by the expression [32]:

$$\frac{S_T}{S_L} = A\left(\frac{\varepsilon_o}{\varepsilon_i}\right)^{D-2} \tag{3.10}$$

where S_L represents the laminar flame speed, A is a model constant, ε_o and ε_i are the outer and inner cutoff lengths respectively. Given that the slope of the L/D plot varies with scale size, this suggests a flame front with multi-fractal characteristics – i.e., a surface with more complex topology that cannot be characterized by a single fractal

dimension.

Figure 46 plots this fractal dimension fluctuation throughout the cycle. It should be emphasized that this is a somewhat rough approximation since its values depend upon what scale size the slope estimate is evaluated from. The key point of the graph - that the fractal dimension of the flame is oscillating throughout the cycle - is clearly made. The fractal dimension estimated here is a global flame average of a flame whose degree of wrinkling varies strongly with spatial location. That is, the flame is stabilized on the inner center body and thus exhibits minimal wrinkling near the attachment point, and has a flame brush that grows monotonically with downstream distance. As such, it is not clear whether the above described fluctuation in fractal dimension is due to truly local variations in fractal dimension, or simply because of flame length modulation. If this were correct, then we would expect to see a global fluctuation in fractal dimension even if the local fractal dimension of the flame at each downstream location does not change. These two alternatives for the observed global fluctuation in fractal dimension– local fluctuation in fractal dimension or simply fluctuation in flame length – can be checked by analysis of a small spatial region of the flame which is done in the next chapter.

These results demonstrate substantial nonlinearity in the perturbation velocity – heat release relationship, with complex topological dependencies that illustrate folds and kinks when plotted in frequency-amplitude-heat release space. Extensive analysis of the dynamics of the flame length and stabilization point dynamics has been made, suggesting that the dynamics of the vortex breakdown bubble is associated with the non-monotonic transfer function characteristics. A key conclusion from these studies is that analysis of flame dynamics with rudimentary descriptions of the fluid mechanics, as done in many

recent theoretical studies [4], is insufficient for capturing the complex dynamics of these swirling flows (although they are probably sufficient for simpler bluff body or rim stabilized flames). Rather, description of the fluid mechanics, including the dynamics of the IRZ and ORZ is necessary.

Following this point, the fluid mechanics of the flow moves the flame around in complex ways, involving the annular jet, IRZ, and ORZ. However, given the boundary condition of an oscillating mass flow rate into the combustor, the total volume of unreacted fluid in the combustor must oscillate, even as its shape can become quite complex due to these fluid mechanic processes. In other words, given a flame with surface area, S, combustor reactant volume, V, nozzle exit area, A_n, and turbulent flame speed, S_T, it can then be seen that the following relation must hold:

$$\frac{d < V(t) >}{dt} = A_n u(t) - S_T < S(t) > \tag{3.11}$$

This equation says that the time derivative of the reactant volume in the combustor equals the difference between the instantaneous rates of reactant volume flux into the combustor and consumed at the flame. Note also that the heat release fluctuation is due to oscillations in flame surface area, $<S(t)>$, and turbulent flame speed, S_T. Velocity fluctuations in the combustor cause both the volume and surface area to oscillate. However, the shape which the flame takes to satisfy this requirement (that its volume oscillates), varies significantly with the underlying fluid mechanics.

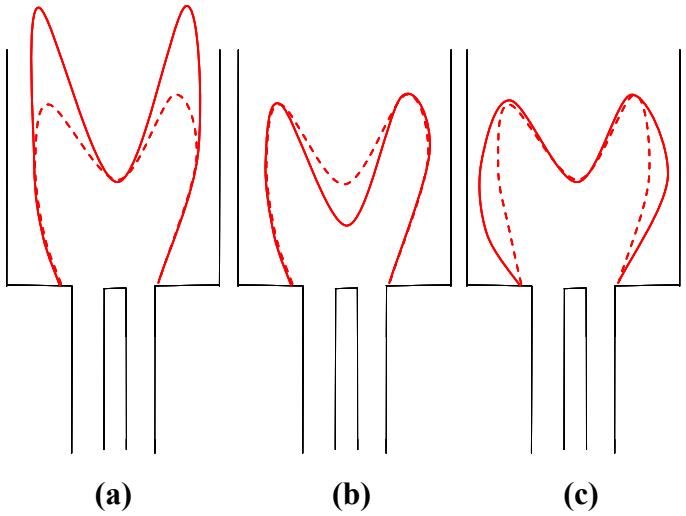

Figure 47: Oscillations in the flame position due to fluctuations in the (a) annular jet (b) IRZ & (c) ORZ.

To illustrate, Figure 47 sketches oscillations in flame position giving approximately the same volume, but due to oscillations in the annular jet, IRZ, and ORZ. It can be seen that *the accompanying change in flame surface area, and therefore heat release, could be quite different*. Furthermore, Figure 47 (b) provides one example where the resulting heat release oscillation due to a velocity fluctuation can exhibit counterintuitive effects. In this example, the flame area decreases, even as the mass flow rate into the combustor increases.

In addition, the case where the volume change is taken up in the annular jet, shown in Figure 47 (a), would presumably allow a much larger downstream growth in flame brush thickness than in the other cases, possibly causing a larger role for the turbulent flame speed fluctuation mechanism described above. In addition, the volume and surface area are coupled, complicating matters. Configurations with higher surface to volume ratios will have larger relative volumetric destruction rates. If this surface/volume ratio varies with forcing amplitude, this can cause saturation – this is analogous to the problem in

turbulent premixed combustion of the turbulent flame speed dependence on turbulence intensity and is at least partially responsible for the "bending" of the S_T curve at higher turbulence intensities. For example, Bellows et al. [12] argued that this was the mechanism for saturation in flame response due to vortex rollup.

In summary, the flame response is not controlled by any single key physical process, but rather several processes occurring simultaneously which are potentially competing, and whose relative significance depends upon forcing frequency, amplitude of excitation, and flame stabilization dynamics. This chapter further identifies and catalogues the key physical processes that control the flame response to acoustic excitation and this is required before rational sense can be made of these results. Only with this understanding can the more global problem of the response of a swirl flame to acoustic excitation be understood. Finally, the impact of turbulent flame speed and brush development on the flame response is presented in the next chapter.

CHAPTER 5

EFFECT OF ACOUSTIC FORCING ON TURBULENT FLAME PROPERTIES

This chapter presents the results on the effect of acoustic forcing on turbulent flame properties and in particular the flame brush thickness and the turbulent flame speed. While the previous chapter catalogued the different mechanisms that lead to a nonlinear flame response when subject to acoustic excitation and identified the modulation of the turbulent flame speed as one possible mechanism, the current chapter examines this mechanism in detail. More specifically, this chapter elucidates the effect of acoustic forcing on the temporal and spatial variations of the turbulent flame brush and the local consumption speed. The experiments were conducted in two different acoustically excited flame configurations: a lean premixed swirl and a lean premixed turbulent Bunsen flame. The diagnostic techniques that were used to characterize the turbulent flame properties included phase locked OH PLIF for the swirl flame and phase locked PIV for the Bunsen flame. Results are first presented for the Bunsen flame followed by those of the swirling flame.

Bunsen Flame

The results reported in this subsection were obtained at a Reynolds number of 10,200 (based on the burner exit diameter and mean flow velocity of u_o ~10m/s). In the unforced case, the centerline turbulent fluctuations were of the order of u'_t/u_o = 0.05. Forced excitation cases were obtained at an excitation frequency (f_{drive}) range of 100 – 400 Hz and at the excitation amplitude of u'_d/u_o = 0.01 – 0.15.

Figure 48 overlays a number of instantaneous images of the flame edge, showing the development of the flame brush for the unforced case. The clear growth of the flame brush can be seen with increasing distance in the downstream direction from the flame holder, an observation consistent with prior studies in the literature [22].

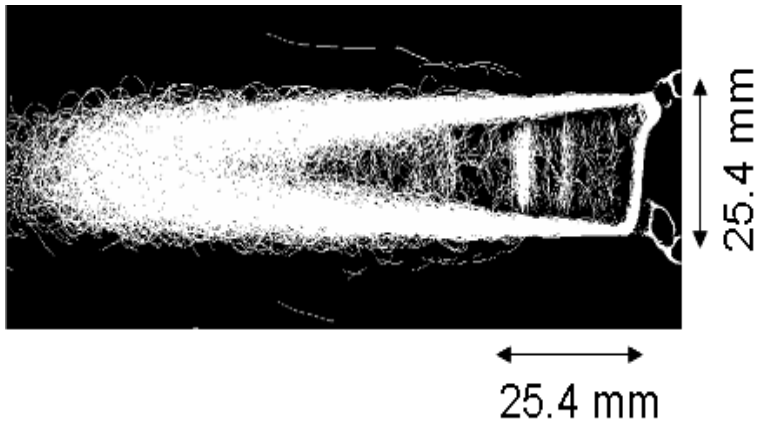

Figure 48: Overlay of several extracted flame edges showing flame brush development for the unforced case.

The instantaneous flame edges obtained from the Mie-scattering images were used to visualize the flame brush. Figure 49 shows two sample mean progress variable images for the unforced and acoustically excited turbulent Bunsen flames that were obtained by ensemble averaging the binarized instantaneous flame images (i.e. after splitting the images into reactants and products). Figure 50 overlays a number of instantaneous phase locked flame edges for 8 phases of an acoustic cycle. On careful observation of these images, one can see that the flame brush thickness (δ_t) can be seen to exhibit a step-like behavior, i.e. growing very slowly for a certain distance before increasing rapidly across the rollup region, and then increasing slowly again.

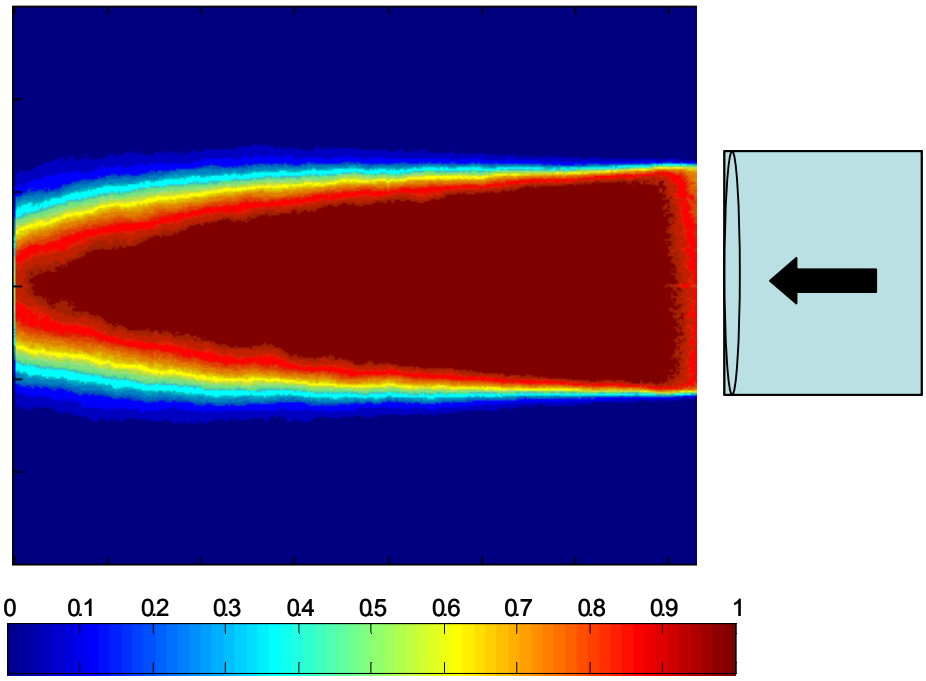

(a)

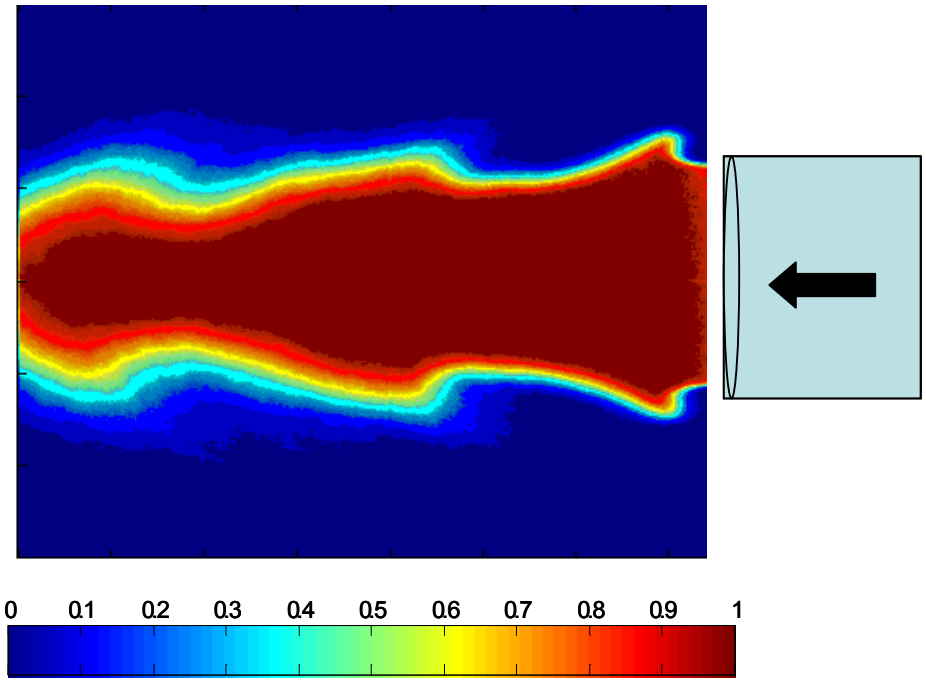

(b)

Figure 49: Progress variable contours for (a) unforced and (b) acoustically excited (f_{drive} = 400 Hz and u'_{α}/u_o = 0.2) turbulent Bunsen flames.

For example, in Figure 50 at the phase of 0^o and 315^o, it can be observed that close to the base of the burner, the flame brush thickness increases rapidly at the location of the first rollup. Downstream of this rollup region, δ_t increases quite slowly before increasing again at the location of the next rollup. The evolution of the flame brush at the other phases is also shown in Figure 50, in which the progress variable contours indicating the edges of the flame brush are shown.

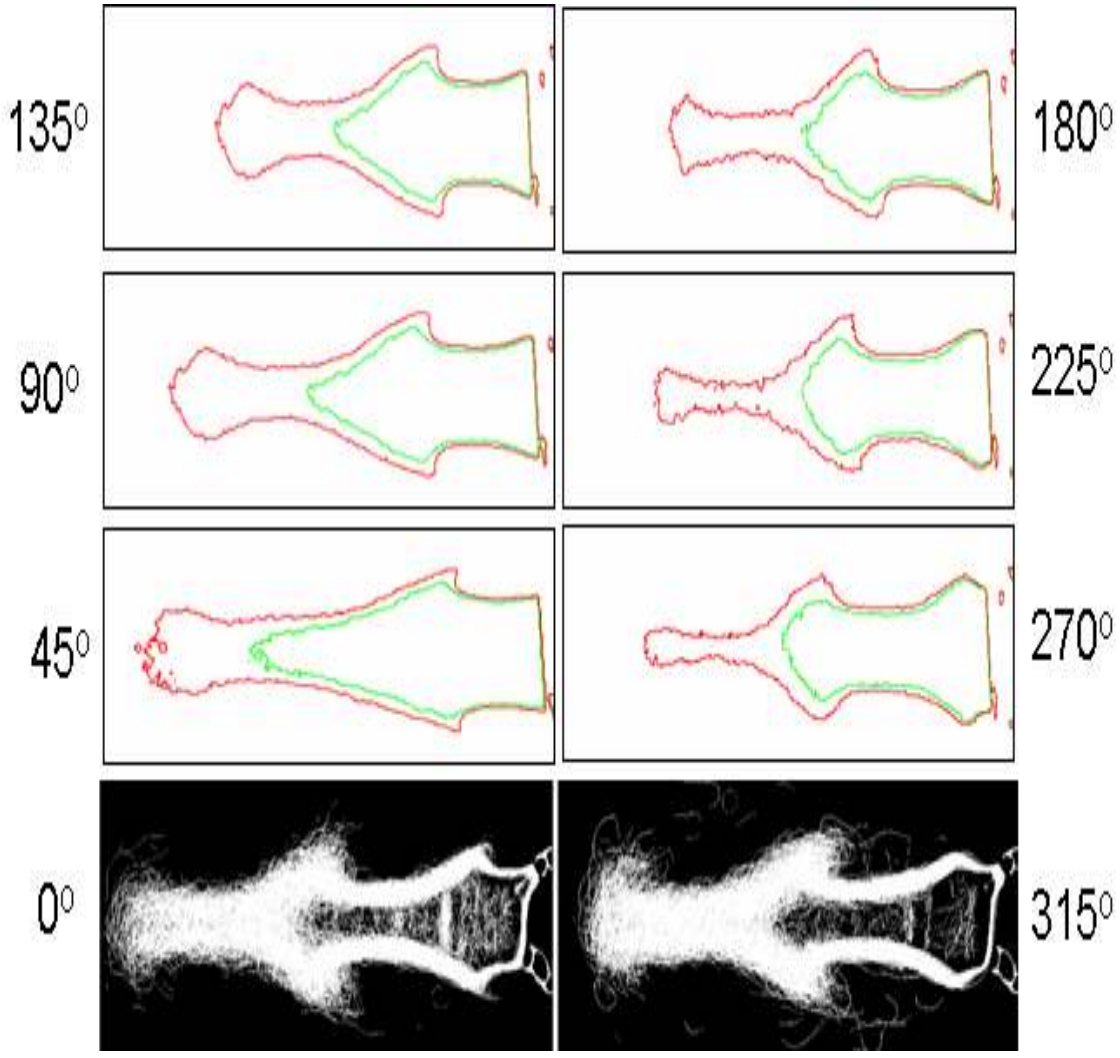

Figure 50: Sample ensemble averaged images and progress variable contours of $\overline{c}$ =0.3 (green line) and $\overline{c}$ =0.7(red line) illustrating the development of the flame brush at *Re* = 10,200, f_o = 200 Hz and u'/u_o = 0.15.

These results illustrate that δ_t grows very slowly up to the location of the convecting vortex, after which it rises rapidly and then grows slowly again. This behavior is significantly different from the unforced case, where the flame brush thickness increases rapidly along the flame coordinate. The above behavior of the spatial evolution of δ_t at a given excitation frequency (f_{drive} = 300 Hz) and flow velocity (Re = 10,200) is quantified in Figure 51. It can be seen that δ_t increases monotonically in the downstream direction for the unforced case, as discussed earlier.

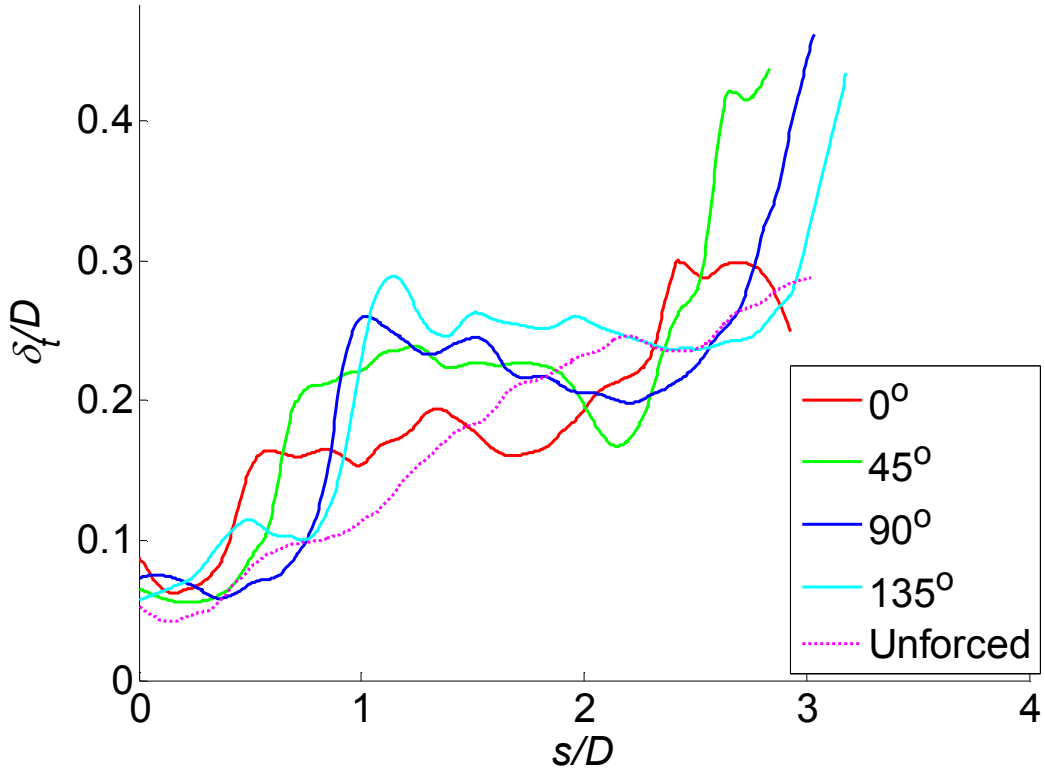

Figure 51: Spatial variation of the normalized flame brush thickness (δ_t /D) along the normalized flame coordinate (s/D).

However, in the presence of acoustic oscillations, δ_t exhibits the step like behavior explained above. For example, consider the variation of the δ_t at the phase of 45° in Figure 51. The flame brush is initially a constant before rising rapidly at the flame

coordinate *s/D* = 0.75 (the location of the vortex). After rising rapidly, δ_t remains nearly constant. Similar behavior can also be seen at 135^o, in which, the flame brush thickness jumps at the flame coordinate *s/D* ~ 1.1 and then again at *s/D* ~ 2.5 (the next location of the vortex) and growing very slowly in the regions between the vortices.

Now, it should be noted that the overall or global trends in the growth of the flame brush thickness seems to be similar in both the cases of the unforced and forced cases. For example, from Figure 51 if one were to measure the growth rate of the flame brush thickness from say *s/D* = 0 .5 to 2, it seems to be very similar for the cases of with and without acoustic excitation.

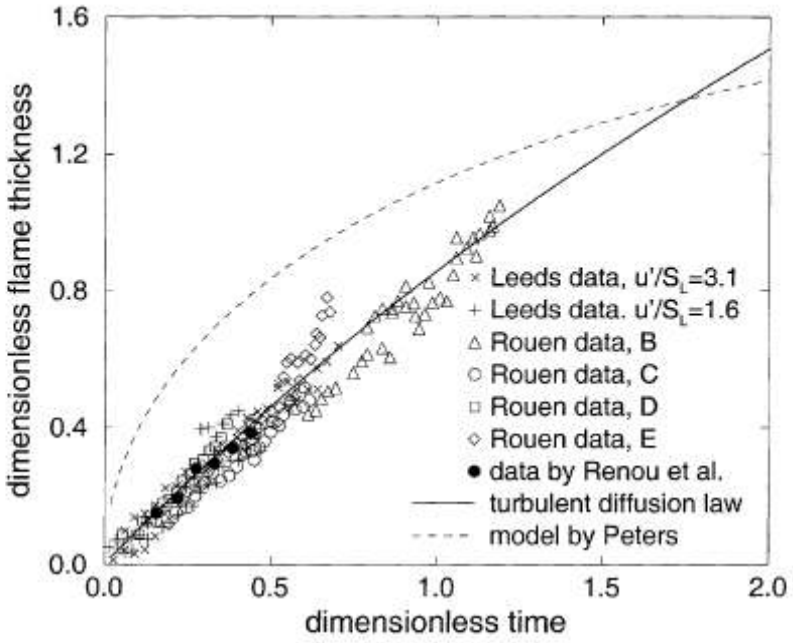

Figure 52: Dimensionless mean flame brush thickness δ_t/ L vs t/τ (dimensionless time). Crosses and pluses show Leeds experimental data (spherical flames- [48]) at different turbulence levels. Open symbols show the Rouen experimental data [49] obtained for open V-shaped, lean hydrogen-air flames stabilized on a rod with different turbulence characteristics reported in four different cases (B-E). Filled circles show the data measured in freely expanding spherical stoichiometric methane-air flames by Renou et al. [50].Dashed and solid lines are calculated by Peters [51] and Equation (2.10).

This observed trend that the flame brush thickness grows at a very minimal rate in the regions between the two vortices seems to be counter-intuitive since δ_t is always expected to grow with downstream distance because of turbulent diffusion. Numerous physical models [51,52,53] and experiments [54,55,56,57,58] have shown that the flame brush thickness grows with downstream distance. For example, Lipatnikov and Chomiak [22] in their review paper describe a universal trend that has been observed for most stationary developing flames.

$$\delta_t^2 = 2u'L_L t\left\{1-\frac{\tau_L}{t}\left[1-\exp\left(-\frac{t}{\tau_L}\right)\right]\right\} \tag{5.1}$$

$$\delta_t = \begin{cases} u't & if \quad t << \tau_L \\ \sqrt{2u'L_L t} & if \quad t >> \tau_L \end{cases} \tag{5.2}$$

Their result is reproduced in Figure 52 [22] which plots the normalized flame brush thickness as a function of flame development time (or distance) from various experiments. Figure 52 includes results from various fuel mixtures (natural gas, propane, hydrogen), burner types and turbulence intensities and shows that for various premixed flame configurations as well as for different fuels, the flame brush thickness grows monotonically with downstream distance. Equations (5.1) and (5.2) describe the turbulent diffusion model for the flame brush thickness and it can be seen that for small time scales, the flame brush thickness follows a linear variation with development time (or distance) and for large time scales the flame brush thickness exhibits a square root variation. This continuous growth of the flame brush thickness is attributed to turbulent diffusion. In addition, Lipatnikov and Chomiak suggested that since δ_t is governed by turbulent diffusion, a time scale that is much larger than the residence times in typical

laboratory or industrial burners is required to achieve a fully developed flame front (characterized by a fully developed δ_t). However, the results obtained in the current study show that the flame brush does not grow continuously and that in the regions in between the vortices, the flame brush thickness grows at a very slow rate. The next few sections address the physics behind this observed behavior.

Effect of excitation amplitude on the flame brush growth

In order to better understand the trends observed in Figure 51, an amplitude sweep was conducted at a given phase and frequency to determine the spatial variations of the flame brush thickness. Sample results are shown in Figure 53 which were recorded at a fixed frequency of excitation and flow velocity and compares the growth in the flame brush thickness with downstream distance of the unforced and acoustically excited cases.

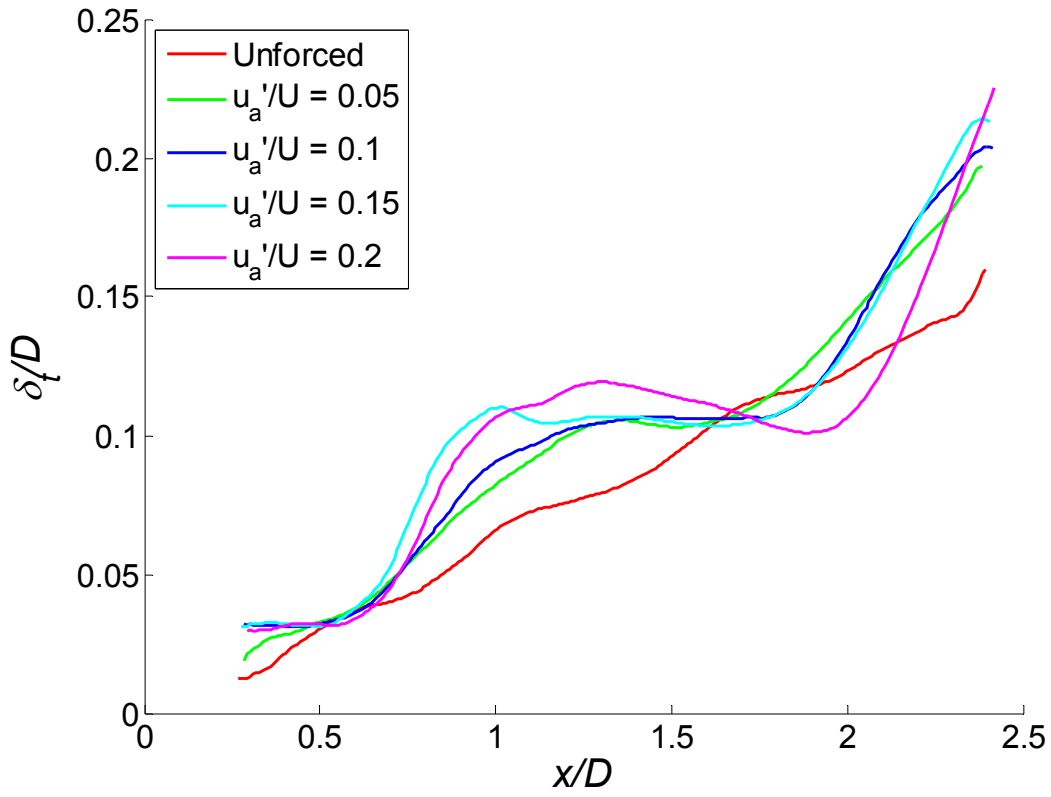

Figure 53: Variation of the normalized flame brush thickness (δ_t /D) along the normalized flame coordinate (s/D).

Figure 53 shows that in the presence of acoustics, the trends observed in the growth of the flame brush thickness differ markedly from the unforced case. For example, from Figure 53, one can observe that at all the different acoustic amplitudes of excitation; the flame brush thickness grows in a step like fashion in the regions between the vortices. It may be further observed that at higher amplitudes of excitation (example u'_a/u_o = 0.2), the flame brush thickness actually decreases slightly before increasing again - a more detailed description of this behavior is provided in the sections of "Phase Jitter". Figure 53 also reveals that step like behavior of the flame brush thickness gradually grows with acoustic amplitude and does not occur at any set threshold amplitude.

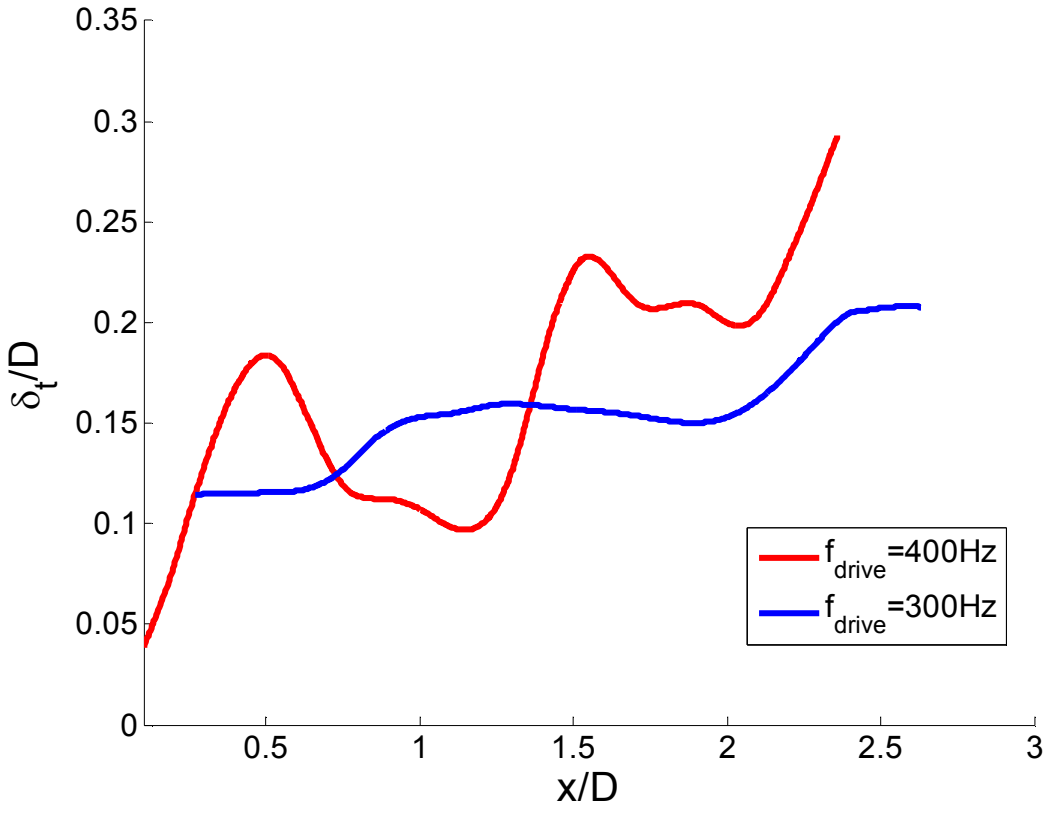

Figure 54: Spatial variation of flame brush thickness (δ_t /D) at different excitation frequencies and at u'_a/u_o=0.09

Effect of frequency

The effect of frequency on the flame brush growth was studied at the frequencies ranging from 200 – 400 Hz and the results are presented in Figure 54. From Figure 54 it can be observed that for the given frequencies the step like behavior can be readily observed. This seems to indicate that the step like behavior in the flame brush thickness indicating once again that there might not be a certain frequency at which this behavior is triggered. It should be noted that experiments were not conducted at higher frequencies since at high frequencies the vortices shed are close to each other spatially and in order to avoid vortex – vortex interactions.

Velocity Field Measurements

In order to gain a physical insight into the behavior of the flame brush thickness, high resolution phase locked PIV measurements were conducted on the acoustically excited Bunsen flame focusing on a small region of the turbulent Bunsen flame close to the burner exit. A sample ensemble averaged velocity field at the excitation frequency of 300 Hz and at a particular phase is shown in Figure 55 (a). The flow direction is indicated by the black block arrow located on the upper left of the figure. It should be noted that in this figure, the velocity field at the shear layer is biased by the presence of the flame. As a result of the acoustic excitation, the mean velocity variation along the axial direction can be observed in this figure. The corresponding two dimensional r.m.s. velocity field is shown in Figure 55 (b) and the key take away from this figure once again is that even along the centerline, the turbulence intensity seems to oscillate along the axial direction at a fixed radial location.

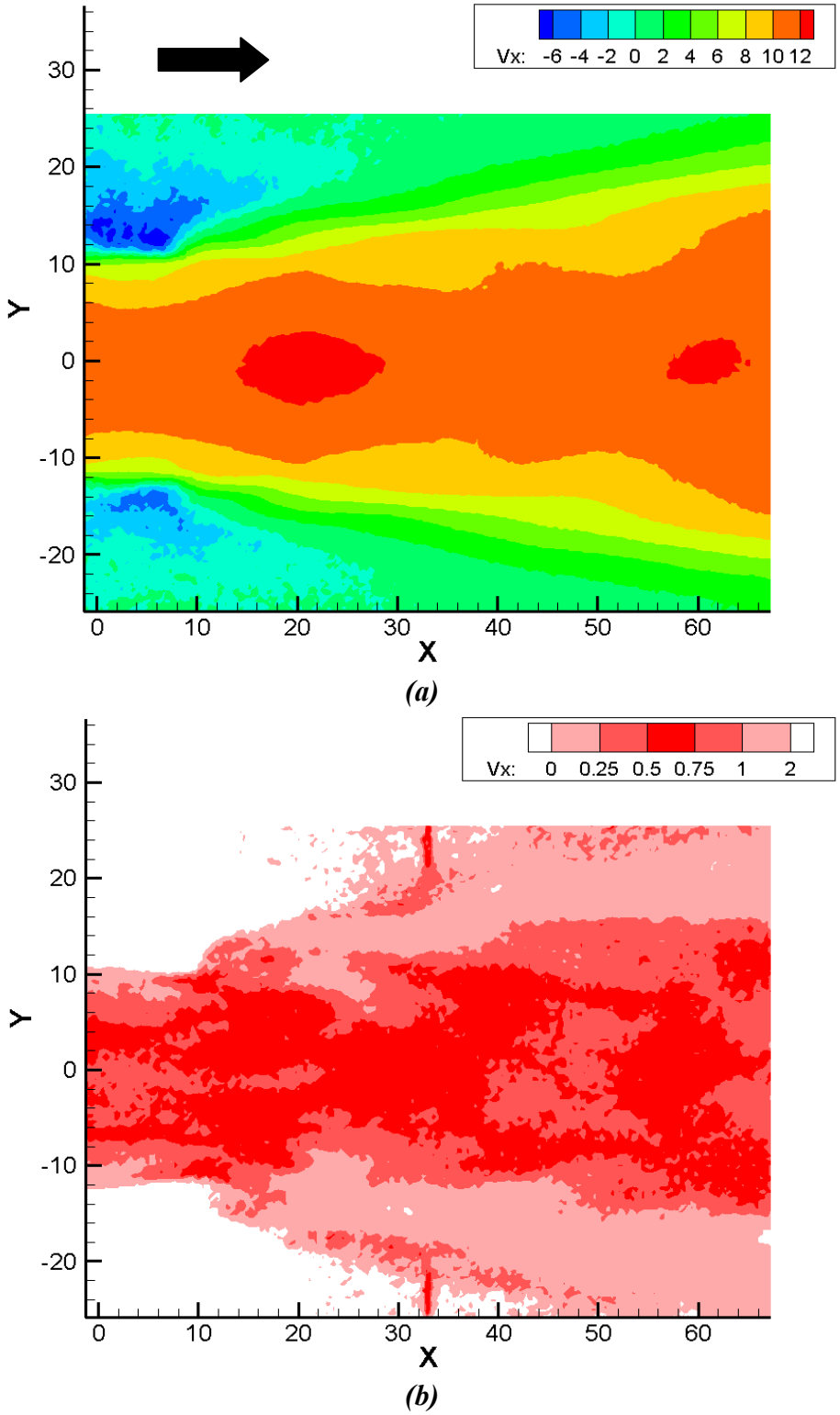

Figure 55: Sample velocity field in an acoustically excited Bunsen flame showing (a) axial velocity field and (b) r.m.s. of the axial velocities (u'_t) at f_{drive} = 300 Hz and u'_a/u_o=0.09.

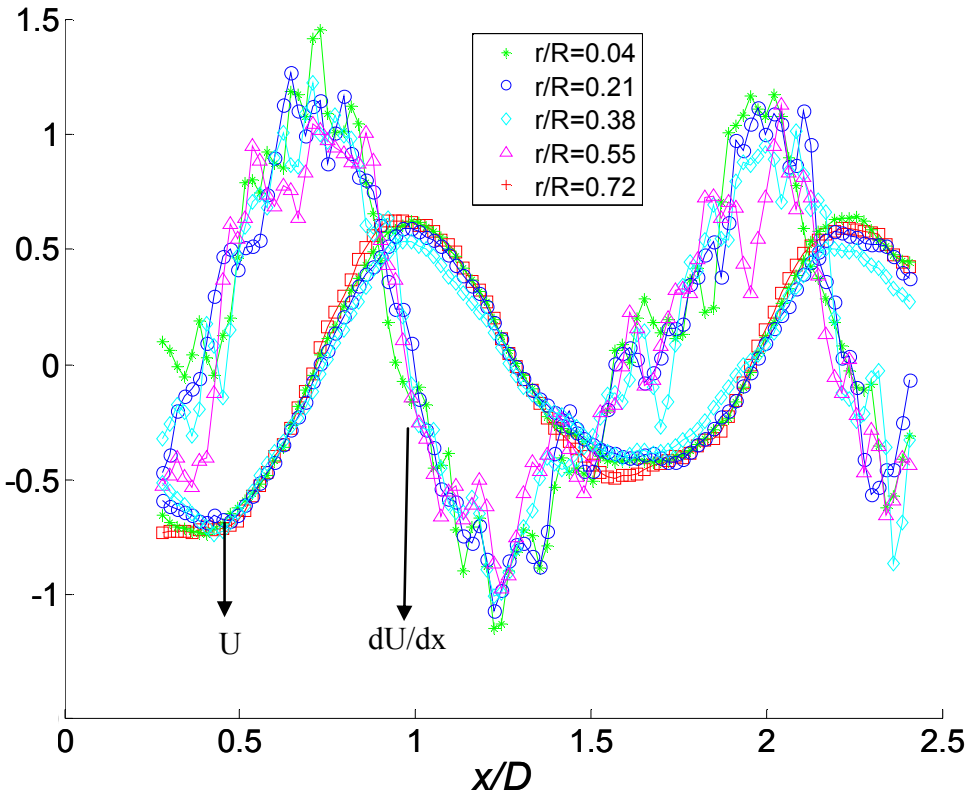

Figure 56: Sample ensemble averaged variations of the acoustic velocity and the corresponding axial velocity gradients f_{drive} = 300 Hz and u'_a/u_o =0.09.

While the contour plots of Figure 55 give us a global idea of the flow field, let us take a closer look at the spatial variation in the velocity profiles and at different radial locations. A sample velocity field of the acoustically forced Bunsen flame is shown in Figure 56 which plots the ensemble averaged spatial variations of the axial velocity and the corresponding axial velocity gradients along the axial location. From this figure, the clear phase offset of $\pi/2$ between the axial velocity and its gradient can be seen. In addition, the changes in the axial velocity and its gradient with radial distance are very minimal. Since there exists very little variation in velocities and the velocity gradients in the radial distance until the flame location ($r/R \sim 0.9$) the velocities (and strain rates) at the flame

location may be assumed to be of the same order as those at the start of the flame brush. This is an important result as it indicates that the strain rates that might influence the flame are similar in magnitude as those at the beginning of the flame brush. This is due to the fact that the strain rate caused by the acoustics is of a higher magnitude than that of the expanding flow and hence it is assumed that the strain rate at the location of the flame front is dominated by the acoustic strain rate.

Next, a comparison of the spatial variation of the flame brush thickness variations with the velocity field is shown in Figure 57. This figure plots the spatial variation of the flame brush thickness, the axial velocity, the strain rate and the gradients in the flame brush thickness along with the turbulence intensity in the same figure. It should be noted that for the velocities presented, the unforced velocity field is subtracted to capture the effect of acoustic forcing. The results are presented at the same phase, frequency and flow velocity but at four different excitation amplitudes. From Figure 57, it can be observed that the axial velocity and the strain rate are varying in a sinusoidal manner with downstream distance – a result of the acoustic excitation. In addition, the turbulence intensity in all the four amplitudes seems to be in phase with the acoustic velocity and seems to be varying in a sinusoidal manner. This is an important result as it shows that despite the mean velocity (and hence *Re*) remaining a constant, the turbulence intensity at each phase of the acoustic cycle is affected by the coherent acoustic velocity. Thus the incoherent velocity/turbulent fluctuations are modulated by the presence of a coherent acoustic field.

The axial variation of the flame brush thickness is also included in Figure 57 and a number of interesting observations can be made from this figure. Firstly, it can be sent

that the flame brush thickness grows rapidly in the regions of positive axial gradients, while it grows very slowly in the regions of negative axial gradients and decreases in some cases of the higher amplitudes of forcing (see Figure 57 (d)). For example, in Figure 57 (c), in the regions of *x/D* from 1-1.5, the strain rate is negative in sign and the growth of the flame brush thickness is suppressed in this region. This result is counter-intuitive since in accordance with the diffusion model described above, it is expected that the flame brush thickness always grow in the regions of negative strain rates.

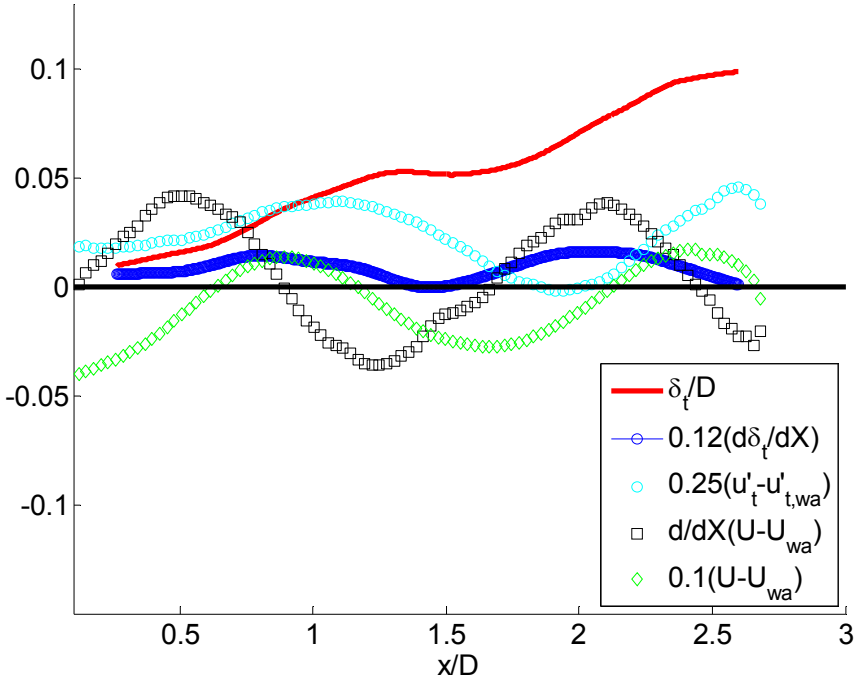

(a)

Figure 57: Sample variations of the flame brush thickness, the gradient in the flame brush thickness, the turbulence intensity along the flame front, the axial gradient in the velocity field and the axial velocity at *Re*= 10,000 Hz, f_{drive} = 300 Hz, (a) u'_a/u_o = 0.05, (b) u'_a/u_o =0.07, (c) u'_a/u_o =0.09 & (d) u'_a/u_o =0.11.

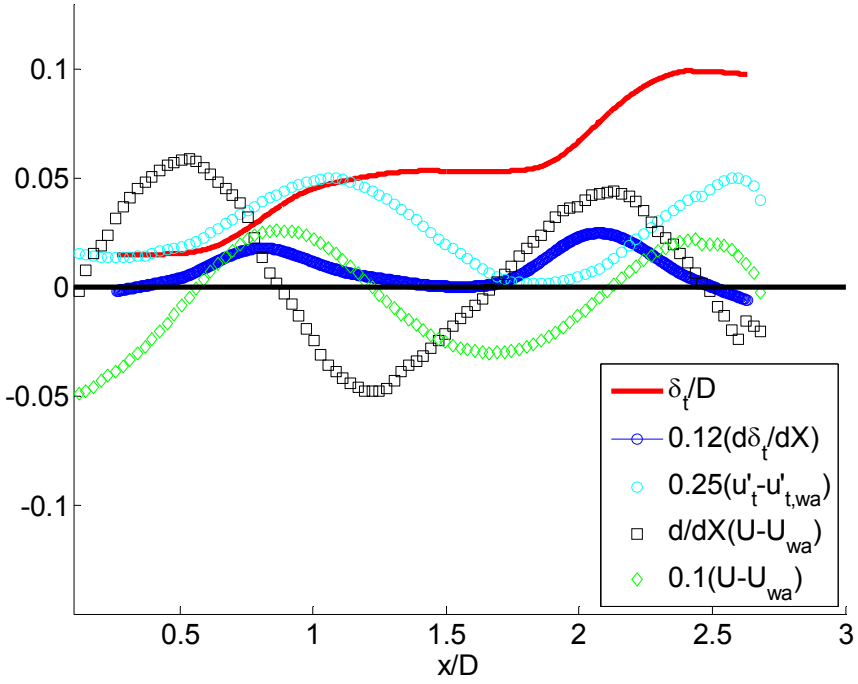

(b)

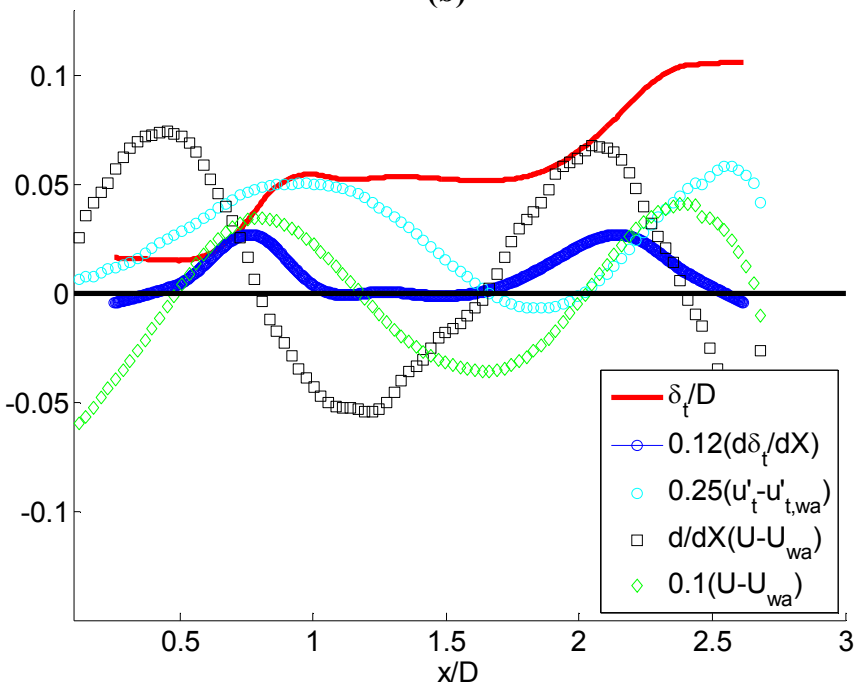

(c)

Figure 57 (continued)

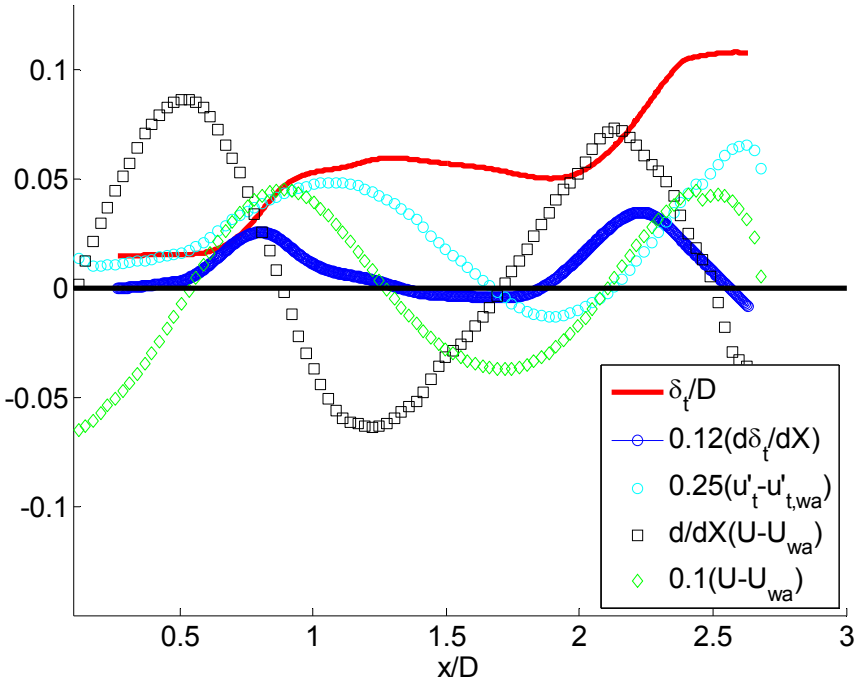

(d)

Figure 57 (continued)

Acoustically forced non-reacting shear layers

The above observation of the growth the flame brush thickness is analogous to the step like growth behavior observed in an acoustically forced non-reacting shear layer. Wiesbrot and Wygnanski [59] in their study of acoustically forced turbulent jets, observed that the shear layer grew in a step like manner. Figure 58 reproduces one such representative result from their experimental study which shows the spatial growth of the shear layer. From this figure, it can be seen that the shear layer grows initially in a linear manner. However, this linear rise is followed by a region of decreasing growth in the shear layer before beginning to rise again. The authors detailed that this decreasing region of the shear layer was a result of negative turbulent Reynolds stress production and that the turbulent energy was being fed into the coherent structures. This interaction between the incoherent fluctuations (turbulence) and the coherent fluctuations seem to be a

possible explanation for the oscillation in the spatial variation of the turbulent intensity in the current study (see Figure 57).

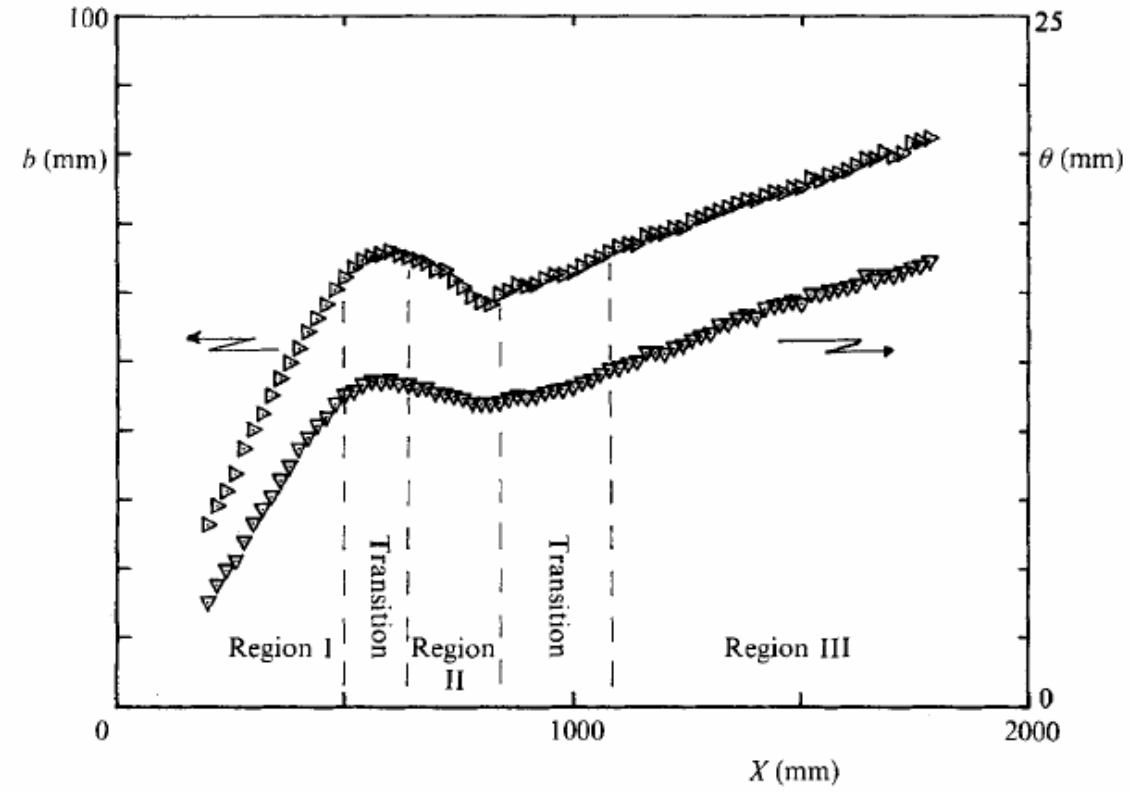

Figure 58: Growth of the shear layer in an acoustically forced nor-reacting jet (reproduced from Wiesbrot and Wygnanski [59]).

The flame brush thickness may be fundamentally thought of being affected by two main parameters: (1) flame wrinkling and (2) flame movement/flapping. An increase in flame wrinkling would lead to a higher brush thickness while an increase in the flame movement/flapping would also lead to the same effect. Now, the flame wrinkling could increase as a result of an increase in the local turbulent flame speed which could have increased as a result of an increase in the turbulent intensity. Next, an increase in the flame flapping could be because of either an increase in the kinematic restoration caused by a stretch effect or because of phase jitter - caused by random variations in the location

of the shed vortex which in turn could affect the flame brush thickness. Let us examine each of these mechanisms in detail.

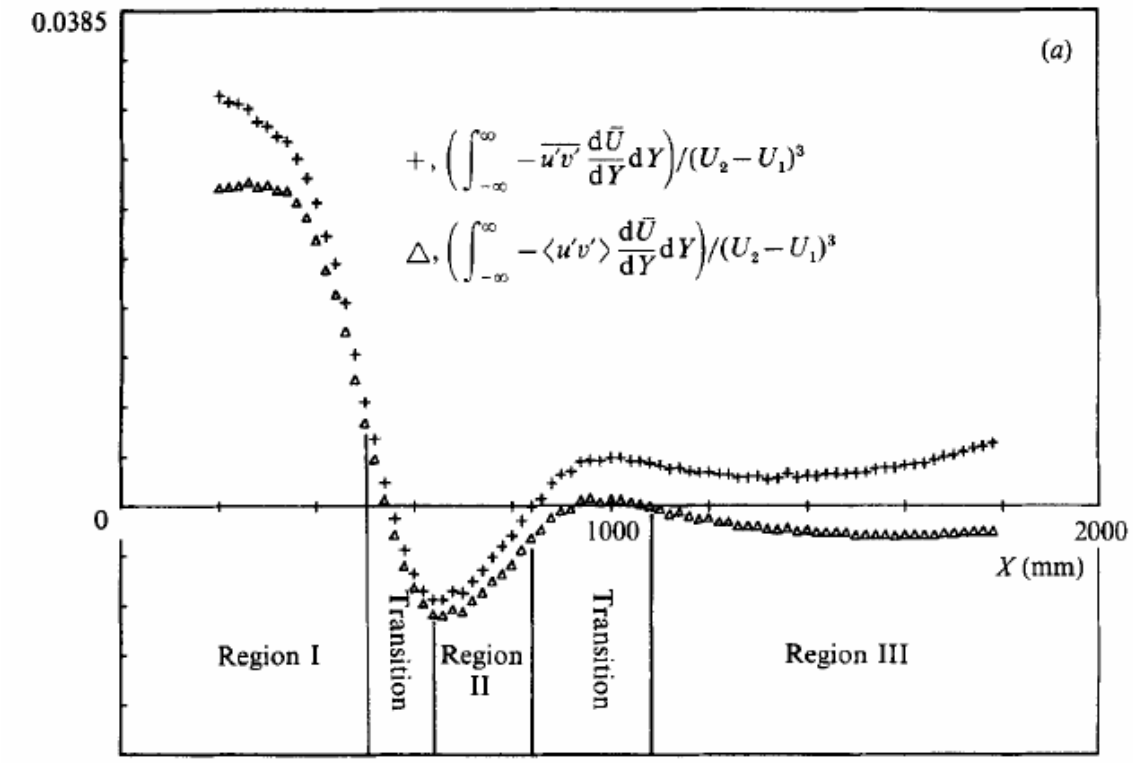

Figure 59: Spatial variation of the turbulent Reynolds stress of an acoustically forced jet (reproduced from Wiesbrot and Wygnanski [59]).

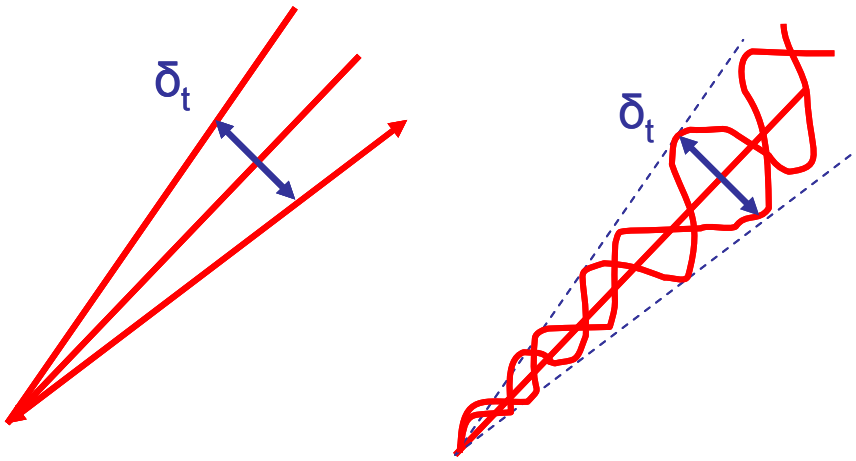

Figure 60: Illustration showing the growth of the flame brush thickness due to (a) flamefront flapping and (b) flame front wrinkling

Stretch Effects

Now, from Figure 57, it was observed that the growth of the flame brush was suppressed in regions of negative strain rates. However, as explained before, the flame brush thickness is expected to grow in regions of negative strain rate and the observed trends are an exact contradiction to what is expected. To test whether this is a stretch related effect, similar experiments are conducted on lean propane-air mixtures which has a Markstein length of opposite sign to that of lean methane-air.

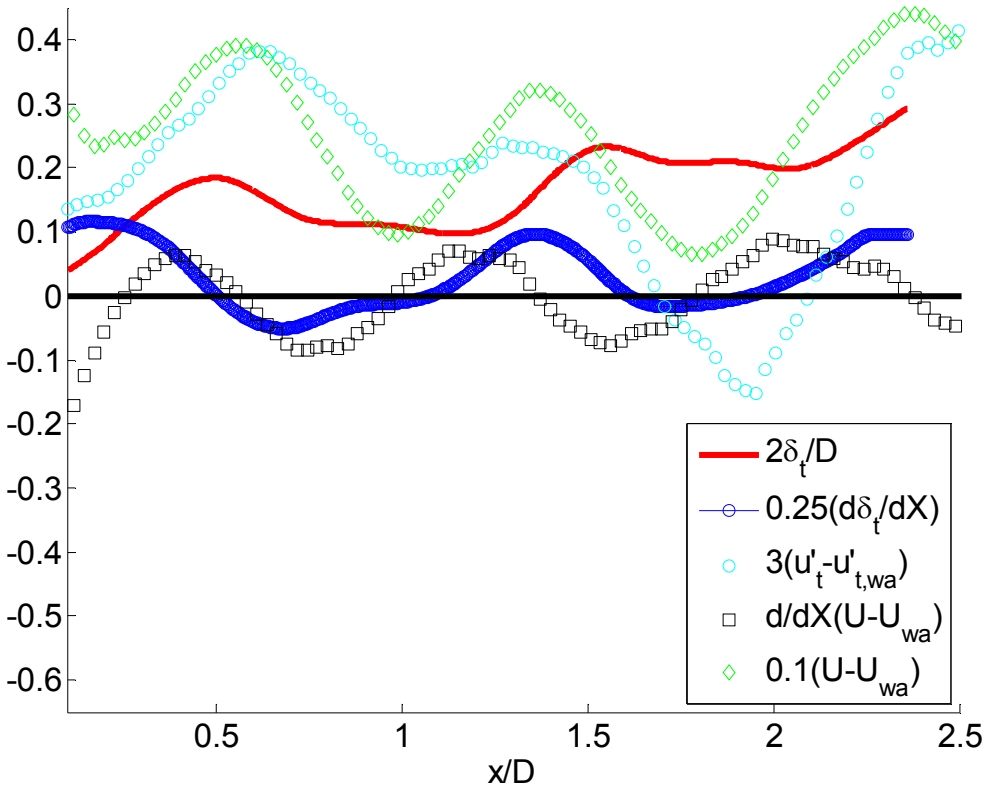

Figure 61: Variation of flame brush thickness, acoustic velocity and their gradients along axial distance for lean propane u'_d/u_o = 0.2, f_{drive} = 400 Hz.

So if strain rates were to be the dominant factor in controlling the growth of the flame brush thickness, then one would expect opposite trends to that of lean methane. The same experiment is conducted on lean propane-air and the results are shown in Figure 61 which plots the variation of the flame brush thickness, axial velocity, turbulence intensity and the gradients in the flame brush thickness and velocity with axial distance for the case of lean propane. From Figure 61, it can be seen that once again in the regions of negative strain rates, the growth of the flame brush is suppressed. For example, in the regions of *x/D* from 0.5 to 1, the strain rate is of negative sign and the flame brush thickness also does not grow. Hence, the results show that the trends of the flame brush growth are similar to those of lean methane-air mixtures. This seems to suggest that strain rates and

hence stretch effects might not be the dominating factor in curbing the growth of the flame brush thickness.

Local Consumption Speeds: Bunsen flame variations

The variation of the local consumption speed for the Bunsen flames also has important implications in the variation of the flame brush thickness of the acoustically forced turbulent Bunsen flames. Since the consumption speed represents the degree of wrinkling of the flame, and the degree of wrinkling can be associated with the turbulent flame brush, the local consumption speed and the turbulent flame brush can be connected. More specifically, higher the degree of wrinkling, the flame brush thickness if also expected to be higher. To determine whether the growth of the flame brush thickness can be explained by any changes in the degree of wrinkling of the flame front, the local consumption speed $S_{T,LC}$ was computed. $S_{T,LC}$ is a measure of the degree of flame wrinkling and higher the flame wrinkling, higher would be $S_{T,LC}$ leading to a higher flame brush thickness. In the computations of $S_{T,LC}$ the $\overline{c}$ = 0.5 contour was assumed to be the reference surface to account for changes in mean flame shape at each phase of the acoustic cycle. Normals were drawn from the $\overline{c}$ = 0.5 to the instantaneous flame edge and the flame area was computed within each "tube" – an ensemble average then yielded the ensemble averaged flame surface area A_T. The ratio of A_T to the tube size $A_{L,ref}$ at every spatial location yields $S_{T,LC} / S_{L,ref}$.

Spatial variations of $S_{T,LC}/S_L$ in the presence of acoustics

Figure 62 shows a sample variation of $S_{T,LC} / S_{L,ref}$ with downstream distance at a fixed excitation frequency (f_{drive} = 300 Hz) and phase of an acoustically excited Bunsen

flame. Results are presented for two amplitudes are presented in this figure and in each of these cases, it can be seen that the trends in the spatial variation of $S_{T,LC} / S_{L,ref}$ and the flame brush thickness δ_t are very similar. For example, in Figure 62 (b), δ_t is seen to increase at an x/D of about 0.5 and then stops growing at x/D= 1.1. On comparing this with $S_{T,LC} / S_{L,ref}$, it can be seen that $S_{T,LC} / S_{L,ref}$ also grows at x/D ~ 0.5 and then stops growing/ begins to decrease at x/D ~ 0.8. $S_{T,LC} / S_{L,ref}$ then grows at a very slow rate until x/D ~ 1.7 before rising rapidly once again. Overall, the trends of δ_t and $S_{T,LC} / S_{L,ref}$ seem to be in phase and they seem to be rising/decreasing at the same locations. Since, the local consumption speed is affected mainly by fine scale wrinkling and hence by the turbulence intensities, the above result corroborates the result that he turbulence intensity is affected by acoustic excitation.

Next, on comparing this trends of δ_t and $S_{T,LC} / S_{L,ref}$ with the turbulence intensity u_t', it can be observed that of δ_t and $S_{T,LC} / S_{L,ref}$ increase in regions of increasing u_t' while in the regions of decreasing u_t', δ_t and $S_{T,LC} / S_{L,ref}$ grow at a very slow rate. Now, both δ_t and $S_{T,LC} / S_{L,ref}$ are influenced by the local u_t' as well as by the turbulent diffusion.

Thus the growth rate of these turbulent properties is governed by turbulent diffusion and by the turbulence component that is influenced by the acoustics and at any given location, the magnitude of δ_t and $S_{T,LC} / S_{L,ref}$ is a net superposition of the diffusion component and that influenced by the acoustics. While the diffusion causes the magnitude of δ_t and $S_{T,LC} / S_{L,ref}$ increase with axial distance, the harmonic variation of the turbulence intensity (u'_t-$u'_{t,wa}$) causes $S_{T,LC} / S_{L,ref}$ to decrease and increase rapidly.

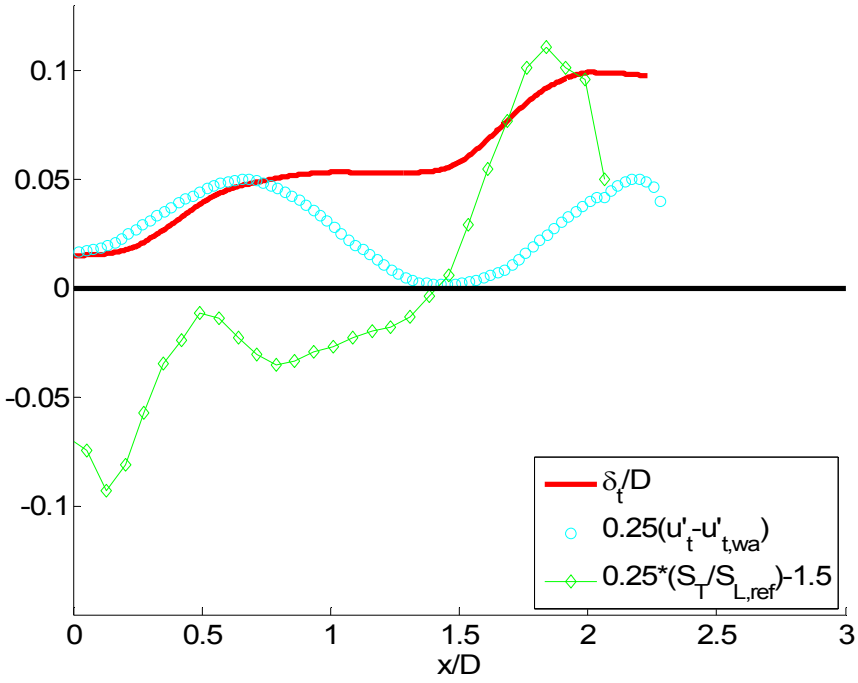

(a)

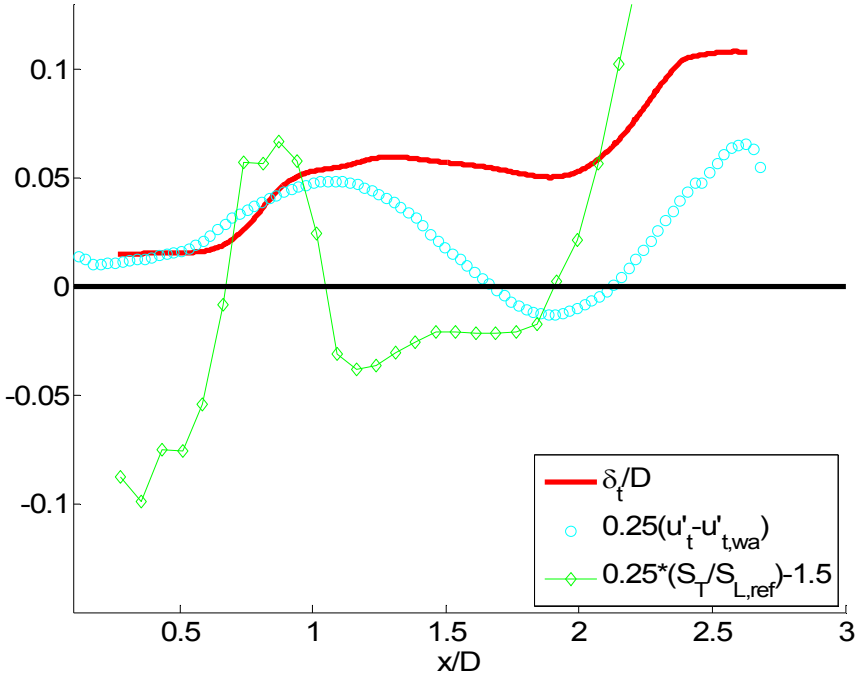

(b)

Figure 62: Sample variations of the flame brush thickness, the turbulence intensity along the flame front, the axial gradient in the velocity field and the axial velocity at *Re*= 10,000 Hz, f_{drive} = 300 Hz, (a) u'_o/u_o = 0.05 and (b) u'_o/u_o = 0.1.

Thus at regions where the (u'_t-$u'_{t,wa}$) is decreasing, the growth of $S_{T,LC} / S_{L,ref}$ also decreases while in regions where (u'_t-$u'_{t,wa}$) is increasing, $S_{T,LC} / S_{L,ref}$ increases rapidly. Since $S_{T,LC} / S_{L,ref}$ is a direct measure of the flame wrinkling at any given location, the behavior of $S_{T,LC} / S_{L,ref}$ indicates that the flame wrinkling grows rapidly at the vortex locations, while very slowly between the vortices. Correlating the flame wrinkling to the flame brush thickness, this seems to explain the trends observed in the flame brush thickness as well.

Effect of excitation amplitude on $S_{T,LC}/S_L$

The effect of acoustic amplitude on the consumption speed is next studied at a fixed excitation frequency and phase and a sample result is presented in Figure 63. From Figure 63, we see that with increasing acoustic amplitude, the difference in the spatial variation of $S_{T,LC}/S_{L,ref}$ from the unforced case also increases. For example, in Figure 63, increasing the acoustic amplitude - u'_a/u_o from 0 to 0.05 and then to 0.1 changes the observed trends in the behavior of $S_{T,LC}/S_{L,ref}$ from an almost linear trend to a step like behavior.

Phase Jitter

The above section on the local consumption speed showed that the turbulence intensities were affected by the acoustic forcing which then lead to changes in flame wrinkling and hence flame brush thickness. However, the flame brush thickness may be influenced not only by the flame wrinkling but by flame movement/flapping.

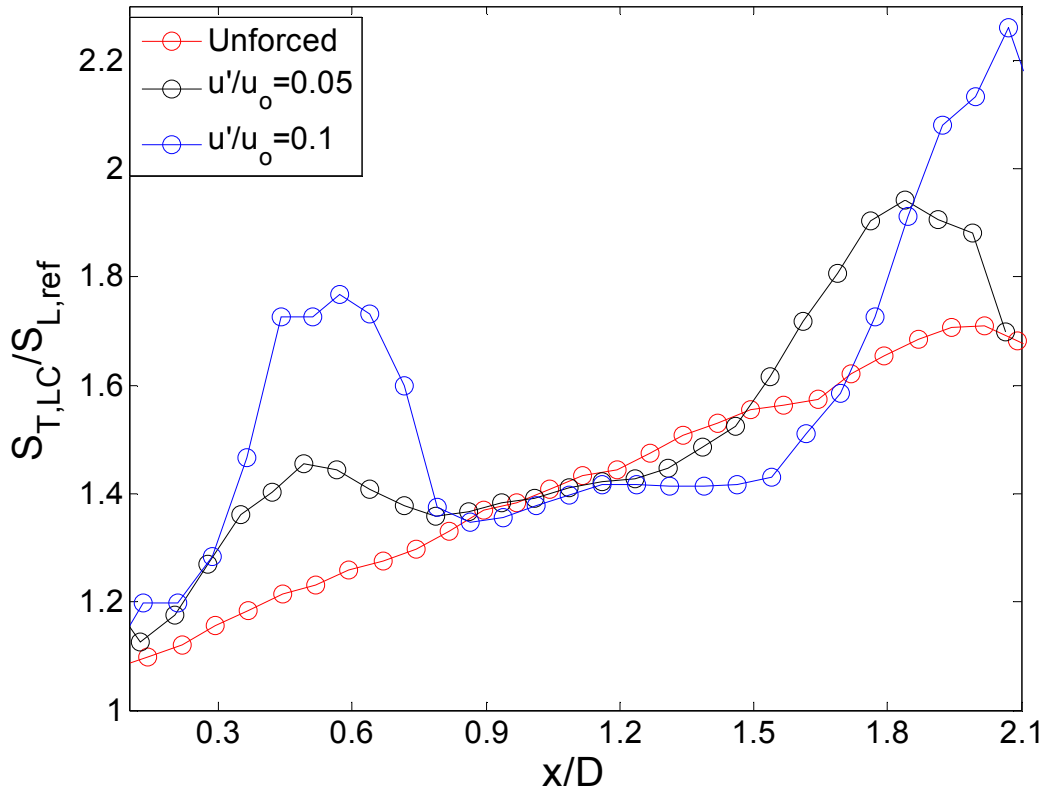

Figure 63: Effect of excitation amplitude on $S_{T,LC}/S_{L,ref}$ at a given phase, *Re*= 10,000 Hz, and f_{drive} = 300 Hz.

To quantify this effect, the "jitter" present at each spatial location of the flame front is captured in this sub-section. The cause of this jitter is because of cycle to cycle variations in the temporal location of the shed vortex. This variation is called "phase jitter" and arises due to multiple reasons which may include turbulence, non-uniform boundary conditions etc. Phase jitter may be random in nature and might thus contribute towards the incoherent fluctuations of the flame front location which in turn mainly influences the flame brush thickness. In other words the effect of phase jitter is to cause an influence on the incoherent component of the flame front location from contributions of the coherent part. In a linear sense, the flame front position may be modeled as the superposition of (a) mean location – influenced by boundary conditions, equivalence ratio, mean flow

conditions etc. (b) coherent part – influenced by acoustic excitation, vortex shedding etc. and (c) an incoherent part influenced by the turbulence present in the flow field. The same is represented mathematically in Equation (5.3) where *f(x)* is the spatial variation of the amplitude of excitation, *Φ(x,t)* is the phase of the acoustic component which is both a function of space and time and *g(x,t)* is the incoherent part of the fluctuations. Subtracting the mean component yields the fluctuating component *L(x,t)* as shown in Equation (5.4). Taking an ensemble average of Equation (5.4) at a given time/phase of the acoustic cycle yields Equation (5.5) for the mean flame position while calculating the standard deviation yields the flame brush thickness δ_t – Equation (5.12). The steps involved in this derivation are shown below.

$$\tilde{L}(x.t) = \bar{L}(x,t) + f(x)Sin(\omega t - \frac{x}{U} + \Phi(x,t)) + g(x,t) \tag{5.3}$$

The fluctuating part can be obtained by subtracting the mean component and yields

$$L(x.t) = f(x)Sin(\omega t - \frac{x}{U} + \Phi(x,t)) + g(x,t) \tag{5.4}$$

Taking the ensemble average of Equation (5.4) at yields

$$\langle L(x) \rangle = f(x)\left\langle Sin(\omega t - \frac{x}{U} + \Phi) \right\rangle \tag{5.5}$$

or

$$\langle L(x) \rangle = f(x)\left(Sin(\omega t - \frac{x}{U})\langle Cos(\Phi) \rangle + Cos(\omega t - \frac{x}{U})\langle Sin(\Phi) \rangle \right) \tag{5.6}$$

Next, taking the square of Equation (5.4) and ensemble averaging the resulting equation yields

$$\left\langle L^2 \right\rangle = f^2(x)\left\langle Sin^2(\omega t - \frac{x}{U} + \Phi) \right\rangle + \left\langle g^2 \right\rangle + \left\langle 2f(x)Sin(\omega t - \frac{x}{U} + \Phi)g \right\rangle \tag{5.7}$$

On assuming that the incoherent and coherent parts are independent renders the last term to zero yielding

$$\left\langle L^2 \right\rangle = f^2(x)\left\langle Sin^2(\omega t - \frac{x}{U} + \Phi) \right\rangle + \left\langle g^2 \right\rangle + 0 \tag{5.8}$$

The variance is given by:

$$\text{var} = \left\langle L^2 \right\rangle - \left\langle L \right\rangle^2 \tag{5.9}$$

Substituting from Equations (5.8) and (5.6) yields:

$$\text{var} = f^2 \left\langle Sin^2(\omega t - \frac{x}{U} + \Phi) \right\rangle + \left\langle g^2 \right\rangle - f^2 \left\langle Sin(\omega t - \frac{x}{U} + \Phi) \right\rangle^2 \tag{5.10}$$

or

$$\text{var} = f^2 \left(\left\langle Sin^2(\omega t - \frac{x}{U} + \Phi) \right\rangle - \left\langle Sin(\omega t - \frac{x}{U} + \Phi) \right\rangle^2 \right) + \left\langle g^2 \right\rangle \tag{5.11}$$

Finally, the flame brush thickness δ_t which is the square root of the variance:

$$\delta_t = \left(f^2 \left(\left\langle Sin^2(\omega t - \frac{x}{U} + \Phi) \right\rangle - \left\langle Sin(\omega t - \frac{x}{U} + \Phi) \right\rangle^2 \right) + \left\langle g^2 \right\rangle \right)^{\frac{1}{2}} \tag{5.12}$$

$$\delta_t = \left(f^2 \left(\begin{array}{l} \frac{1}{2} - \frac{1}{2} Cos(2\omega t - \frac{2x}{U}) \left\langle Cos(2\Phi) \right\rangle \\ + \frac{1}{2} Sin(2\omega t - \frac{2x}{U}) \left\langle Sin(2\Phi) \right\rangle - \left\langle Sin(\omega t - \frac{x}{U} + \Phi) \right\rangle^2 \end{array} \right) + \left\langle g^2 \right\rangle \right)^{\frac{1}{2}} \tag{5.13}$$

or

$$\delta_t = \left(f^2 \left(\begin{array}{l} \frac{1}{2} - \frac{1}{2} Cos(2\omega t - \frac{2x}{U}) \left\langle Cos(2\Phi) \right\rangle \\ -Sin^2(\omega t - \frac{x}{U} + \Phi) \left\langle Cos(\Phi) \right\rangle^2 \end{array} \right) + \left\langle g^2 \right\rangle \right)^{\frac{1}{2}} \tag{5.14}$$

Now, if one were to assume a Gaussian profile for the phase with a zero mean and variance σ^2 i.e. :

$$\Phi(x) = \frac{1}{\sqrt{2\pi\sigma^2}} e^{-\frac{x^2}{2\sigma^2}} \tag{5.15}$$

then Equation (5.5) becomes

$$\left\langle L(x) \right\rangle = f(x) Sin(\omega t - \frac{x}{U}) \left\langle Cos(\Phi) \right\rangle \tag{5.16}$$

or

$$\left\langle L(x) \right\rangle = f(x) Sin(\omega t - \frac{x}{U}) e^{-\frac{\sigma^2}{2}} \tag{5.17}$$

Substituting for *f(x) and Φ(x,t)* in Equation (5.14) yields

$$\delta_t{}^2 - \left\langle g^2 \right\rangle = \frac{\left\langle L \right\rangle^2}{Sin^2(\omega t - \frac{x}{U}) e^{-\sigma^2}} \left(\begin{array}{l} \frac{1}{2} - \frac{1}{2} Cos(2\omega t - \frac{2x}{U}) e^{-2\sigma^2} \\ -Sin^2(\omega t - \frac{x}{U}) e^{-\sigma^2} \end{array} \right) \tag{5.18}$$

Now from the experiments, δ_t – the flame brush thickness is known at different phases is known. In addition, $\langle g^2 \rangle$ is taken as the square of the average of the flame brush thickness across all the phases is also known as is $\langle L \rangle$ the mean flame position at the different phases. The only unknown in Equation (5.18) is σ and can thus be solved for numerically. The results are shown in Figure 64 which plots the spatial distribution standard deviation of the phase jitter. From Figure 64, it can be seen that σ does not vary

spatially and is nearly a constant equaling 12°. The same may be observed at the higher amplitude of $u_a'/u_o = 0.15$.

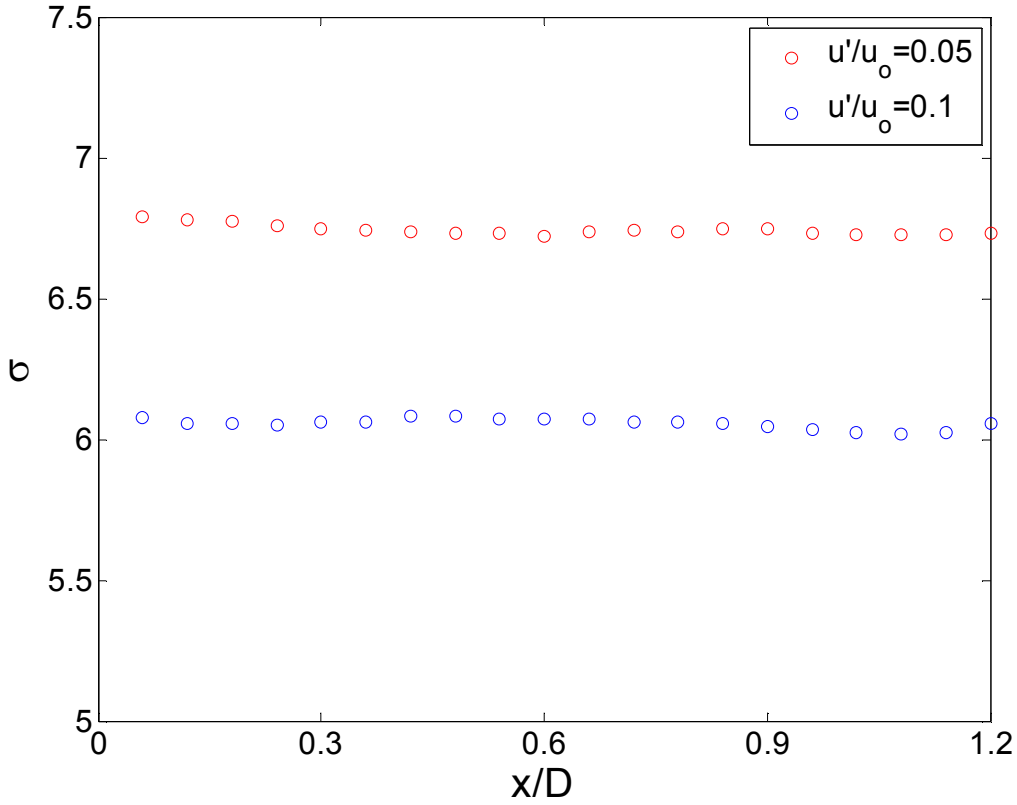

Figure 64: Spatial variation of the phase jitter at different acoustic amplitudes and *Re*= 10,000 Hz, and f_{drive} = 300 Hz.

Swirl Stabilized Flame

The results presented in this subsection were based on experimental data obtained at *Re* of 21,000 (based on the nozzle exit diameter and a mean nozzle exit flow velocity of nearly 21 m/s). The acoustic excitation was at a frequency of 130 Hz, while the excitation amplitude at which data was recorded was $u'_a/u_o = 0.3$ and 0.6.

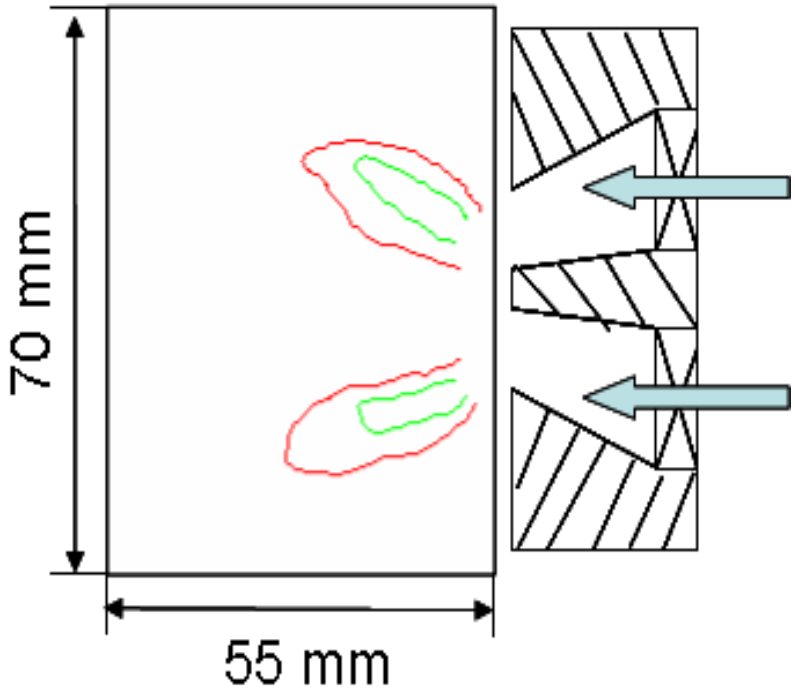

Figure 65: Evolution of the flame brush as given by the progress variable contours of $\overline{c}$ =0.3 (green line) and $\overline{c}$ =0.7 (red line) of an unforced swirl flame at *Re* = 21,000.

The flame brush was computed after digitizing the images and using the same progress variable approach used for the Bunsen flame. Figure 65 presents the flame brush contours of the unforced flame corresponding to the progress variables of $\overline{c}$ = 0.3 and 0.7. From, this figure it can be observed that the flame brush seems to grow, although at a very small rate with downstream distance. Also, note that the flame height in this case was only around 30 mm, ~ 3 times the width (11.9 mm) of the annular passage at the nozzle exit.

Next, in the presence of acoustic oscillations, Figure 66, describes the typical variation of the flame brush contours with phase. It can be observed that length of the flame is clearly modulated with phase through the acoustic cycle. Similar to the Bunsen flame, the growth of the flame brush is quite slow as well in the forced case. However, the step-like

behavior of the flame brush thickness observed in the Bunsen flame is not replicated here. This may be associated with the apparent lack of the same coherent vortex present for the Bunsen flame.

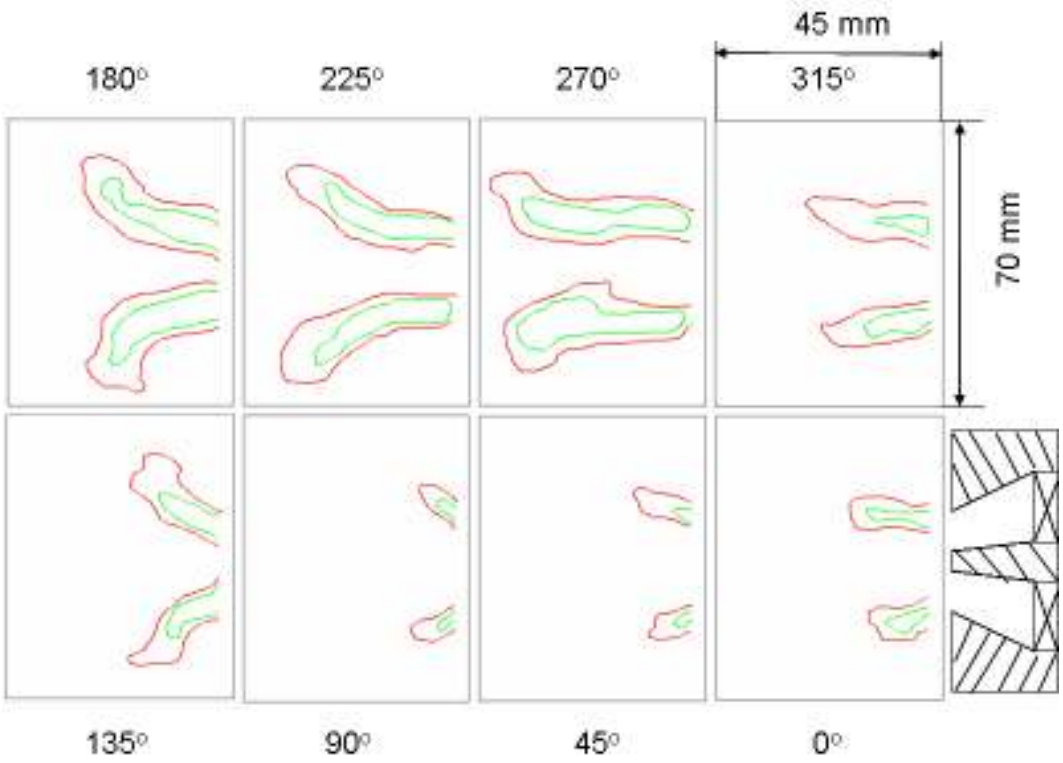

Figure 66: Contour plots of the progress variables $\overline{c}$ =0.3 (green line) and $\overline{c}$ =0.7 (red line) showing the development of the flame brush at *Re* = 21,000, f_o = 130 Hz and u'_a/u_o = 0.6.

Quantitative plots showing the variation of δ_t /D_{an} for the swirling flame are shown in Figure 67. It should be noted here that only regions close to the nozzle exit is presented. Figure 67 plots the spatial variation of the flame brush thickness for the unforced and acoustically excited cases. The amplitude of fluctuation of the flame brush thickness at the different phases of the acoustic cycle can be seen to increase with acoustic amplitude. For example, at the excitation amplitude of 0.9, the variation between the phases of δ_t /D_{an} can be seen to higher than at u'_a/u_o = 0.45.

The consumption speed ($S_{T,LC}/S_{L,ref}$) was calculated using the same procedure as described for the Bunsen flame. Once again, comparisons were made for both the unforced and forced cases and the results are shown in Figure 68 which plots the spatial development of $S_{T,LC}/S_{L,ref}$. From this figure, it can be seen that first, $S_{T,LC}/S_{L,ref}$ in the presence of acoustic excitation, is always lower than for the unforced case. For example, in Figure 68, at the experimental conditions of u'_a/u_o = 0.45 and 0.9 and at all the spatial locations, $S_{T,LC}/S_{L,ref}$ is lower than the unforced case. Comparing this result to the spatial development of the flame brush thickness in Figure 67, the results seem to be in tandem. That is, a lower $S_{T,LC}/S_{L,ref}$ is observed in the presence of acoustics indicating that the degree of wrinkling of the flame front is lower in the presence of acoustics. A lower degree of wrinkling could result in a lower flame brush thickness and the same is observed in Figure 67.

In addition, in Figure 68, the growth rate of $S_{T,LC}/S_{L,ref}$ is lower than that of the unforced case. This result corroborates the result observed in Figure 68 where the flame brush thickness δ_t /D_{an} is also seen to grow at a slower rate in the presence of acoustics. Finally, at the highest acoustic amplitude of u'_a/u_o = 0.9, it can be seen that the amplitude of fluctuation at the various phases of $S_{T,LC}/S_{L,ref}$ is seen to be higher than at the lower excitation amplitude of u'_a/u_o = 0.45 – the same was observed for the flame brush thickness δ_t /D_{an} in . Also, if one recalls the results of the fractal dimension presented in Chapter 4, Figure 45 which showed that the amplitude of fluctuation of the fractal dimension (and hence the global consumption speed $S_{T,GC}$) was higher at u'_a/u_o = 0.9 than at u'_a/u_o = 0.45 the same could be explained by $S_{T,LC}/S_{L,ref}$. Comparing the two

results, it can be seen that the fluctuating global consumption speed occurs not only because of a fluctuating flame length but also a fluctuating local consumption speed.

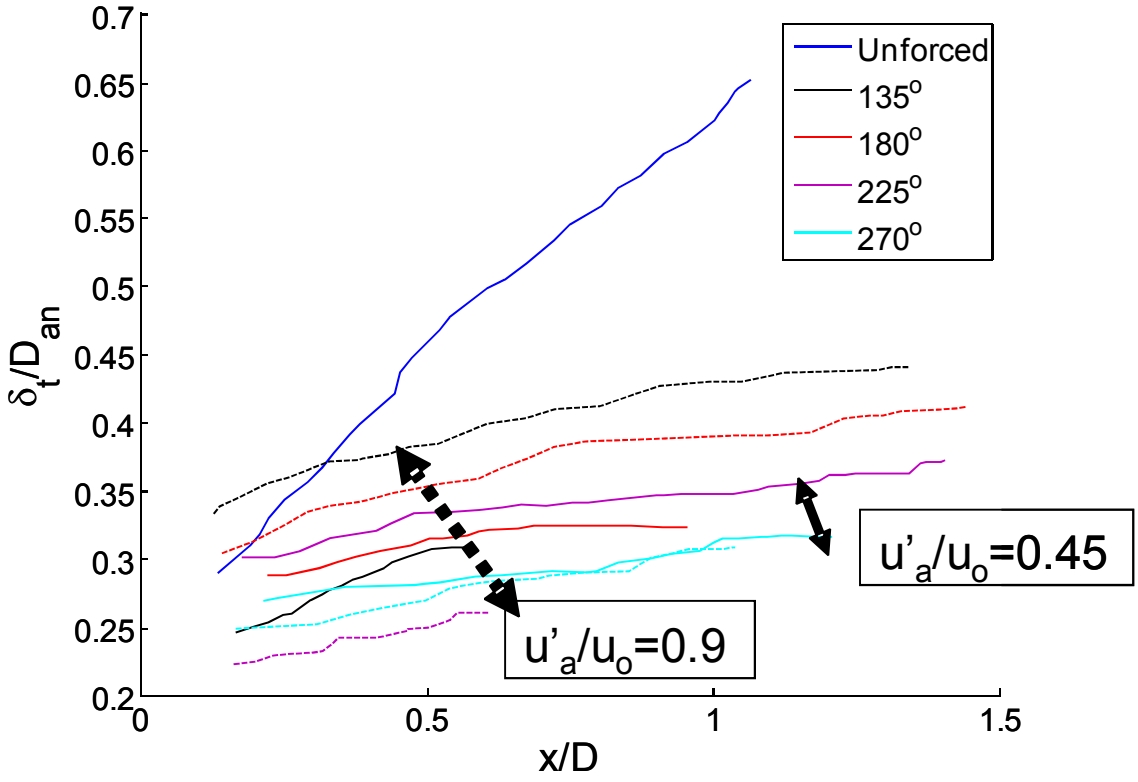

Figure 67: Variation of the normalized flame brush thickness (δ_t/D_{an}) along the normalized flame coordinate (s/D_{an}) at Re = 21,000, f_o = 130 Hz.

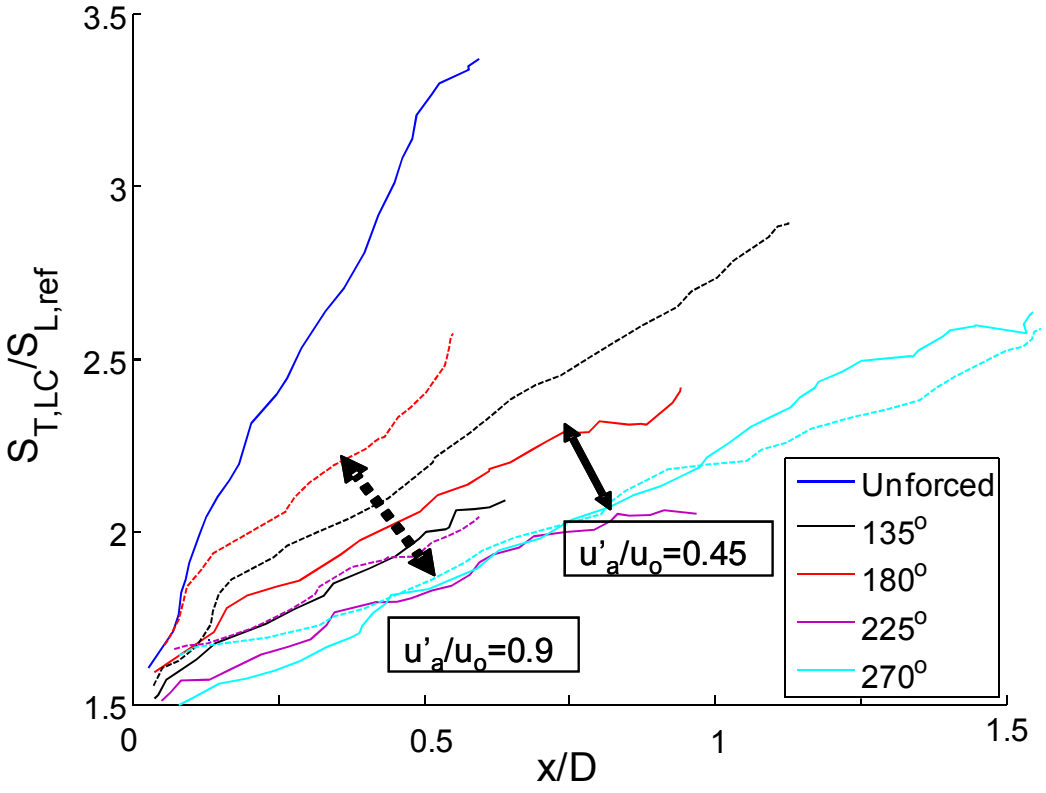

Figure 68: Variation of the normalized flame brush thickness (δ_t / D_{an}) along the normalized flame coordinate (s/D_{an}) at Re = 21,000, f_o = 130 Hz.

CHAPTER 6

CONCLUSIONS AND RECOMMENDATIONS FOR FUTURE WORK

This chapter summarizes the contributions from this thesis from Chapters 4 and 5 and provides recommendations for future work as well.

Summary of Contributions

1. Flame response to harmonic excitation

The flame response to harmonic excitation of a lean premixed swirl combustor was measured using the global chemiluminescence of CH* and OH*. The results presented in Chapter 4 show that the flame response of a swirl combustor to harmonic excitation is highly nonlinear and depends on the frequency, amplitude as well as the flow velocity. In addition, while the flame response increases monotonically with perturbation amplitude for low forcing levels; its behavior becomes much more complex at higher levels. At higher amplitudes, the flame response can saturate, saturate then increase again, decrease then increase and saturate, among others. This behavior of the flame response calls for an examination of the flame response models which assume a linear increase followed by saturation. In addition, to improve accuracy in amplitude predictions, the above result suggests that the flame response models may need to be modified accordingly by incorporating flame transfer functions of non-traditional shapes.

2. Characterization of flame/flow processes that control flame response

Phase locked OH PLIF measurements of these acoustically excited swirl flames were conducted for various conditions of flow velocities, excitation frequency and amplitudes. The images showed that at the low flow velocities and for no acoustic excitation, the

flame was attached to the center body. At higher flow velocities, the flame was lifted off the center body and was stabilized at the IRZ. From an analysis of a large number of OH PLIF images and from a wide range of conditions, it was seen that the complex flame dynamics is controlled by a superposition of the following processes – (1) annular jet fluctuations, (2) fluid mechanical instabilities of the backward facing step, jet column, swirl, and shear layer and (3) oscillatory flame speed and brush development.

The annular jet fluctuations seemed to be the major contributor to the overall variations of the flame length, area and hence heat release. At high amplitudes of excitation, it was seen that the flame could rollup into the ORZ, IRZ as well as be lifted off the center body at some phases of the acoustic cycle. The dynamics of the IRZ seemed to follow that of the flame response for the cases of higher flow velocities (where the flame was stabilized at the IRZ). The phase relationship between the motion of the IRZ, the ORZ and the fluctuating annular jet was shown to be important in determining the net flame area fluctuations. Shear layer instabilities in the IRZ and the ORZ were also seen to be excited and the presence of KH-instabilities in the IRZ and the ORZ could be seen through the OH PLIF images.

The mechanism of the modulation of the turbulent flame speed was examined in greater detail. In particular, the fractal characteristics of the flame were computed and it was seen that at the higher excitation amplitudes, the fluctuation in the fractal dimension was higher than at lower amplitudes of excitation. The relationship between the fractal dimension and the turbulent flame speed was described and it was seen that the fluctuations in the turbulent flame speed (through an acoustic cycle) increases with excitation amplitude.

These results show that the amplitude dependent flame response in not controlled by one single physical process but rather by several competing physical processes. This stresses the need to examine each one of these mechanisms in greater detail to try and characterize the various conditions/configurations under which the mechanisms might exist or be excited. In addition, the above results throw some light into a few of the mechanisms that need to be incorporated into flame response models to capture the physics and improve the accuracy of amplitude predictions.

3. Effect of harmonic forcing on turbulent flame properties

A detailed analysis of the effect of harmonic forcing on the turbulent flame properties was conducted in two experimental configurations. In particular, the effect of acoustic excitation on the spatial variations of the flame brush thickness and the local consumption was studied for both the swirl flame as well as a turbulent Bunsen flame. Phase locked PIV measurements were used to capture the flame front and the velocity field simultaneously for the acoustically excited Bunsen flame. The results showed that while the flame brush thickness for the unforced cases grew monotonically with axial distance, in the presence of acoustic forcing the flame brush thickness grew in a step like manner. The flame brush thickness grew rapidly close to the vortex locations but in between any two vortices, the flame brush thickness grew very slowly relative to the unforced case. The effect of gradually increasing excitation amplitude from no forcing to 20% of the mean flow showed that the step like growth of the flame brush thickness got more pronounced - indicating that there was no threshold amplitude at which this behavior was triggered. The effect of changing excitation frequency showed similar effects on the growth of the flame brush thickness with a varying vortex location based

on the excitation frequency.

The velocity measurements showed that in the regions of negative velocity gradients, the flame brush thickness grew very slowly while in the regions of positive velocity gradients the flame brush thickness grew rapidly. This seemed counterintuitive as the turbulent diffusion model indicates that the flame brush thickness grows in the region of negative velocity gradients leading to a belief that stretch effects might be playing an important role in the growth of the flame brush thickness. To examine this, similar measurements were conducted using a fuel with opposite stretch effects (i.e. opposite sign of Markstein number). The results showed that there was no effect in the spatial variations of the flame brush thickness.

The velocity measurements also showed that the relative turbulence intensity in the presence of acoustics (i.e. subtracting the mean acoustic field) was modulated spatially and that this turbulence intensity grew in the regions of positive velocity gradients and decreased in the regions of negative velocity gradients. This modulation of the turbulence intensity has been seen in the past in the study of acoustically forced non-reacting shear layers. In these cold flow cases it was seen that the shear layer also grew in a step like manner and the reason attributed to this behavior was that the turbulence intensity was being modulated and in the regions where the shear layer increased slowly, the turbulent energy was being fed into the coherent part of the flow. Thus, the modulation of the relative turbulent intensity in the presence of acoustics seen in the current research study may be explained by this interaction between the incoherent and coherent parts of the flow. This might be also used to explain in part the step like behavior of the flame brush thickness.

The spatial variation of the local consumption speed was also obtained at the various conditions using the flame edges from the PIV images. In the presence of acoustic forcing, it was seen that the consumption speed behaved analogous to the flame brush thickness and grew in a step like manner. In the regions of decreasing relative turbulence intensity (to the unforced case), the consumption speed also grew slowly which in the regions of increasing relative turbulence, the consumption speed grew rapidly.

Finally, the spatial variation of the flame brush thickness for the swirl flames was seen to grow at a slower rate than the unforced cases. The amplitude of fluctuation at the various phases of the acoustic cycle was seen to increase with acoustic excitation. The local consumption showed similar behavior and the amplitude of fluctuations was seen to increase with excitation amplitude. This trend was seen to be similar to the behavior of the global consumption speed as estimated by the fractal dimension wherein it was seen that the amplitude of fluctuations of the global consumption speed was seen to grow with excitation amplitude.

The results presented in this section are the first experimental study to show the importance of the modulations of the turbulent flame properties in the presence of harmonic forcing. In addition, the results stress the need to incorporate such variations in combustion dynamics predictions to improve accuracy in amplitude predictions.

Recommendations for Future Work

The initial results from the study showed that the flame response was highly nonlinear in nature. Since, the flame response is controlled by the driving and the damping each of these need to be examined separately to understand the nonlinear flame response. In particular, measurements trying to specifically quantify the amount of

damping/driving present at the various conditions and finally the mechanisms leading to non-linearities in flame response need to be undertaken.

The current research identified and catalogued the various physical processes that affect the flame response to acoustic excitation. These processes are occurring to some extent simultaneously, with non-monotonic dependencies upon forcing amplitude, and not necessarily with the same phase relative to each other. This sheds some light on the complex overall flame heat release response measurements and suggests a fruitful area for detailed computational studies that can better elucidate the underlying physics controlling the phenomenon. While one of the mechanisms of the fluctuations in the turbulent flame speed was examined, the remaining mechanisms of the influence of the fluid mechanical instabilities of the backward facing step, jet column, swirl, and shear layer on the flame response need to be examined in greater detail. To understand the fluid mechanics and its effect on the flame, measurement techniques that can capture the flame and the flow at the same time need to be used.

In addition, for the Bunsen flame the PIV measurements were used to explain the spatial variations in the turbulent flame brush and local consumption speeds. The results stressed the need of considering and incorporating flame speed fluctuations in combustion dynamics models. This also calls to understand the mechanisms behind these fluctuations for a swirl combustor using simultaneous flow/flame measurements. Finally, while these studies are more fundamental in nature, similar studies at high pressures need to be undertaken to be able to directly relate to industrial settings.

APPENDIX 1: UNCERTAINTIES IN FLOW MEASUREMENTS

The air and fuel flow rates throughout the research study were measured using rotameters with ranges of 0- 500 SCFH and 0-250 SCFH for the fuel flow respectively. At the typical operating flow conditions, the rotameters were calibrated against a drum flow meter and the results are as shown in Figure 69. From this Figure, one can readily see that the bias errors associated with the rotameters at the desired flow rates are less than 5%.

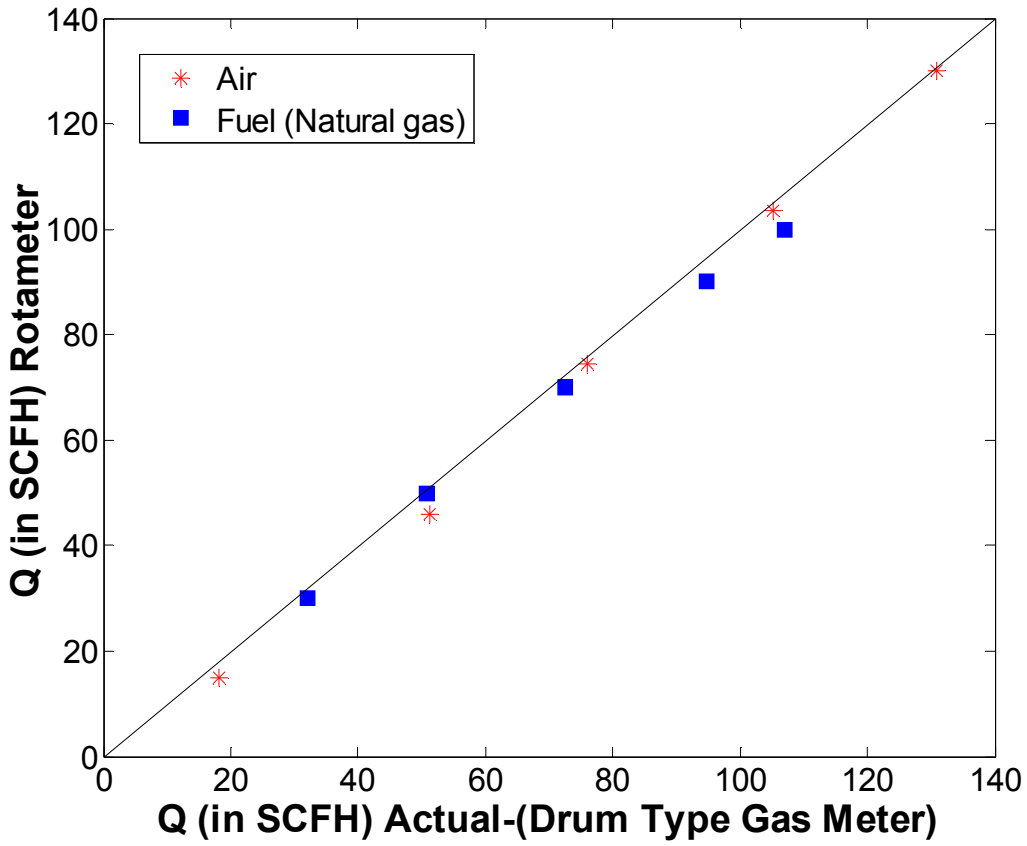

Figure 69: Calibration curve of the air rotameters at a pressure of 18 psig and fuel at atmospheric pressure conditions

APPENDIX 2: PMT LINEARITY STUDIES

Each of the PMTs operated under a certain range of voltage outputs based on the chemiluminescence inputs. In a test study, the light rays from a source were passed through a PMT and through an optical filter with varying absorption ratios. The voltage recorded from the PMTs was then analyzed as a function of the absorption ratio and a representative comparison is shown in Figure 70. As can be seen from Figure 70, in the range of voltages ranging from 0-6 V, the PMT is well within the linear regime indicating that any increase of PMT voltage because of chemiluminescence directly corresponds to an increase in the voltage shown by the PMT (i.e. a linear one –one correspondence exists).

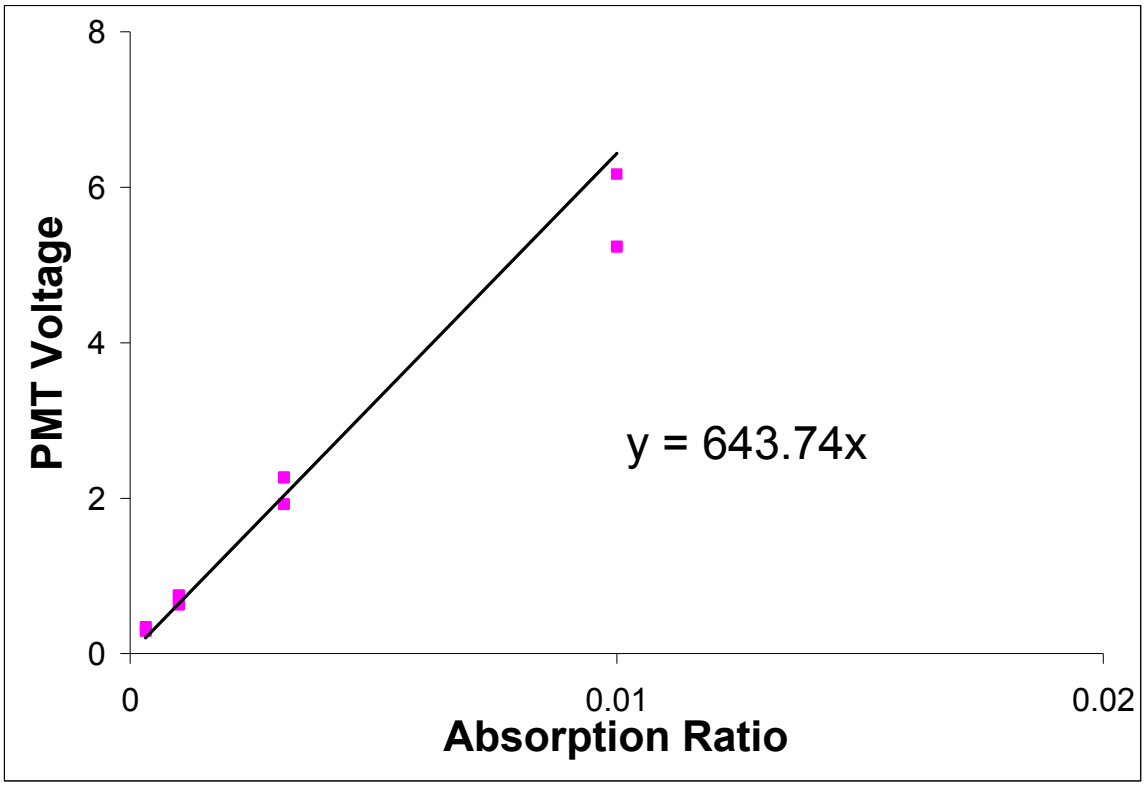

Figure 70: PMT voltage vs absorption ratio (as determined by putting in filters of known absorption).

Now during each of the chemiluminescence experiments, the maximum PMT voltage that was observed never exceeded 4 V indicating that the PMT lies in the linear regime of operation while recording chemiluminescence data from the flame.

REFERENCES

[1] Lee J., Santavicca D., "Experimental Diagnostics for the Study of Combustion Instabilities in Lean, Premixed Combustors", *J. Prop. Power*, 19(5) (2003) 735-750.

[2] Richards G., Straub D., Robey E., "Passive Control of Combustion Dynamics in Stationary Gas Turbines", *J. Prop. Power*, 19(5) (2003) 795-810.

[3] Dowling A.P., "Nonlinear Self-Excited Oscillations of a Ducted Flame",*J. Fluid Mech*., 346 (1997) 271-290.

[4] Lieuwen, T., Yang, V. "Combustion Instabilities in Gas Turbine Engines: Operational Experience, Fundamental Mechanisms, and Modeling", *AIAA,* Reston, VA, USA, 2005, Chapter 12.

[5] Rayleigh J.W.S. (1896), "The Theory of Sound", Vol. 2. Mc. Millan & Co London and New York

[6] Lieuwen, T., "Experimental Investigation of Limit Cycle Oscillations in an Unstable Gas Turbine Combustor",*J. Prop. Power*, 18(1), 2002, pp.61-67.

[7] Dowling A.P., "A Kinematic Model of a Ducted Flame" J. Fluid Mech., 394 (1999) 51-72.

[8] Peracchio A.A., Proscia W.M., "Nonlinear Heat Release/Acoustic Model For Thermo-Acoustic Instability In Lean Premixed Combustors",*J. of Eng. for Gas Turbines & Power*, 121 (1999) 415–421.

[9] Baillot F., Durox D., Prud'homme R., "Experimental and Theoretical Study of a Premixed Vibrating Flame",*Combust. Flame*, 88 (1992) 149-168.

[10] Durox D., Baillot F., Searby G., Boyer L., “On the Shape of Flames Under Strong Acoustic Forcing: A Mean Flow Controlled by an Oscillating Flow”,*J. Fluid Mech*. 350 (1997) 295-310.

[11] Bourehla A., Baillot F., “Appearance and Stability of a Laminar Conical Premixed Flame Subjected to an Acoustic Perturbation”,*Combust. Flame*, 114 (1998) 303-318.

[12] Bellows B.D., Bobba M.K., Seitzman J.M., Lieuwen T.,, “Flame Transfer Function Saturation Mechanisms in a Swirl-Stabilized Combustor,”*Proc. Combust. Inst*. 31(2) (2007) 3181-3188.

[13] Kulsheimer C., Buchner H., “Combustion dynamics of turbulent swirling flames”, *Combust. Flame*, 131 (2002) 70-84.

[14]D. Kim, J. G. Lee, B. D. Quay, K. Kim, S. Srinivasan and D. Santavicca, "Effect of Flame Structure on the Flame Transfer Function in a Premixed Gas Turbine Combustor”, *ASME paper*, GT-2008-51014, 2008.

[15] Balachandran R., Ayoola B.O., Kaminski C.F., Dowling A.P., Mastorakos E., “Experimental Investigation of the Nonlinear Response of Turbulent Premixed Flames to Imposed Inlet Velocity Oscillations”, *Combust. Flame*, 143 (2005) 37-55.

[16] Biagoli, F, Felix G, Bruno S., “Combustion dynamics linked to flame behaviour in a partially premixed swirled industrial burner”, *Experimental Thermal and Fluid Science,* 32 (7), 2008, 1344-1353.

[17] Driscoll J.F., "Turbulent premixed combustion: Flamelet structure and its effect on

turbulent burning velocities", *Prog. in Energy and Combust. Sci*. (2008), 91-134.

[18]Damkohler, G, "Der einflußder Turbulenz auf die Flammengeschwidigkeit in Gasgemischen," (1940) *Z. Electrochem* (46), 1947, English Translation NASA Tech Mem. 1112.

[19] Lipatnikov, A.N. and Sathiah, P. "Effects of turbulent flame development on thermoacoustic oscillations", *Combust. Flame*, 142 (2005) 130-139.

[20] Zimont, V. L., "Theory of Turbulent Combustion of a Homogeneous Fuel Mixture at High Reynolds Numbers", *Combust. Expl. and Shock Waves*, Vol. 15 (1979), 305-311.

[21] Zimont, V. L., and Lipatnikov, A. N, "A numerical model of premixed turbulent combustion of gases", *Chem. Phys. Report*, Vol. 14 (7) (1995), 993-1025.

[22]Lipatnikov, A.N, Chomiak J*,* "Turbulent flame speed and thickness: phenomenology, evaluation, and application in multi-dimensional simulations", *Prog. in Energy & Combust. Sci.*,28(1) ,(2002) 1-74.

[23]Waser, M.P., Crocker, M.J., "Introduction to the two-microphone cross-spectral method of determining sound intensity", *Noise Control Engineering Journal*, 22(3), pp. 76-85, 1984.

[24]Boden, H., Abom, M., "Influence of errors on the two-microphone method for measuring acoustic properties in ducts", *J. Acoust. Soc. Amer.,* 79(2), pp.541-549,1986.

[25]Jang, S. and Ih, J., "On the multiple microphone method for measuring in-duct acoustic properties in the presence of mean flow", *J. Acoust. Soc. Am.,* 103 (3), 1998.

[26] Samaniego, J.-M., Egolfopoulos, F., Bowman, C., "Mechanism of nitric oxide formation in oxygen-natural gas combustion", *Combustion Sci. and Tech*., 109, 183-203, 1995.

[27]W. Pun, S.L. Palm, F.E.C. Culick, "Combustion d ynamics of an acoustically forced flame", *Combust. Sci. and Tech*. 175 (2003) 499-521.

[28]D.M. Kang, F.E.C. Culick, A. Ratner, "Combustion dynamics of a low-swirl combustor", *Combust.and Flame*, 151(3) (2007) 412-425.

[29] Pfadler, S., Czichos M.,Dinkelacker, F.,Leipertz,A., "Measurement of turbulent transport mechanisms in premixed flames by conditioned PIV techniques", *Proc. of the European Combust. Meeting* 2005, paper 113, Louvain-la-Neuve, Belgium.

[30]Pfadler, S.,Leipertz A.,, Dinkelacker,F., "Systematic experiments on turbulent premixed Bunsen flames including turbulent flux measurements", *Combust. Flame* 152 (4) (2008), pp. 616–631.

[31]Pfadler, S., ,Leipertz,A., Dinkelacker F., "Two-dimensional direct measurement of the turbulent flux in turbulent premixed swirl flames", *Proc. Combust. Inst.* 31 (1) (2007), pp. 1337–1344.

[32]Gulder O.L Smallwood G.J, Wong R, Snelling D., R. Smith R. Deschamps B.M & Sautet J.C, "Flame front surface characteristics in turbulent premixed propane/air combustion", *Comb. And Flame*, Vol. 120, 2000, pp. 407-416.

[33]Das A.K ,Evans R.L., "An experimental study to determine fractal parameters for lean premixed flames", *Experiments in Fluids*, 22, 1997, pp. 312-320.

[34]Shepherd I.G, Cheng R.K, Talbot L, “Experimental criteria for the determination of fractal parameters of premixed turbulent flames”, *Experiments in Fluids*, 13, 1992, pp. 386-392.

[35]Davis M.R., Li H.L., “Evaluation of fractal dimension for mixing and combustion by the schlieren method”, *Exper. In Fluids*, 1995, 21 (4), 248-258.

[36]Smallwood G.J., Gulder O.L., Snelling D., . Deschamps B.M., Gokalp I., “Characterization of flame front surfaces in turbulent premixed methane/Air combustion”, *Comb. And Flame*, Vol. 101 (4), 1995, pp. 461-470.

[37]Bérubé D.,Jébrak M., “High precision boundary fractal analysis for shape characterization”, *Computers and Geosciences,* 1999 25(9), 1059-1071.

[38]Gouldin F.C,Hilton S.M, Lamb T, “Experimental evaluation of the fractal geometry of flamelets”, *Twenty Second Symposium on Combustion*, 1988, pp. 541-550.

[39]Y. Huang and V. Yang, “Bifurcation of flame structure in a lean-premixed swirl-stabilized combustor: transition from stable to unstable flame", *Combust. & Flame*, 136 (3) (2004) 383-389.

[40]K.K. Venkataraman, L.H. Preston, D.W. Simons, B.J. Lee, J.G. Lee, D.A. Santavicca, “Mechanism of combustion instability in a lean premixed dump combustor”, *J. Prop. Power*, 15 (6) (1999) 909-918.

[41]T. Sarpkaya, “Turbulent vortex breakdown”, *Phys. Fluids* 7(10) (1995) 2301–2303.

[42]S. Leibovich and K. Stewartson, “A sufficient condition for the instability of columnar vortices”, *J Fluid Mech* 126 (1983) 335–356.

[43]W. Althaus, Ch. Bruecker, M. Weimer, “Breakdown of slender vortices” in *Fluid Vortices* (ed. S. I. Green), Kluwer (1995) p 373-426.

[44]H.M. Najm, A.F. Ghoniem, "Coupling between Vorticity and Pressure Oscillations in Combustion Instability", *J. Prop. Power*, 10 (6) (1994) 769-776.

[45]C. Ho, P. Huerre, “Perturbed Free Shear Layers”, *Annual Review of Fluid Mechanics,* (16 (1984) 365-422.

[46]H.M. Najm, A.F. Ghoniem, "Numerical-Simulation of the Convective Instability in a Dump Combustor" *AIAA Journal* 29 (6) (1991) 911-919.

[47]Bellows, B. “Characterization of Nonlinear Heat Release - Acoustic Interactions in a Premixed Combustor,”, *PhD Thesis*, Georgia Institute of Technology 2005.

[48]Atashkari K., Lawes M., Sheppard C.G.W., Wooley R., “Towards a general correlation of turbulent premixed flame wrinkling”, *Eng. Modelling and Measurements* Vol 4., 1999, 805-814.

[49]Goix P., Parontheon P., Trinite M., "A Tomographic Study of Measurements in a V-Shaped H2/Air Flame and a Lagrangian Interpretation of the Turbulent Flame Brush Evolution", *Combust and Flame* 1990, 81, 229.

[50]Renou B., Mura A., Samsun E., Boukhalfa A., “Surface Density Measurements for Freely Propagating Turbulent Premixed Flames at Various Lewis Numbers”, *International Colloquim on the dynamics of Explosions and Reactive Systems* 2001, 040.

[51] Peters N., " Turbulent Combustion”, Cambridge, Cambridge University Press 2000

[52] Bray K.N.C., “Studies of the Turbulent Burning Velocity”, *Proc. of Royal Society of London* 1995, A:451: 231.

[53] Ballal D.R., “The structure of a prem ixed turbulent flame”, *Proc. of Royal Society of London* 1979, A:367: 353.

[54]Boukhalfa A., Gokalp I., “Influence of the Damköhler number on the average thickness of conical turbulent premixed methane/air flames”, *Combust and Flame* 1988, pp 73-75.

[55]Bradley D., Lau A.K.C., LawesM., “Flame stretch rate as a determinant of turbulent burning velocity”, Phil Trans *Royal Soc. London* 1992; A 338:359

[56]Namazian M., Shepherd I.G., Talbot L., “Characterization of the density fluctuations in turbulent V-shaped premixed flames”, *Combust. and Flame* 1986; 64, 299.

[57]Sheperd I.G., “Flame surface density and burning rate in premixed turbulent flames”, *Proc of Combust Inst.* 1996, 26, 373.

[58]Cheng R.K., Talbot L., Robben F., "Conditional Velocity Statistics in Premixed CH4- Air and C2H4-Air Turbulent Flames", Proc. of Combust. Inst. 1984, 20, 443.

[59] Wiesbrot I., Wygnanski I., “On coherent structures in a highly excited mixing layer”, *J. Fluid Mechanics*, 1988, (195), 137-159.